Alma Mater Studiorum · University of Bologna

School of Science
Department of Physics and Astronomy
Master Degree in Physics

Neuromorphic devices with molecular semiconductors.

Supervisor:
Prof. Beatrice Fraboni.

Co-Supervisor:
Dr. Alberto Riminucci.

Submitted by:
Hassan Issa

Academic Year 2023/2024

University of Bologna-CNR-ISMN.

Neuromorphic devices with molecular semiconductors.

MASTER THESIS

Submitted for the degree of Master by:

Hassan Issa.
MSc. Physics.

Under the supervision of:
Professor Beatrice Fraboni.
Doctor Alberto Riminucci.

Bologna, 2024

Title: Neuromorphic devices with molecular semiconductors.

Author: Hassan Issa.

Thesis Supervision:

Professor Beatrice Fraboni, Director of Institute of Higher Studies, Department of Physics and Astronomy "Augusto Righi".

Doctor Alberto Riminucci, Researcher, CNR-ISMN.

Thesis Defense Date: Friday, 19/July/2024.

Acknowledgement

I want to start by thanking Prof. Beatrice Fraboni for the feedback and comments on the work as my university supervisor, and to express my deepest thanks and gratitude to Alberto Riminucci, my intern supervisor, for countless offered knowledge, information, experience, help, resources, suggestions, corrections, patience, time, and support.
I want to thank all ISMN crew, who treated me as one of them from day one.
I want to thank Dr. Valentin Dediu and all the group members, for all the help and shared information.
I want to specially thanks Dr. Manju Singh for being the closest one to ask for guidance, and support during my everyday labwork, and for introducing me to many techniques used for sample handling and mounting.
I want to thank Dr. Luca Gnoli for not hesitating to share any information concerning operating parts in the characterization system, pumps, electronics... and for introducing me to magneto-optic Kerr effect (MOKE), and micromagnetic simulations (mumax3).
I want to thank Dr. Raimondo Cecchini for introducing me to probe station IV characterization, and SEM imaging, and for fabricating and preparing the sample I worked with.
I want to thank Dr. Rajib Kumar Rakshit for introducing me to the deposition structure, and all operating parts used for monitoring fabrication, including shadow masking(PVD-EBPVD), and oxidation, and for fabricating the sample I worked with.
I want to thank Dr. Mattia Benini for introducing me to AFM, both data acquisition, and software related tasks used for image processing, and refining, and many statistical methods, for an accurate information extraction.

Abstract

Since the construction of Von Neumann architecture, up to these days, computers have been used to facilitate our everyday life by storing information and executing numerical calculations, but most importantly to perform AI tasks. Over time, many circuits and algorithms have been constructed to optimize the performance of these devices, granting access to more sophisticated, complex tasks to be executed in a fast accurate manner. Nowadays, computers are very efficient in task execution; However, traditional computing architecture is reaching its limitation due to many fundamental problems, such as CMOS scalability limits(Moore's law), and the huge energy consumption due to the continuous information flow and conversion between memory and processor.

In contrast, nature provided us a very compact, energy-efficient biological memory and processor combined, the human brain. Functioning as a memory capable of self-learning and processing incoming information, the brain houses approximately 10^{11} neurons, interconnected with around 10^{14} synapses, contained within a volume of 140 x 167 x 93 mm^3 and weighing an average of 1.3 Kg. The most important property of the brain, apart from the huge number of neurons, is the synaptic plasticity, enabling continuous information acquisition, modification or erase through timing modulation of presynaptic and postsynaptic action potentials, this action leads to a modification in the postsynaptic Ca^{2+} signal, resulting in long (short)-term potentiation or depression.

Neuromorphic computing (NC) mimics brain performance, thus allow computing and storage in a single unit (IMC), resulting an extremely short latency, and low energy consumption. This approach is particularly useful in dynamic vision sensors in self driving cars, and event driven sensors in robotics.

Table of Contents

List of Figures

List of Tables

Abbreviations and acronyms

|↑↓> Anti-parallel spins .

|↑↑> Parallel spins .

AC Alternating Current .

ACF Autocorrelation Function .

ADAS Advanced Driver Assistant Systems .

AFM Anti-ferromagnet .

AFM Atomic Force Mircroscopy .

AI Insulator .

AMP Amplifier .

AMR Anisotropic Magnetoresistance .

BE Back scattered Electrons .

BPTT Back Propagation Through Time .

CI Canted Antiferromagnetic insulator .

CMR Colossal Magnetoresistance .

CNN Convolutional Neural Networks .

CSA Channel Spark Ablation .

CVD Chemical Vapour Deposition .

CZ Czochralski .

D2D Device to device .

DAC Digital Analog Converter .

DAFM Dynamic Atomic Foce Microscopy .

DC Direct Current .

DFT Density Functional Theory .

DL Deep Learning .

DOS density of states .

DR Dynamic Range .

DUT Device Under Test .

DVS Dynamic vision sensor .

e-beam electron beam .

EBIC Electron Beam Induced Current .

EBPVD Electron Beam Physical Vapour Deposition .

EMC Electochemical Metallization Cell .

ET Everhart-Thornley .

FCC Face Centered Cube .

FeRAM Ferroelectric Random Access Memory .

fft Fast Fourier Transform .

FI Free magnetic Insulator .

FM Ferromagnet .

FTJ Ferroelectric Tunnel Junction .

Gaq3 Tris(8-hydroxyquinoline)- Ga(III) .

GMR Giant Magnetoresistance .

HCP Hexagonal Close Packed .

HM Half Metal .

HOMO Highest occupied molecular orbit .

HRS High Resistive State .

HV High vacuum .

IB Ion Beam .

IM In Memory .

IRS Initial Resistive State .

IV Current Voltage characteristics .

KPFM Kelvin Probe Force Microscopy .

LC Local Computing .

LRS Low Resistive State .

LSMO $La_{0.7}Sr_{0.3}MnO_3$.

LSTM Long Short Term Memory .

LUMO Lowest Unoccupied Molecular orbit .

mbar-Torr pressure unit of measure .

MBE Molecular Beam Epitaxy .

MLP Multi layer perceptron .

MOM Metal Oxide Metal .

MR Magnetoresistance .

MTJ Magnetic Tunnel Junction .

NR Neuromorphic computing .

NVM Non Volatile Materials .

OM Optical Microscope .

OS Organic Semiconductors .

OSV Organic Spin Valve .

PCM Phase Change Memory .

PC Parallel computing .

pdf Probability Density Function .

PFM Piezorisponse Foce Microscopy .

PID Propoertional Integral Derivative .

PI Paramagnetic Insulator .

PMMA Resist Polymer .

PMT Photomultiplier Tube .

P Polarisation .

PSPD Position Sensitive Photodetector .

PVD Physical Vapour Deposition .

Re Reynolds .

RF Radio Frequency .

RMS Root mean Square .

RNN Recurrent Neural Networks .

RRAM Resistive Random Access Memory .

RT Resistance Temperature characteristics .

SEM Scanning Electron Microscopy .

SE Secondary Electrons .

SMU Source Measure Unit .

SNN Spiking Neural Networks .

SO Spin Orbit interaction .

S Spin .

SV Spin Valve .

TMR Tunneling Magnetoresistance .

UHV Ultra High Vacuum .

VCM Valence Change Memory .

vdW van deer Waals .

VMM Vector Matrix Multiplication .

WGen WaveFunction Generator .

Chapter 1

Introduction

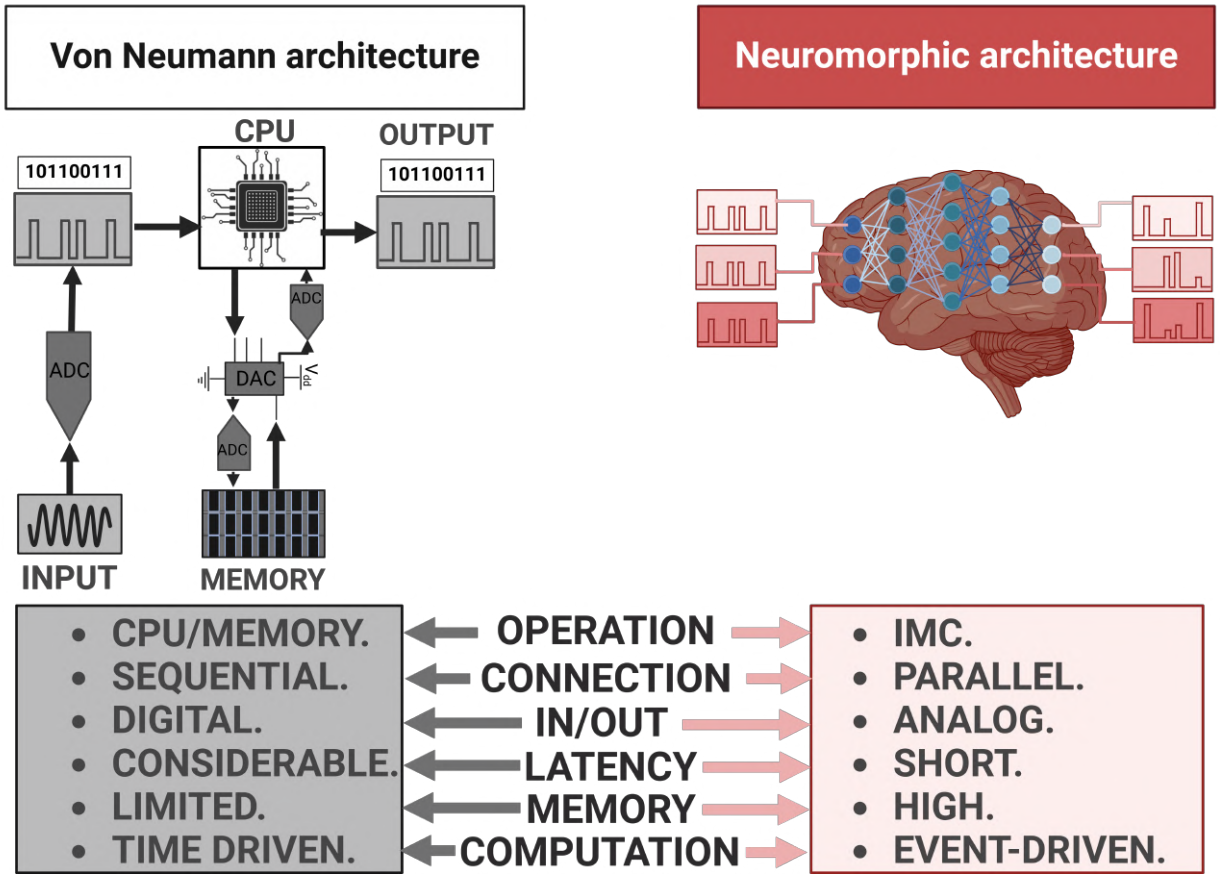

Figure 1.1: Illustrative image of Von Neumann computing architecture, and Neuromorphic computing architecture(inspired by [1]).

Due to the diversity of NC compared to traditional computing, many new research fields emerged in search for new non-volatile (NV) materials, circuits and hardware engineering, and training methods.

1. Many materials were suggested to be used in this new computing technique. The most promising are resistive switching materials that may exhibit a NV resistance change as a response to an external applied stimuli such as:

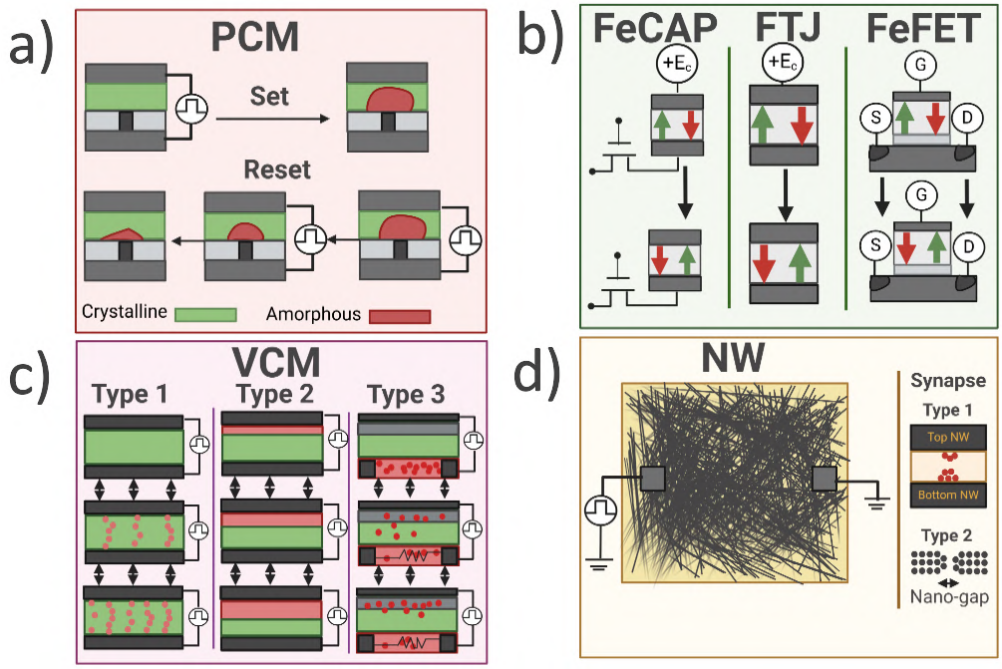

Figure 1.2: a) Phase change material device, showing a crystalline/amorphous continuous phase change upon heating (set), initiated by a positive pulse, and intermediate state in the reset process, achieved by partial negative pulses. b) Different models of ferrroelectric material devices. c) Different types of valence change material devices, type 1 filamentary, type 2 interfacial, and type 3 redox-transistor. d) Conductive NW networks, and different synapses(inspired by [2]).

- Phase-change materials (PCM) can exhibit a non volatile resistance modification, due to the reversible stable crystalline and amorphous phases, controlled by heating. The coexistence of the two phases may also be realized, therefore, these devices may experience a continuum of resistances, limited by the crystalline phase 'LRS', and amorphous phase 'HRS' [16].

- Ferroelectric materials exhibit a reversible resistance modification, due to the bipolar domains polarization configuration, reversibly switched by an applied voltage larger than the coercive voltage V_d [17].

- Valence change materials (VCM) can exhibit a reversible resistance modification due to ionic drift. Upon migration, many mechanisms can manifest such as the formation of conductive filaments (of migrated ions, unbounded metals or formed complexes) [18,19], interfaces(through oxidation processes), or redox reactions [15,20].

- Electrochemical metallization cells (ECM) exhibit a reversible resistance modifica-

tion due to electrically induced ionic migration. Migrated ions are then attracted toward the other extremity, where they start to deposit, and form conductive bridges between the two electrodes, thus short circuiting the two [21].

- Nanowire networks (NW) can exhibit resistance modification due to filament formation between overlapping NW conductive cores, or by nanogaps, initiated by an applied pulse. NW networks were introduced to emulate brain's random neural connections, and high synapses density, the device structure is based on a highly dense mesh of conductive NWs, covered by an outer insulating shell, randomly drop-casted ontop of a substrate [22].

These materials offer numerous advantages such as size down to 2 nm [23], low production cost, 3d stacking compatibility etc. However, almost all these models have common issues regarding uncontrollable intermediate states, endurance, heat tolerance, unstable on/off, temperature sensitive switch and other issues that must be addressed first before mass production.

2. To achieve high connectivity, many architectures were adopted, the most promising is the crossbar geometry(fig. 1.3), due to the high number of cross-points between rows and columns (high synaptic density, between neurons) and the easy to fabricate structure; However, other geometries have also been used, such as NW random growth, used for reservoir computing. To implement these devices on a large-scale application, many hardware approaches were adopted, traditional DL accelerators were adjusted to allow NC, while new brain inspired operation (SNN), and other physics related principles were proposed:

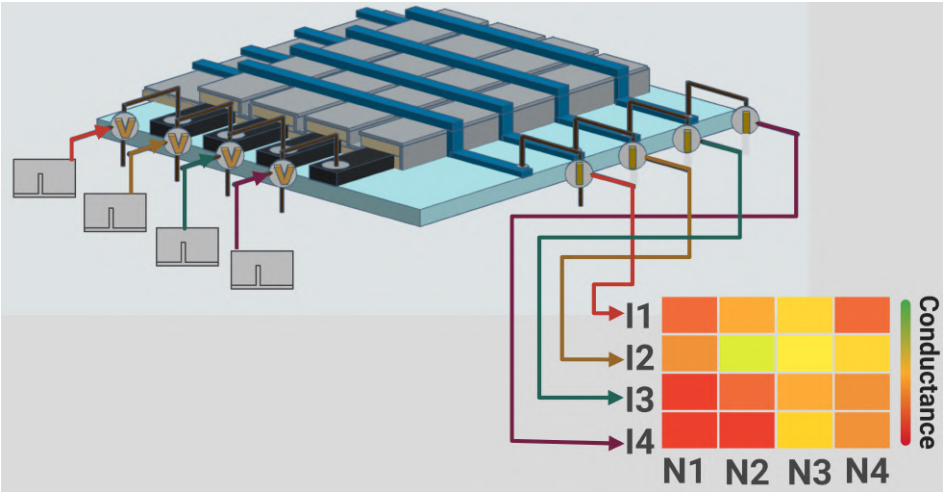

Figure 1.3: 4x4 crossbar hosting 16 devices, used to perform a VMM.

- Deep learning accelerators have shown to be achievable using memristors, and hybrid (memristor/CMOS) units [24], while various deep learning (DL) models, including perceptrons [25], multiple layer perceptrons (MLPs) [26], long short-term memory (LSTM) based recurrent neural networks (RNNs), and convolutional

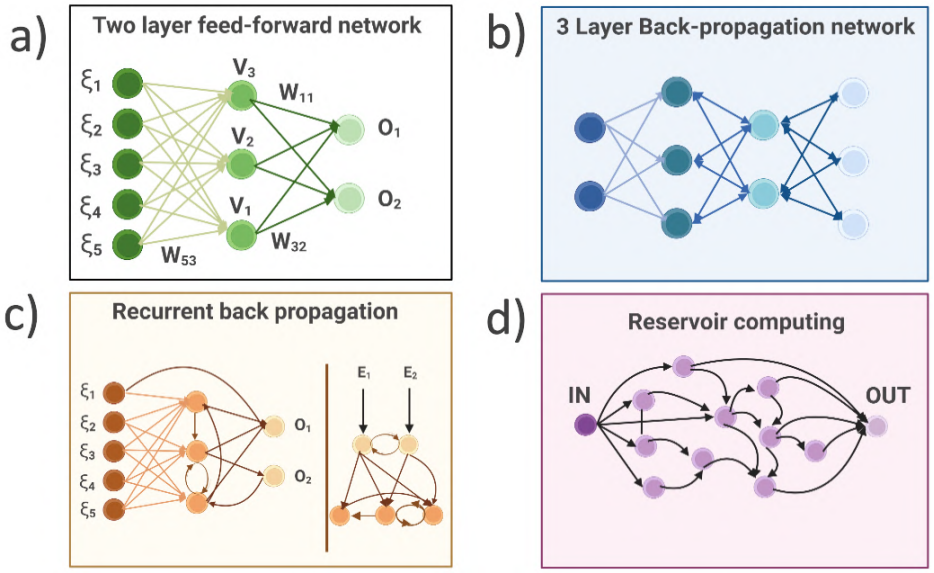

Figure 1.4: Some used forward, and recurrent learning neural networks [3,4].

neural networks (CNNs) [27], have demonstrated applicability using memristors, for most typical supervised, unsupervised, and reinforced learning algorithms.

- Additionally, non-traditional hardware engineering based on spiking neural networks (SNNs) have been introduced. In this approach, crossbar geometry is used, composed of bottom electrodes that acts as inputs, top electrodes that acts as neurons, separated by memristive materials used to weight the generated current (fig.1.3), each row is connected to an integrate and fire soma held at the corner of the array. Overtime, voltages are supplied trough the inputs, resulting currents at the neurons, weighted by the synapses conductance, the currents are then integrated over time, once surpassing a certain threshold, an electrical pulse (spike) is released, in this technique both storage and computing are performed through spikes [28,29]. Spike information coding can be based on different features of the generated spikes, such as rate within a given time window, latency between successive spikes, phase with respect to a background signal, population etc. [5](fig.1.3).

- Other emerging hardware approaches inspired by neuromorphic and physics based principles were also introduced, that by default, follow a spontaneous optimization (path to solution) mechanism. These meta-heuristic approaches includes simulated annealing (quantum-based annealers [30,31], CMOS based annealers [32,33]), evolutionary algorithms [34],probabilistic bit logic [35,36], and models such as Boltzmann machines [37], and Ising model [38,39](otical and coherent Ising machine [40,41]).

- More complex hardware designs were also suggested, that consists on heterogeneous neuromorphic accelerators, housing different neuromorphic technologies, each optimized to perform a certain task.

3. Being a brain-like computing technique, NC was set to address many applications, that

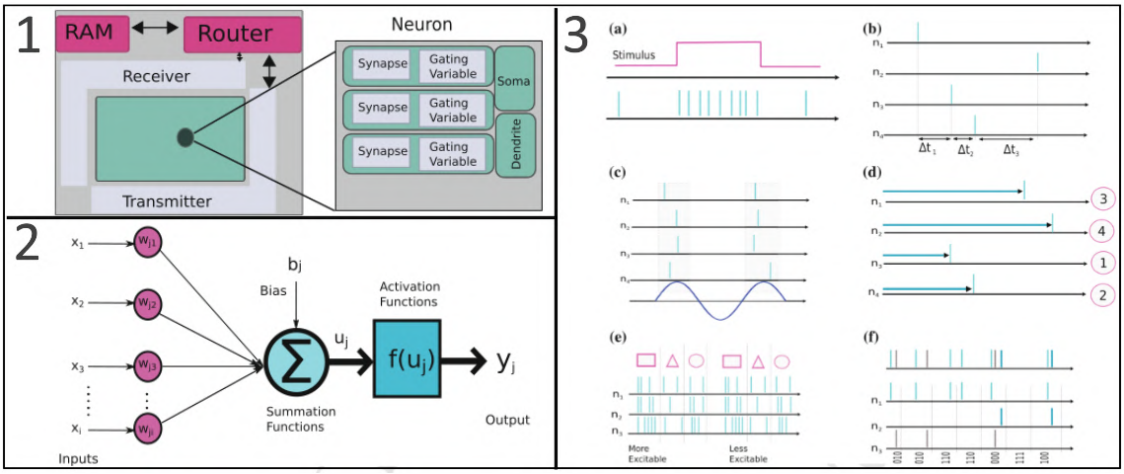

Figure 1.5: 1) A chip of neuron elements, an asynchronous digital transmitter for sending the events generated by the neurons, a receiver block for accepting events from other sources, a router block for communicating packets among chips, and a memory blocks for supporting different network configurations.2) Integrate and fire functionality.3) Spike information coding strategies a) Rate coding. b) Latency coding. c) Phase coding. d) Rank-coding (spike-order coding). e) Population coding. f) Sparse coding (taken from [5]).

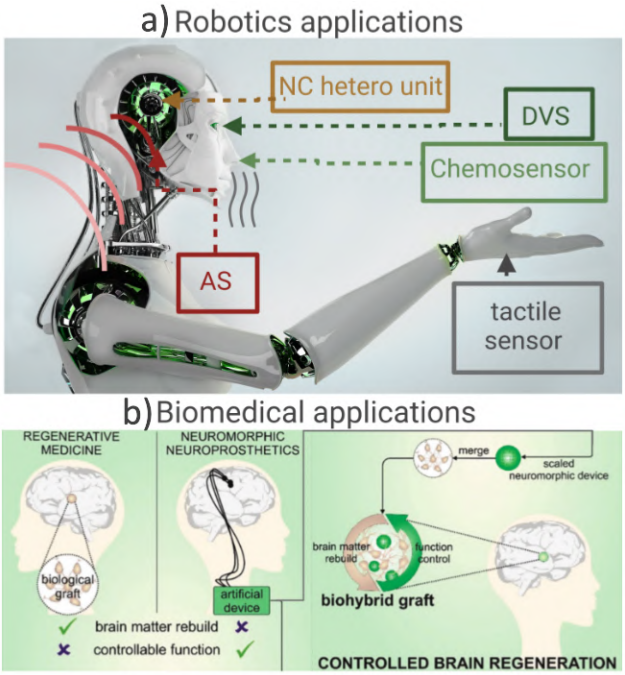

Figure 1.6: Neuromorphic hardware implantation in a) robotics (Motor control, and event driven sensors), and in b) biomedical applications, for artificial brain cells regeneration [2].

are not possible to be optimized by traditional Von-Neumann computing, due to many fundamental issues, most are centered around short latency applications, such as event driven sensors in robotics, and dynamic vision sensors in self driving cars, but also for

data storage, and even for biological brain applications(fig.1.6):

- In robotics, neuromorphic devices were set to tackle three main areas, visual perception, with suggestions of using neuromorphic based even driven visual sensors [42, 43], input conversion into a useful signal to be sent to the motor, done by a neuromorphic in or near sensor commuting [44], and motors control (reaction generation) [43, 45]. Other sensing related applications were also suggested, such as in chemosensors for olfaction, and chemosensation [46, 47], and in audition sensors [48], for an artificial hearing, and other audio related tasks such as speech recognition etc. [49].
- In self driving cars, for neuromorphic dynamic vision sensor (DVS), to encounter many related problems that limits the achievement of high ADAS in traditional DVS, such as the considerable latency among other.
- In biomedical brain applications [50], NC offers a more advantageous brain dysfunctions treatment over the already in use electronic devices [50–52], but also was suggested for brain cells regeneration using artificial neuromorphic neuroprosthetics, to create a biohybrid graft.

The main topic of this thesis is centered on two different resistive switching materials, and their potential application in NC. The work will encompass fabrication, imaging, and characterization of two different memristors, through methods such as IV, MR, SEM, and AFM.

Chapter 2

Theoretical background

2.1 Ferromagnetism

2.1.1 Introduction

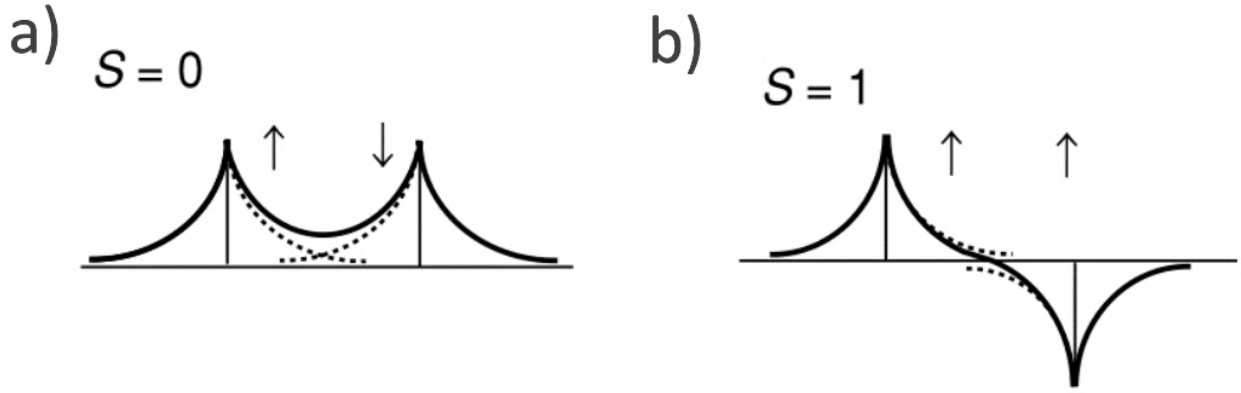

Figure 2.1: Possible electron-electron bond, a) parallel orbit, anti-parallel spin configuration $|\uparrow\downarrow>$, and b) anti-parallel orbit, parallel spin configuration $|\uparrow\uparrow>$(taken from [6]).

Ferromagnetism is a magnetic state, exhibited by some materials such as cobalt, and iron. These materials have a huge permeability μ, caused by an internal magnetic response M to applied magnetic fields(equ.2.1).

$$B = \mu H = \mu_0(H + M) \tag{2.1}$$

The huge magnetic permeability μ, is mainly due to electrons intrinsic spins S. As atoms starts to condensate, their energy levels overlap, and valence electrons bond to each other following Pauli's exclusion principle, which results two possible configurations, parallel spin, anti-parallel orbit, or anti-parallel spin, parallel orbit, with a total intrinsic spin S=[1,0] per bond, in some materials valence electrons are more energetically favorable to form a

parallel spin, anti-parallel orbit(anti-bonding), and in addition the presence of a non vanishing exchange integral, these materials will exhibit a spontaneous M, below certain temperature T_C.

The exchange interaction between the materials spins can be direct(short-range), limited to nearest neighbors, or indirect(long-range $\propto 1/r^2$), metals only experience direct interactions, while insulators experience both, due to the absence of conduction electrons that usually screens long-range effects in metals, which can result different types of interactions such as super exchange, double exchange in some oxides, anisotropic exchange etc.

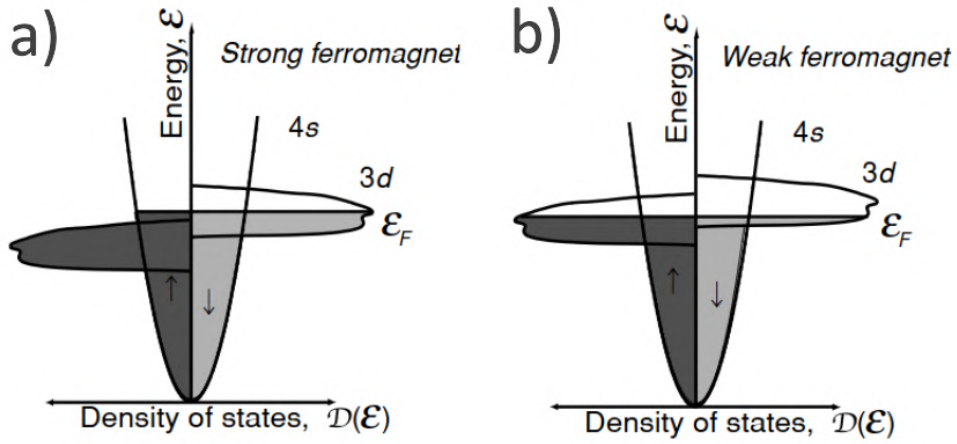

Figure 2.2: Schematic densities of states for a strong and a weak ferromagnet. The $3d^{\uparrow}$-band is full for the strong ferromagnet(taken from [6]).

The exchange interaction can be described by the Heisenberg Hamiltonian:

$$\hat{\mathcal{H}} = -2 \sum \mathcal{J}_{ij} S_i \cdot S_j \tag{2.2}$$

$\mathcal{J}$ = the exchange integral.
For $\mathcal{J} > 0$,electrons spins are parallel aligned, and the material show an FM.
For $\mathcal{J} < 0$,the spins are anti-parallel aligned, and the material is a non FM(fig.2.2).

Since ferromagnetism is an ordered state, it is temperature sensitive,limited by the Curie temperature T_C , above which, thermal fluctuations randomize the orientation of domains magnetizations, thus resulting a zero net magnetization. In this case the material follow a second order ferromagnetic/paramagnetic phase transition.

Ferromagnetic materials can be soft or hard, determined by the crystal properties such as the exchange interaction, and magnetic anisotropies. Hard FM are characterized by a high coercivity, making them difficult to magnetize, but also a big remanence, which allows them to preserve their magnetization over a long period of time. Soft magnetic materials on the other hand, have a very small coercivity, and an almost negligible remanence, making them easy to magnetize and demagnetize(fig.2.3).

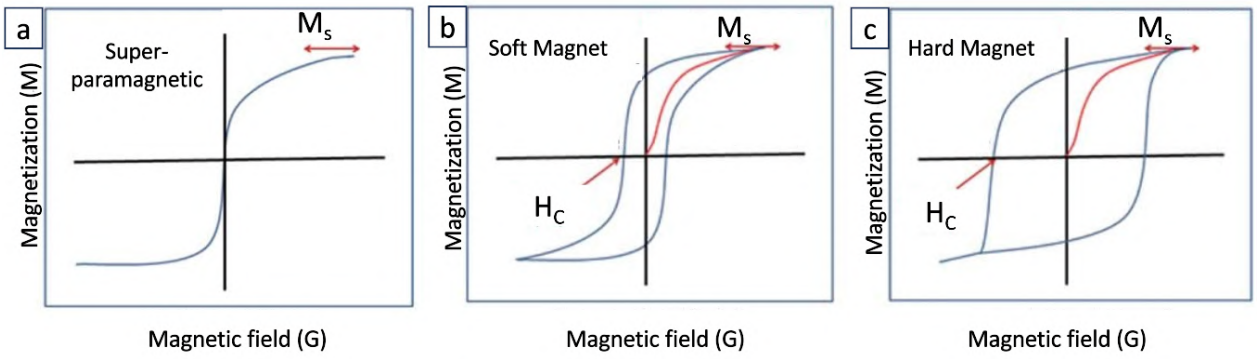

Figure 2.3: Magnetization hysteresis loop of a) super-paramagnetic, b) soft ferromagnetic, and c) hard ferromagnetic materials.

2.1.2 Magnetic Domains

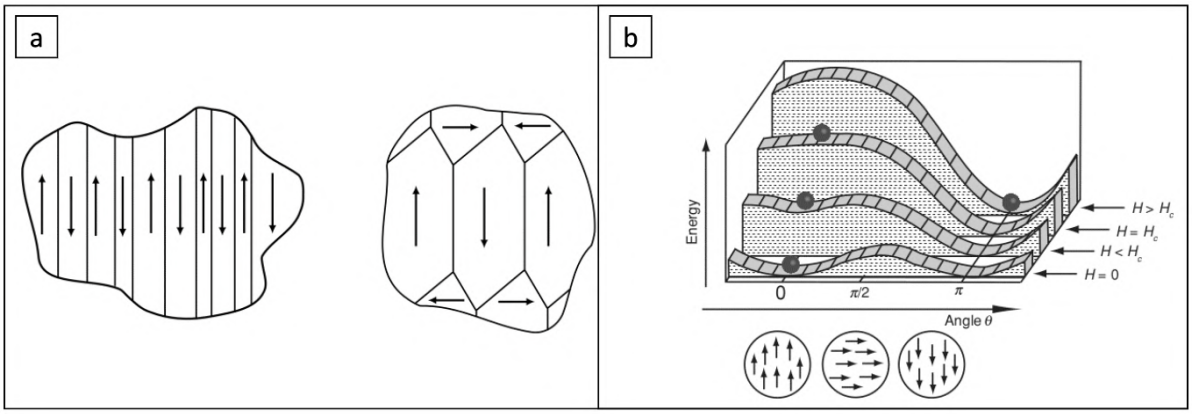

Figure 2.4: a) Domains magnetizations alignment, in the presence of a uniaxial easy axis, and along two axis. b) An energy landscape with metastable minima gives rise to remanence and coercivity(taken from [6]).

In macroscopic systems, singularities such as vortices, dislocation, defects, walls form as a result of energy minimization. Ferromagnetic materials tend to form magnetic domains to reduce the overall energy ϵ_d (equ.2.3) of the system. In most cases, each domain has its own saturation magnetization and direction limited by domain walls.

$$\epsilon_d = -\frac{1}{2}\int H_d(r) M dr^3 \tag{2.3}$$

ϵ_d = the energy term, expressed in terms of the volume integral of the dipole field $H_d(r)$.

For a non-magnetized material, in the absence of magnetic anisotropy, the magnetizations of the domains randomly orient, resulting a zero net magnetization. However, in most cases, FM materials have direction dependent magnetic anisotropy(shape,magnetocrystalline, induced), caused by the lattice cell, and/or crystal size, crystal deformation (see. (2.1.3)etc.

At equilibrium, the magnetic domains will tend to align in a given direction, but with random orientation, resulting a zero net magnetization. If the FM is subjected to an external field H, higher than the coercive field H_c , all the domains magnetizations will align with the field H, resulting a magnetization saturation. After the field is removed, the deformed domains magnetizations rearrange, to re-achieve the initial equilibrium state, this will be observed experimentally as a magnetization hysteresis loop.

2.1.3 Magnetic anisotropy

Magnetic anisotropy describes an angle dependent energy distribution in magnetic systems (equ.2.4), as a consequence, the system will have an easy axis in a certain direction, upon which the magnetization alignment will result an energy minimum.

$$E_a = K_1 sin^2\theta \tag{2.4}$$

where θ is the angle between M and the anisotropy axis, K1 has units J/m^3, with values that may range from less than 1 kJ/m^3 to more than 20 MJ/m^3. Magnetic anisotropy is observed in materials that have different dimensions, applied forces, or crystal symmetries, and can be caused by:

1. Shape anisotropy: as a consequence of surface poles formed at the edges of an FM, a demagnetizing field is generated between the opposing poles, with direction opposite to that of the magnetization. In it's simplest forms, H_d have a linear dependence on the magnetization(in spherical shapes)(equ.2.5). If the H_d formed between poles is not homogeneously distributed over the material's geometry, magnetization will be subjected to different fields, that will modify it's orientation to follow the direction with the smallest H_d.

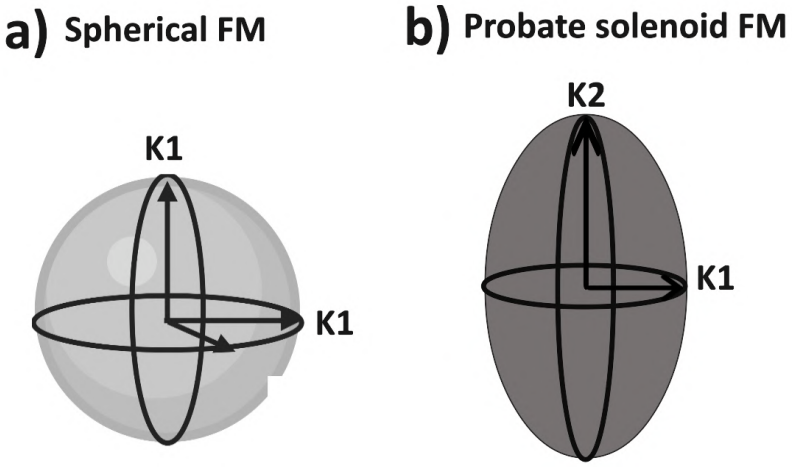

Figure 2.5: a) Spherical FM with an isotropic demagnetization field. b) Prolate spheroid with an easy axis in the z direction.

Shape anisotropy energy can be estimated as the energy difference between the easy

and hard axis configuration(equ.2.6). The internal magnetic field:

$$H_k = (H_0)_k\text{-}\gamma_k(M_0)_k \tag{2.5}$$

γ = demagnetization factor.
H_0 = applied uniform external magnetic field.
$(M_0)_k$ = magnetization at a given direction k.

$$\Delta\epsilon_m = \frac{1}{2}\epsilon_0 V M_s^2[\frac{1}{2}(1\text{-}N)\text{-}N)] \tag{2.6}$$

N = demagnetizing factor in an easy direction.
N'= $\frac{1}{2}$ (1 - N). demagnetizing factor perpendicular to the easy axis.
Shape anisotropy affected by domains, thus it is mostly effective for small systems, where it can reach up to 200 kJ/m^3.

2. Magnetocrystalline anisotropy is a crystal symmetry related magnetic anisotropy, generated from crystal-field, spin-orbit coupling, and/or dipole–dipole interactions. Different crystal symmetries, may result different anisotropy, with different energies and energy relations:
Hexagonal lattice cell:

$$E_a = K_1 sin^2\theta + K_2 sin^4\theta + K_3 sin^6\theta + K_3' sin^6\theta sin6\phi. \tag{2.7}$$

Tetragonal Lattice cell:

$$E_a = K_1 sin^2\theta + K_2 sin^4\theta + K_2' sin^4\theta cos4\phi + K_3 sin^6\theta + K_3 sin^6\theta sin4\phi. \tag{2.8}$$

Cubic lattice cell:

$$E_a = K_{1c}(\alpha_1^2\alpha_2^2 + \alpha_2^2\alpha_3^2 + \alpha_3^2\alpha_1^2) + K_{2c}(\alpha_1^2\alpha_2^2\alpha_3^2). \tag{2.9}$$

α_i = are the magnetization direction cosines.

Hexagonal anisotropy(equ.2.8) can be simple-uniaxial, along an easy axis, or along easy plane/cone(fig.2.6):

- For $K_1 = K_2 = 0$, the FM is isotropic.
- For $K_1 > 0$ and $K_2 > -K_1$: the c axis is an easy axis.
- For $K_1 > 0$ and $K_2 < -K_1$: the basal plane is an easy plane.
- For $K_1 < 0$ and $K_2 < -K_1/2$: the basal plane is an easy plane.
- For $-2K_2 < K_1 < 0$: the ferromagnet has an easy cone .

Cubic structures(equ.2.9) can experience more complex anisotropy, usually along 3 different axis, labeled as easy,medium, and hard, determined based on K_{1c}, and K_{2c}.

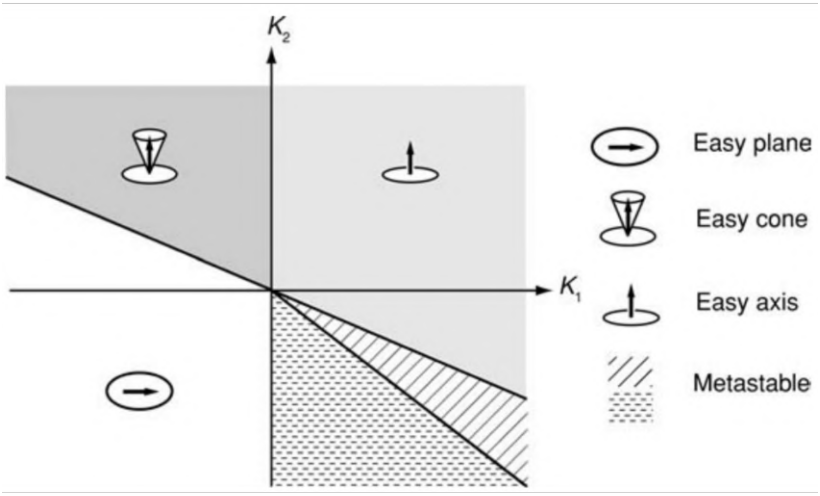

Figure 2.6: Magnetic phase diagram for uniaxial magnets. In the metastable regions, there are two energy minima, at $\theta = 0$ and $\theta = \pi$ /2(taken from [6]).

3. Induced anisotropy: is an artificial anisotropy, introduced by external forces. One way to form an easy axis, is by applying an external magnetic field, during a thermally activated diffusion in some alloys such as $Ni_{80}Fe_{20}$(fig.2.7). Easy axis can also be introduced by an applied stress, that can lead in simple cases to a uniaxial axis formation with a magnitude,$K_{u\sigma} = 32\ \sigma\lambda_s$. λ_s is the saturation magnetostriction.

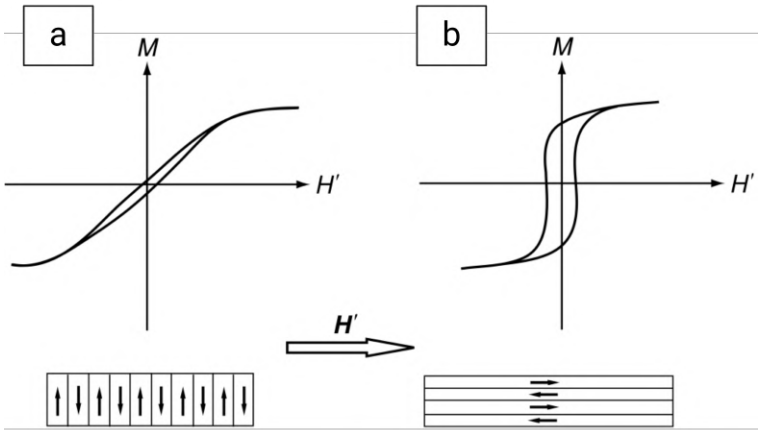

Figure 2.7: Magnetization of a thin film with induced anisotropy created by annealing in a magnetic field. a) 'sheared' hysteresis loop, observed when H is applied perpendicular to the alloy's domains magnetizations. b) Open loop, observed after the formation process was performed, while applying H parallel to the alloy's domains magnetizations.(taken from [6]).

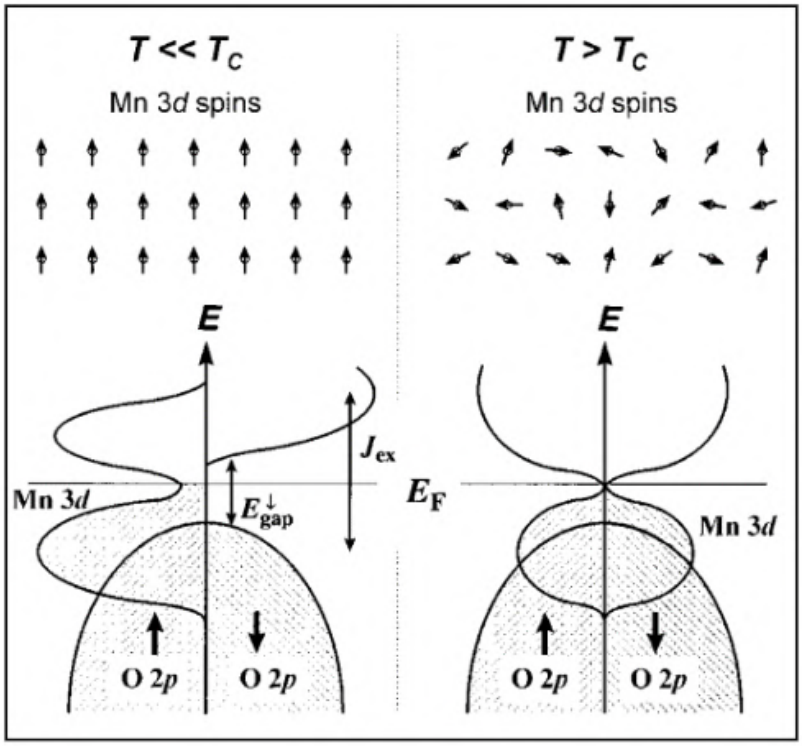

Figure 2.8: a) Energy band below T_C, showing a Fermi level in the conduction band for the majority spins, and a bandgap for minority spins density of states (taken from [7]).

2.1.4 Half metals

Half metallicity is a phenomenon experienced by some FM alloys, such as manganese perovskite, $La_{0.7}Sr_{0.3}MnO_3$(LSMO). Below T_C, these materials have a metallic behavior for one spin polarization, and an insulating behavior, for the other. This corresponds to the formation of an energy gap for minority spin density of states. Upon charge transport these materials can result completely spin polarized currents up to 100% theoretically.
Close to T_C, order is destroyed by thermal fluctuations, and the material follows a second order FM/paramagnetic phase transition. At temperatures near T_C a huge colossal magnetoresistance (CMR) will be observed(due to the FM/Insulator phase change), while at temperatures higher than T_C, this material behaves as a normal insulator [7].
This remarkable property made them of a great interest as spin injectors in spintronics(exp. in spin valves).

2.2 Organic semiconductors

Organic semiconductors are materials composed of low molecular weight materials and polymers. Carbon atoms tend to form an sp2 hybridization, by promoting an s electron to the empty pz orbital, then two states are formed between the molecules, an in plane σ bond, due to a direct binding between the molecules s, px and py electrons, and a second

state perpendicular to the plane π, formed by an indirect bonding between pz electrons of the two atoms. Valence electrons may follow a bonding process, leading to parallel orbital, anti parallel spin configuration, and form a stable σ,π bonds, or an anti-bonding process, by an anti parallel orbit, parallel spin configuration, leading to an unstable $\sigma*$, $\pi*$ states. The molecular energy levels can be represented by two regions, filled states, represent stable σ, and π energy levels, and empty states, of excited $\sigma*$, and $\pi*$ energy levels [8].

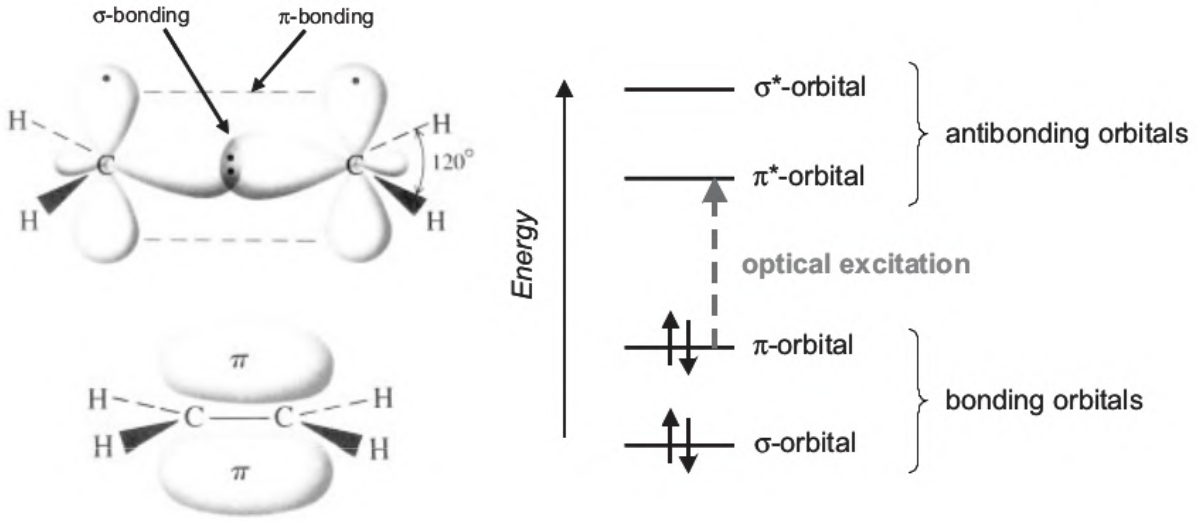

Figure 2.9: Different types of bonding between two molecules, and their energy levels (taken from [8]).

At close separating distances, molecules may form crystals, via inter-molecular Van der Waals bonds, however, with a lower melting point and hardness compared to the covalently bonded inorganic counterparts, due to the weak bonding forces.

Molecular semiconductors are characterized by a completely filled HOMO, and empty LUMO bands, separated by a small bandgap that lies for most components in the visible range. Free carriers can be generated by molecular energy absorption (thermal-photon-electrical etc.), leading to molecular excitation(mostly π-π^* transition), that may lead to (electron-hole) generation free to move in the LUMO band in between molecules. After a period, the free charge can encounters another excited molecule (a vacancy in the HOMO), then the free charge fill the vacancy, thus stabilizing the molecule(π^*-π transition), and releasing energy (phonon/photon) in the visible range.

Charge transport in OS can range between two extreme mechanisms, band transport in highly ordered crystals, while through hops in disordered amorphous solids :

- Band transport in OS, is usually observed in highly purified molecular crystals [8], the mobility have the same temperature dependence as it's inorganic counterparts, $\mu \propto T^{-n}$ with n = 1, however at much lower magnitudes(1 to 10 cm^2/Vs at room temperature).
- In amorphous OS solids, the random distribution of molecular orbitals result a Gaussian distribution of HOMO-LUMO state. In this case charge transport manifest via hopping

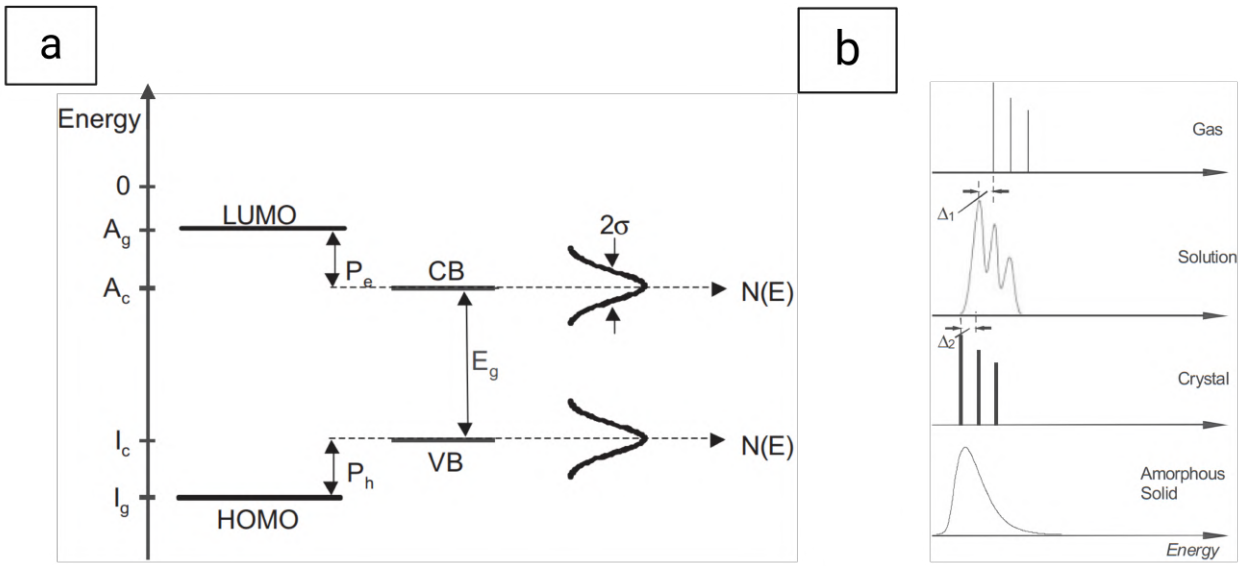

Figure 2.10: a) Energy states distribution for a single molecule, crystal, and amorphous solid. b) Absorption energy spectra comparison between different phases(taken from [8]).

mechanism between localized molecular orbitals, resulting in a much lower mobility ≈10^{-3} cm^2/Vs, that depends on both temperature and applied electric field (equ.2.10).

$$\mu(F,T) \propto exp(-\Delta E/kT).exp(\beta\sqrt{F}/kT) \tag{2.10}$$

Charge transport in MS is affected by many parameters such as charge carrier density(equ.2.11), and the effective density of states N_0. MS charge density is orders of magnitude lower than the inorganic SC. To overcome the low intrinsic carriers density, carriers can be injected to the system, either by doping, direct contact injection, or photo-generation.
$n_{OS} \approx 1cm^{-3}$ for a typical E_g=2.5eV, and N_0=10^{21} cm^{-3}.
n_{Si}=10^{10} cm^{-3}, for an E_g=1.12eV, and an N_0=10^{-19} cm^{-3}.

$$n_i = N_0.exp(-E_g/2kT) \tag{2.11}$$

Amorphous semiconductors are characterized by having a Gaussian HOMO-LUMO energy distribution, with an energy gap(E_g=[1.5;3]eV) that lies in the visible range, thus they are perfect white light absorbers (fig.2.10). Other important optical property in MS, is related to the presence of a well defined spin states(singlet| $\uparrow\downarrow\rangle$/triplet| $\uparrow\uparrow\rangle$), and a weak crossing between the two, which sets a higher limit for electroluminescence quantum efficiency in OLEDs.

2.2.1 Tris(8-hydroxyquinoline)-A(III)

Tris(8-hydroxyquinoline)- A(III) is a molecular semiconductor that consist on a coordination complex between an A post transition metal(III), such as Al, Ga, and three quinoline lig-

ands(fig.2.11). Apart from being the most used molecules in OLEDs, these molecules are also

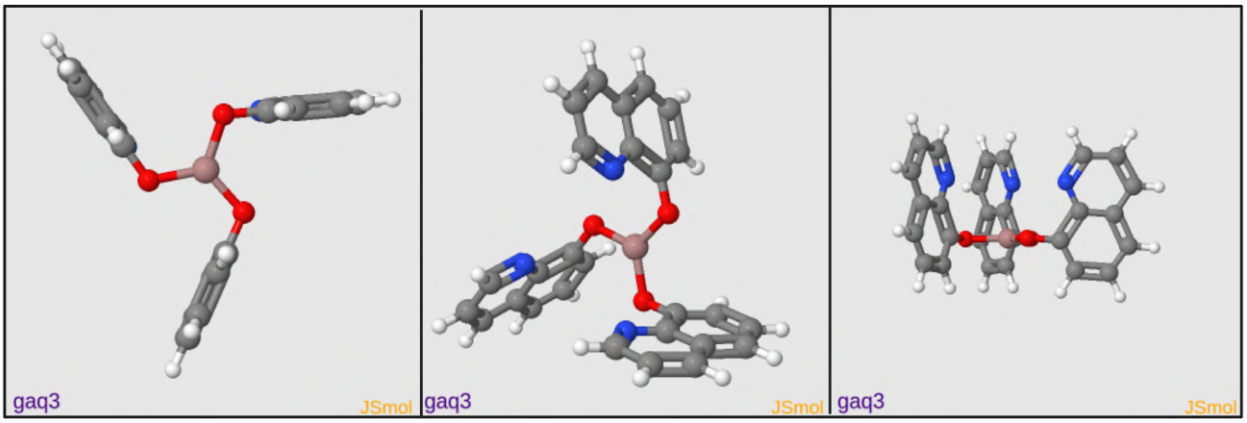

Figure 2.11: Aluminum(III) Tris(8-hydroxyquinoline)(Alq_3) molecule.

used in spintronic applications due to their efficiency in spin and charge transport [15,53], mainly due to the low spin-orbit, as a result of the small atomic numbers constituting these materials, and particular molecular structure, and the suppressed hyperfine interactions, due to the use of integer atomic number atoms (D^2 instead of H^1 etc.). These materials have shown extremely long spin-orbit, and hyperfine related spin relaxation time, up to a milliseconds observed experimentally, and even seconds theoretically [54], therefore, they are very efficient in spin transport.

$$\lambda_s = \sqrt{(D_{hop} + D_{ex})\tau_s} \tag{2.12}$$

With D_{hop}, and D_{ex} the spin diffusion constants due to hopping, and exchange coupling, consecutively, while τ_s is the spin relaxation time.

2.3 Charge transport in disordered solids

In sufficiently disordered solids such as amorphous MS, oxides, polymers... Bloch's band theory no longer applies, instead, energy states must be considered as localized. Unlike band transport in crystals, disordered solids transport manifest via hopping mechanism between localized states. Hopping may follow many mechanisms(fig.2.12), depending on the type of material, and thickness of the transport medium.

Many models were constructed to describe hopping mechanisms, most of them are solutions to the master equation (equ.2.13) [10].

$$\frac{\partial}{\partial t} f_i(t) = -\sum_{j \neq i} W_{ji} \left[f_i(t)(1 - f_j(t)) \right] + \sum_{j \neq i} W_{ji} \left[f_j(t)(1 - f_i(t)) \right] - \lambda_i f_i(t) \tag{2.13}$$

$f_i(t)$ = the probability that the site i is occupied.
$(1\text{-}f_j(t))$ = is the probability that the state j is unoccupied.

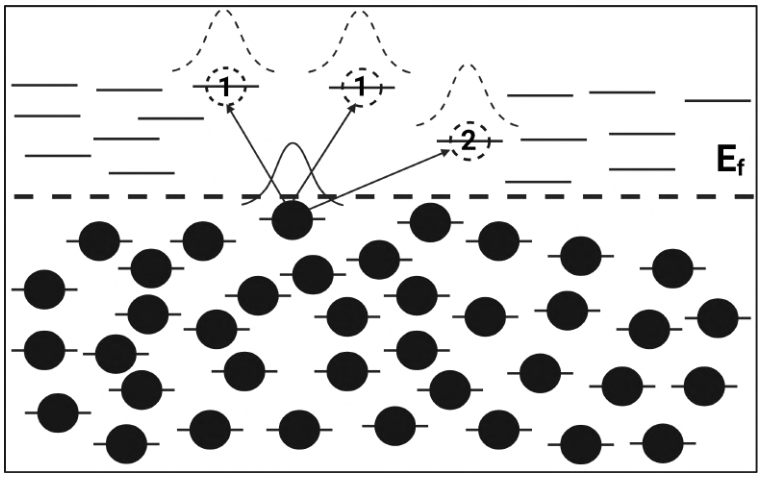

Figure 2.12: 1) Nearest neighbor hopping, and 2) variable range hopping mechanisms between localized states(taken from [9]).

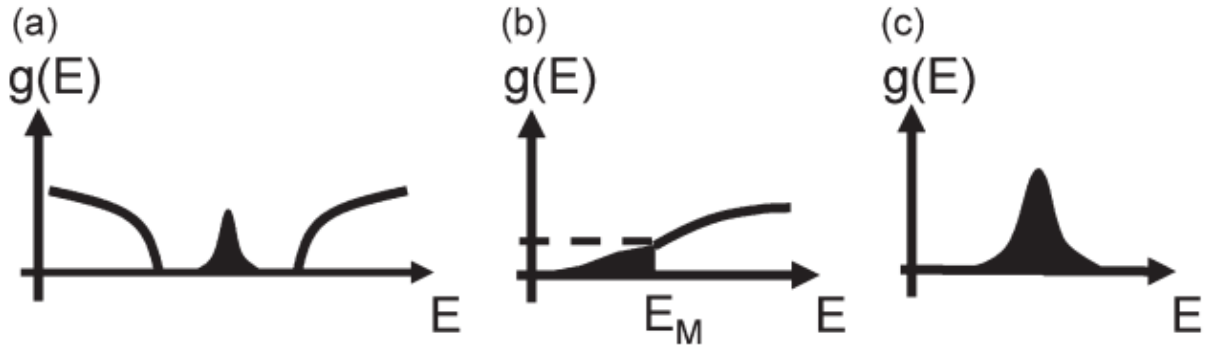

Figure 2.13: a) Traps energy band, in the band-gap. b) Traps levels,located at one of the energy bands. c) Completely separated localized band, generated by free traps (taken from [10]).

W_{ij} = the transition rate from i to j state.
λ_i = the decay rate of the excitation at site i.

To solve the master equation, the transition rate must be evaluated first. Two assumptions where used to find W_{ij}, the first constructed by Anderson, and is based on a phonon-assisted tunneling mechanism, the resultant expression is known as Miller-Abrahams hopping model.

$$W_{ij} = \nu_0 exp(-2\gamma|R_{ij}|) \begin{cases} exp\left(-\frac{(\epsilon_j-\epsilon_i)}{KT}\right), & \text{if } \forall \epsilon_j > \epsilon_i \\ 1, & \text{else} \end{cases}$$

ν_0=Phonon frequency.
γ= the inverse localization radius.
R_{ij}= distance between site i and site j.
ϵ_i/ϵ_j= energy levels of site i and j.

The second model, based on polaronic induced hopping. In this model transition between two sites is only possible if the two have the same energy levels, in other words, when the total energy of the carrier do not change upon hops, W_{ij} was found to be:

$$W_{ij} = \frac{J^2}{\hbar}\frac{\pi}{\sqrt{2U_b kT}} exp\left(-\frac{U_b}{2kT}\right) \cdot exp\left(-\frac{(\epsilon_j - \epsilon_i)}{2kT} - \frac{\beta(\epsilon_j - \epsilon_i)^2}{8kTU_b})\right) \tag{2.14}$$

J= parameter related to the overlap integral, J= $J_0 exp(-2\gamma|R_{ij}|)$.
U_b= polaron binding energy.

Based upon one of the W_{ij} models, many model were constructed to describe hopping using different assumptions to simplify the relation, such as uncorrelated systems, and/or small deviations from equilibrium, which leads to linearization of (equ.2.13). Notable to mention is Mott's variable range hopping (VRH)(equ.2.15),Ambegaokar's Percolation, mean medium approximation of Gaussian(MMA), and energy-space aster equation(ESME)...

$$W_{ij} = \nu_0 exp\left(-\gamma\left(\frac{1}{8\gamma\kappa\pi\rho}\frac{1}{T}\right)^{1/4} - \frac{1}{\kappa T\frac{4}{3}\left(\frac{1}{8\pi\gamma\kappa\rho}\frac{1}{T}\right)^{3/4}\rho}\right) \tag{2.15}$$

$W_{ij} \propto exp\left[-\left(\frac{T_0}{T}\right)^{1/4}\right]$.
To computationally describe hopping models, other approach was introduced by Bässler, based on Monte-Carlo simulations. The main difference between Bässler's MC, and the master approaches, is that one is based on averages via computationally intensive renders of particles, while the other deals with averages via occupation probability.

Bässler and Coworkers were able to construct a low-field charge-carrier mobility model(equ.2.16), while other master based mobility expressions discussed in section(sec.2.2)(equ.2.10), show a temperature, field, and localized states concentration dependence(equ.2.17) :

$$\mu = \mu_0 exp\left[-\left(\frac{2}{3}\frac{X}{K_B T}\right)^2\right] \tag{2.16}$$

X = the standard deviation of the Gaussian energy distribution.

$$\sigma = \sigma_0 \exp\left(-\frac{\gamma}{\alpha N_0^{1/3}}\right) \tag{2.17}$$

N_0 = the concentration of randomly distributed sites. σ_0 = concentration independent.
α = is the localization radius.
γ = a numerical coefficient.
As for the temperature dependence of the conductivity, many models were constructed, in

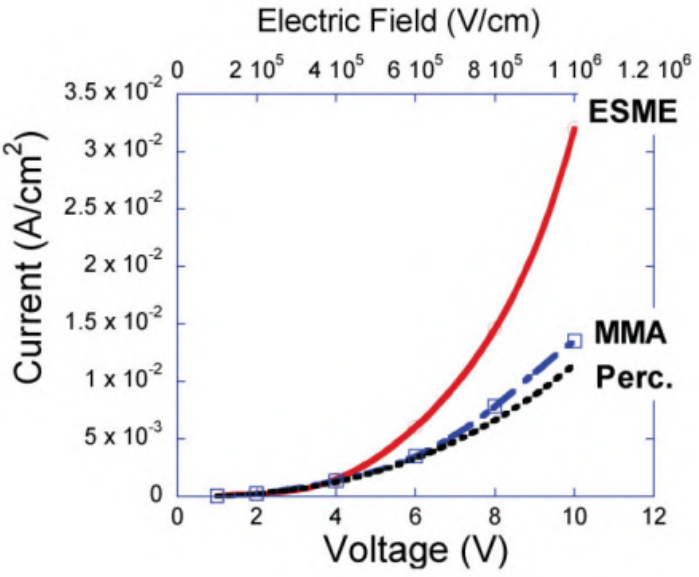

Figure 2.14: Space-Charge-limited current for Perc, MMA, and ESME, using a=1 nm, γ=a/10, T=300 K, σ4kT, ν_0=10^{12} s^{-1}(taken from [10]).

terms of concentration and DOS.

In MIM junctions, transport can manifest between two metal electrodes via direct tunneling if the insulating layer is thin enough. A model was constructed by Simmons [55] to describe direct tunneling for thicknesses below 2 nm (equ.2.18).

$$J = a \times V + b \times V^3 \tag{2.18}$$

a and b: parameters that depends on the shape of the barrier.

For thicker insulating layers, typically above 6 nm, inelastic hopping via chains of multiple localized states was proven to be the most adequate [14] (equ.2.19), the expression shows voltage dependent terms, weighted by the conductance of each channel.

$$G(\Omega^{-1}) = \sigma_0 + \sigma_1 \times V_1^c + \sigma_2 \times V_3^c + ... + \sigma_{N\text{-}1} \times V_N^c \tag{2.19}$$

W:conductance.
σ: conductance at a given channel.
c_n:$\frac{4}{3}$n.
N: the number of hopping channels considered in the model.

$$G(\Omega^{-1}) = \sigma_0 + \sigma_1 \times T_1^c + \sigma_2 \times T_3^c + ... + \sigma_{N\text{-}1} \times T_N^c \tag{2.20}$$

W:conductance.
σ: conductance at a given channel.
c_n:$\frac{4}{3}$n.
N: the number of hopping channels considered in the model.

2.4 Magnetotransport

Ferromagnetism can influence thermal, electrical and optical properties of solids, leading to different magneto-correlated effects such as magnetocaloric, magnetoelectric, and magneto-optical Kerr effects.

Magnetotransport describes electrical transport under the influence of a magnetic field, many magnetorestive and Hall effects fall into this category, to evaluate this effect, the magnetoresistance (MR) is used, and it describes how the electrical resistivity of a sample is affected by an applied magnetic field B:

$$MR = \frac{\rho(\mathbf{B})\text{-}\rho(\mathbf{0})}{\rho(0)} \tag{2.21}$$

Where $\rho(\mathcal{B})$ represents the resistivity influenced by a magnetic field B, and $\rho(0)$ denotes the resistivity in the absence of any magnetic influences.

2.4.1 Anisotropic magetoresistance

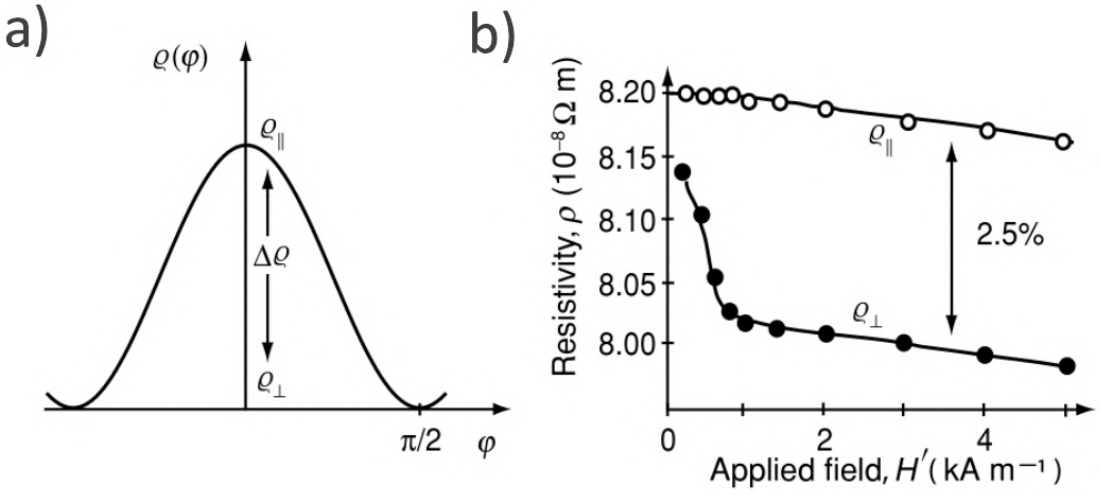

Figure 2.15: a) AMR of a permalloy film, and b) its angular dependence(taken from [6]).

In a spontaneously magnetized FM, conductivity is dependent on the relative orientation of an applied electrical current, with respect to the magnetization direction. This effect is called anisotropic magnoresistance (AMR), and is attributed to the spin-orbit interaction at the (s-d) states, resulting a mixing of up and down spins, thus introducing a scattering probability between up(down) to down(up) spins.

$$\rho(\theta) = \rho_{\parallel} + \Delta\rho_{AMR}.cos^2(\theta) \tag{2.22}$$

θ = the angle between magnetization and applied current direction.
$\Delta\rho_{AMR} = \rho(\parallel)\rho(\perp)$.

2.4.2 Colossal magnetoresistance

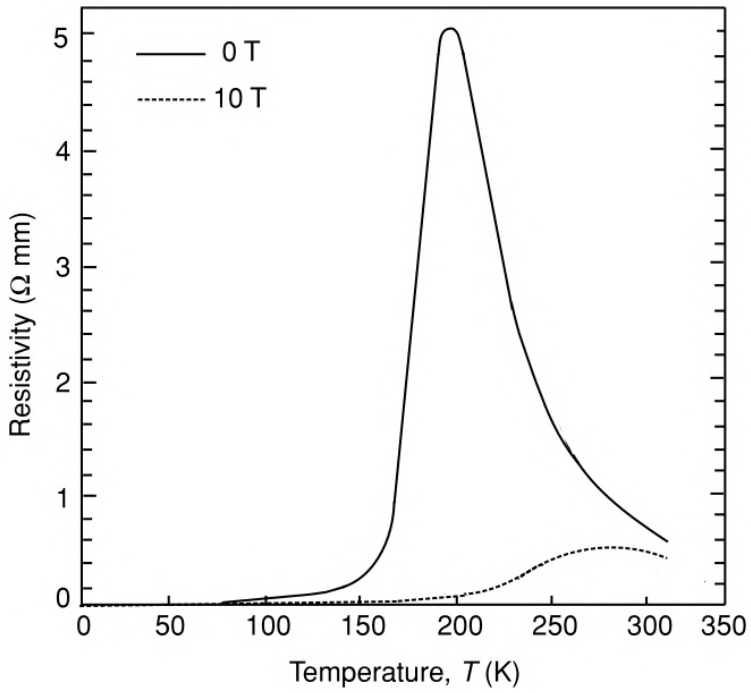

Figure 2.16: Huge, negative CMR effect, observed around T_C, in $La_{0.7}Ca_{0.3}MnO_3$ when subjected to 10 T magnetic field, below T_c, both resistivities decrease, and coincide at very low temperatures, where the CMR is no longer effective.(taken from [6]).

Another MR was observed in double-exchange materials (such as LSMO half-metal). Upon replacing a fraction x of La^{3+} with bivalent ions, approximately 1-x of the manganite adopts the Mn^{4+} state. At a specific fraction x, the structural distortion diminishes, transforming the material into a half-metal below the critical temperature (T_C), and an insulator above. Around T_C, these materials exhibit a remarkable negative magnetoresistive effect, peaked at T_C, known as the colossal magnetoresistance (CMR), caused the FM/Insulator second order phase transition.

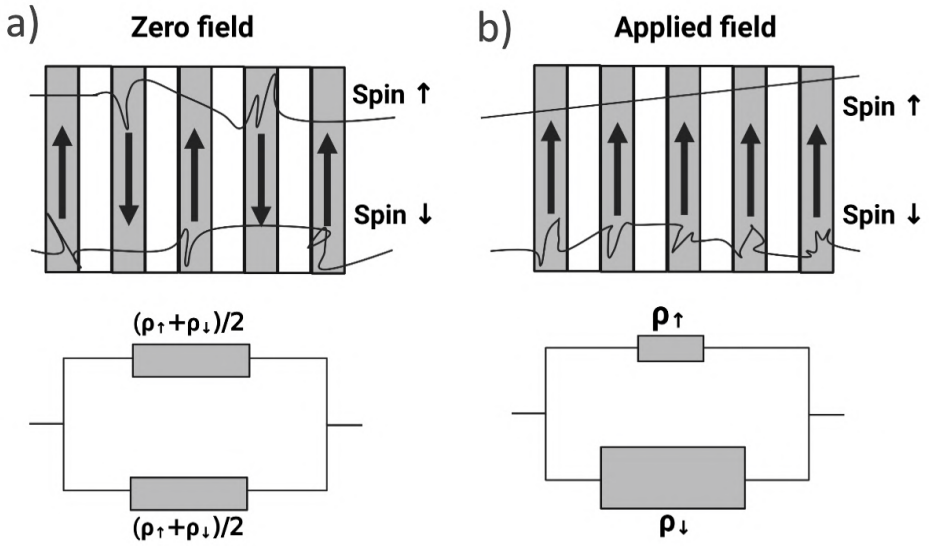

Figure 2.17: A ferromagnetic multilayer separated by a metallic non FM spacer, a) in the absence of a magnetic field, the magnetizations are in an anti-parallel configuration, upon charge transport, both majority and minority will have the same resistance. b) In the presence applied field resulting a parallel magnetization configuration, all magnetizations will align with the field, upon charge transport, majorities will have scattering free, while minorities suffers scattering at each layer, resulting difference in the resistances (taken from(taken from [6]).

2.4.3 Giant and tunneling magnetoresistance

Giant magnetoresistance is another manifestation of magnetoresistive effects, observed when two ferromagnetic (FM) materials are separated by a non-FM, metallic spacer.
This effect was first discovered in 1988 by Albert Fert and coworkers, and Peter Grünberg an coworkers separately, in a Fe-Cu multilayer, where they observed a huge MR reaching up to 40% (fig.2.18).
The mechanism can be understood using Mott's two electrons conduction model. If one spin electrons mean free path exceeds the FM/Spacer stacking period, and differs from the other spin, a GMR is observed, as a consequence of spin scattering of majorities and minorities, mainly at the spacer/FM interface. Typically, the layers are stacked in anti-parallel configuration, under an applied current, the two spins follows a spin scattering based on their orientation relative to the magnetization of the FM layer, causing up-facing spins are scattered by down-facing magnetization, and vise versa. In this configuration the resultant resistance from both spins is identical(equ.2.23). However,if a magnetic field is applied, the FM magnetizations will align with it, and upon transport, majorities experience a spin scattering free transport, while minorities experience scattering at each FM layer. The two configurations have different resistances.
The resistance can be written as(equ.2.24).

$$R_{ap} = (R_{\uparrow} + R_{\downarrow})/2. \tag{2.23}$$

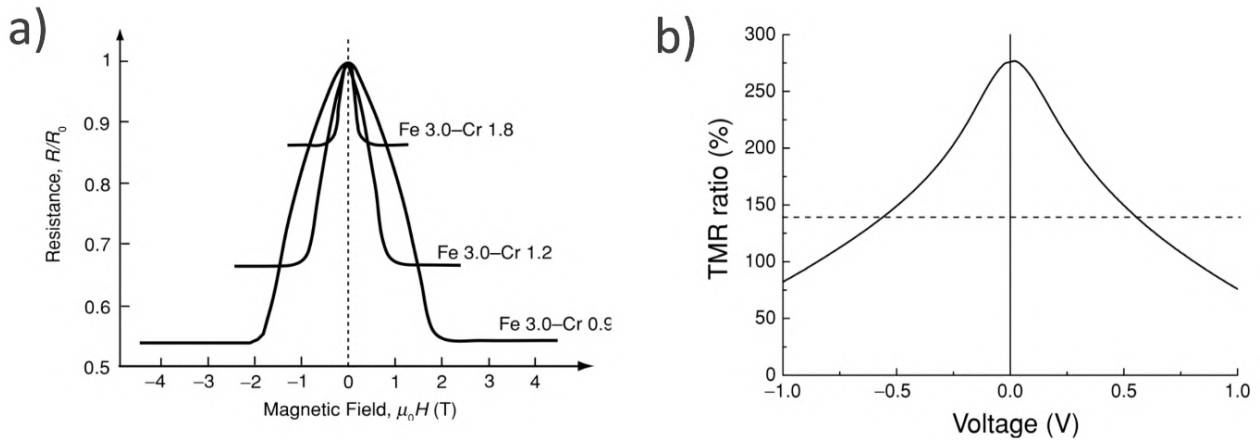

Figure 2.18: a) GMR ratio reported by Fert et. al [11], observed in an FM/Metallic multilayer heterostructure. b) TMR %, measured in an FM/Insulator(MgO) multilayer heterostructure(taken from [6]).

$$R_p^{-1} = R_\uparrow^{-1} + R_\downarrow^{-1}. \tag{2.24}$$

The GMR ratio is defined as the difference between the two configurations, divided by the AP resistance.

$$\Delta R/R = (R_{AP}\text{-}R_P)/R_{AP}. \tag{2.25}$$

If the spacer is an insulator, FM/insulator/FM devices exhibit a tunneling magnetoresistance(TMR)(chap.5). Charge transport in these devices is similar to a MIM, described by [14,55], while for spin transport, devices exhibit a low/high resistive state for a P/AP configuration, switched by an external magnetic field, due to scattering mechanisms discussed for FM/M/FM multilayer.

This effect was fist observed in AlOx spacers, then a bigger effect was reported in MgO. These heterostructure acts as a near-perfect spin filter at P configuration, allowing (almost)only majority related current to be generated, while blocking minority current. The positive TMR values can exceed 200% at room temperature.
To estimate the TMR in terms of spin polarization, a simple model formalized by Jullière can be used(equ.2.26).

$$MR_{max} = \frac{2P_1P_2}{(1+P_1P_2)}. \tag{2.26}$$

where

$$P_i = (D_\uparrow(\epsilon_F)\text{-}D_\downarrow(\epsilon_F))/(D_\uparrow(\epsilon_F) + D_\downarrow(\epsilon_F)) \tag{2.27}$$

D(ϵ_F) = the interfacial density of states at the Fermi level for the particular spin-up or spin-down bands.

Chapter 3

Fabrication processes

3.1 Substrate cleaning and storage

Surfaces represent crystal boundaries with empty space, caused by an abrupt interruption of crystal periodicity, as a result, atoms at surfaces are more energetic than in the bulk, due to missing bonds. To lower their energy, surface atoms reorganize themselves by forming bonds in between, and in most cases, a surface reconstruction manifest, and a new crystal lattice at the interface is formed. Surfaces are the doorways of the crystal bulk, and in direct contact with the crystal surrounding, thus are usually exposed to free molecules in the surrounding environment, that may physically or chemically bond to it (physisorption-chemisorption), resulting surface contamination.

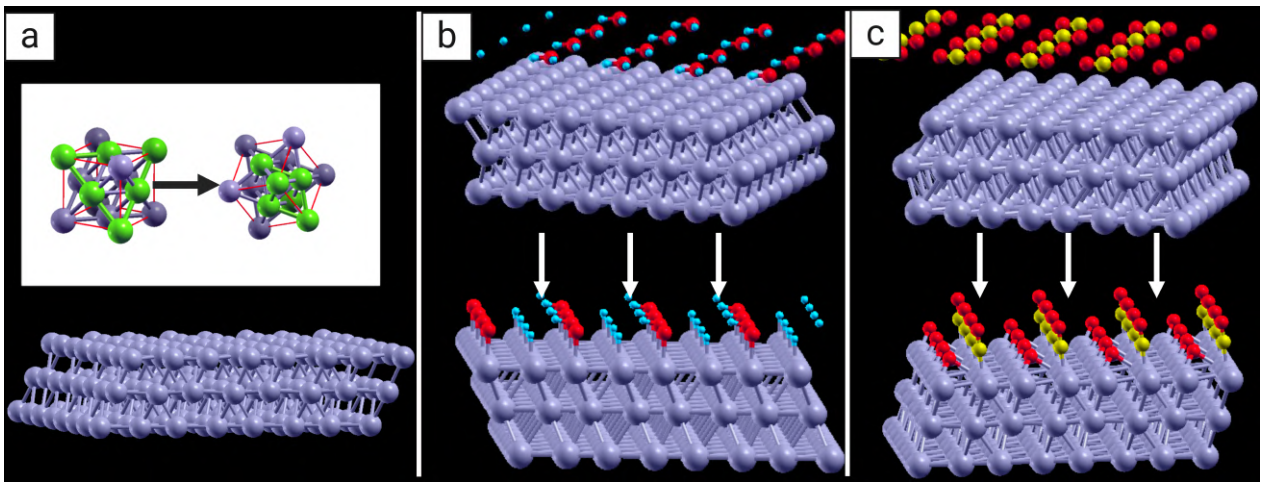

Figure 3.1: a) Crystal FCC bulk lattice, and hcp surface lattice, obtained by a surface reconstruction process(surface relaxation). b) Surface contamination by water molecules,(both physisorption-chemisorption). c) Surface contamination by CO2 molecules(both physisorption-chemisorption), system relaxation was performed, using DFT based, quantum espresso simulation.

Surface contamination is sometimes intentional, however, in most cases, contamination is undesirable, particularly in high-purity device fabrication, as contaminants may affect deposition rate, and purity of the device, thereby its properties.

Surface cleaning is a critical step in sample preparation, aimed to eliminate unwanted contaminants. Various techniques have been developed, for different types of cleaning such as gross cleaning, to eliminate large amounts of materials, done by stripping, abrasive cleaning using sandpaper or abrasive powder, chemical etching, electro-cleaning, fluxing, and deburring etc. Specific cleaning on the other hand, is employed for particular types of contaminants, such as particulates and hydrocarbons. In this process water or other polar solvents can be used to remove ionic contaminants, while non-polar solvents like chlorinated hydrocarbons to remove non-polar contaminants like oils. Cleaning processes can be performed at room temperature, however elevated temperatures are often employed to enhance solute in solvent solubility.
Cleaning processes can also be performed using gases or even plasma, in this technique, high-energy ions are generated through a Radio Frequency (RF) source, and attracted towards the targeted surface by means of a sheath potential. When accelerated ions/excited species bombard the surface, they transfer their kinetic energy to the surface, thereby augmenting the surface's overall energy(sheath potential). Consequently, this energy increase facilitates the rupture of bonds formed between the surface and contaminants(fig.3.2).

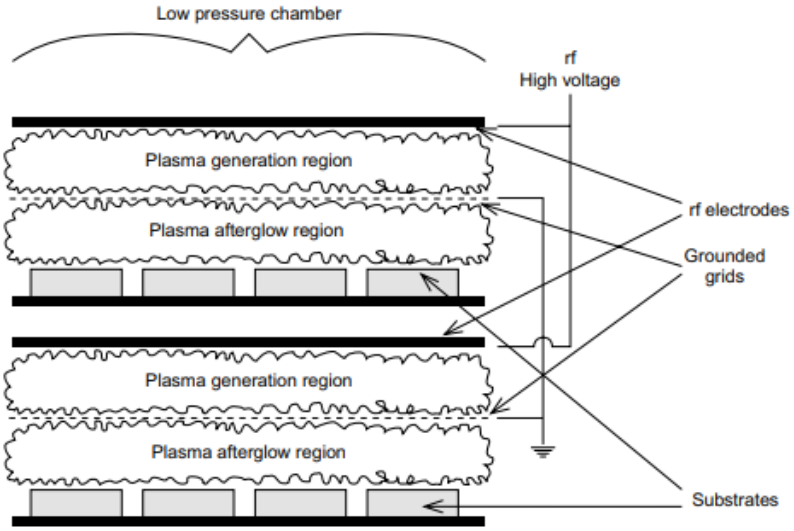

Figure 3.2: Plasma cleaning.

After the cleaning process, surfaces are usually rinsed with distilled water, particularly when soaps and detergents are used during cleaning, to eliminate any left-off residues. Then a drying process is usually performed to extract any moisture left after the washing process. For this purpose, different techniques can be used such as vapor drying, wiping, blown drying, or annealing.

Surface recontamination is very probable and can occur whenever the surface is exposed to the environment, subsequently in handling, transfer, or storage, thus, stringent protocols are enforced to lower as much as possible surface recontamination:

- In handling the sample, tools are used to avoid direct contact with the sample active surface region, and for that purpose gloves, tweezers, and other tools are used.
- For storage, plastic bags and polymers are avoided, especially if in direct contact with the sample active area, and instead glass containers are used.Storage can become more appropriate, by placing the sample in a vacuumed chamber(active storage).
- Since cleaning, storage and deposition chambers are usually physically separated, the sample must be transferred in between, which impose the risk of recontamination, therefore shortening the exposure time by swift transfer is very important to lower the contamination.

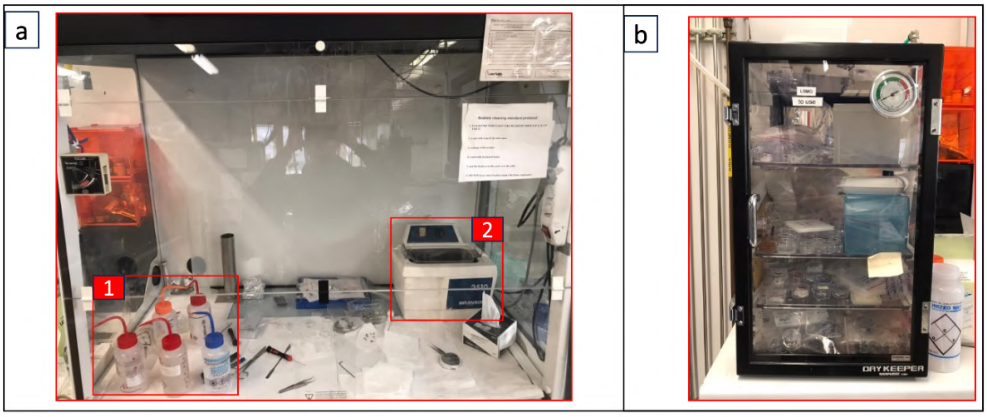

Figure 3.3: a) Laminar flow cabinet: 1) cleaning solvents(acetone-isopropanol), 2) Ultrasonic cleaner. b) active storage box.

3.2 Deposition techniques

3.2.1 Introduction

Most materials growth and deposition can be grouped into two approaches: top-down and bottom-up. The first involves methods that initiate from a highly pure single crystal bulk, previously obtained by single crystal growth techniques, such as Bridgman, Czochralski, PVT, solution..., then scale down in thickness by slicing process, cutting wafers as thin as 0.2 mm, then many top-down processes may be applied, such as PL,EBL...

On the other hand, bottom-up approach involves processes that starts at the atomic level, and scale up to a few nanometers/hundreds of nanometers. This approach is primarily utilized for thin film deposition, using various techniques like PVD, CVD, MBE, and inkjet printing. Although bottom-up techniques are atomically precise, and generate very small amounts of

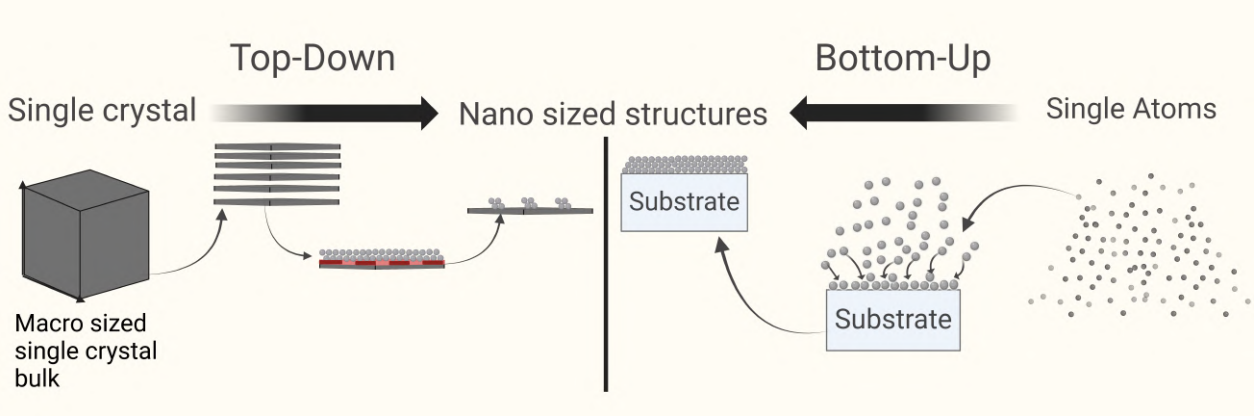

Figure 3.4: Top-down, bottom-up nano-fabrication steps.

waste, these techniques cannot be applied to large-scale deposition; This limits its applications in industrial mass production. Instead, top-down approaches such as PL are employed.

3.2.2 Physical vapor deposition

Physical vapor deposition is a widely used thin film deposition technique, initiated from a vapor generated by heating of powder or liquid using annealing or other means such as electron beam, the generated vapor of atoms/molecules are then transferred to the sample's surface where they condensate.

PVD consists on vapor transfer between two regions, thus lower vacuum is always desirable to lower scattering probability of vapor atoms/molecules by residual gases, however, low vacuum can also be used in this technique, based on the desired deposition rate, reactivity of the vapor with residual gas, and the tolerable impurities in the deposit film. At UHV materials follow a "line-of-sight" trajectory, with little/no collisions with molecules contained in the space between source and sample, which results a deposition rates(equ.3.1) between 1-10 nm per second in case of resistive annealing PVD.

$$\frac{dN}{dt} = 2\pi mkT \cdot C - \frac{1}{2}(p^* - p)sec^{-1} \tag{3.1}$$

Where dN = number of evaporating atoms per cm^2 of surface area.
C = constant that depends on the rotational degrees of freedom in the liquid and the vapor.
p* = vapor pressure of the material at temperature T.
p = pressure of the vapor above the surface.
k = Boltzmann's constant.
T = absolute temperature.
m = mass of the vaporized species.

While the flux distribution can have different shapes and dependencies. In case of low evaporation rates, with a small angular distribution, F have a simple cos dependence(equ.3.2):

$$\frac{dm}{dA} = \frac{E}{\pi r^2} cos\phi.cos\theta \tag{3.2}$$

where dm/dA is the mass per unit area.
E = the total mass evaporated.
r = the distance from the source to the substrate.
θ = the angle from the normal to the vaporizing surface.
ϕ = the angle from the source - substrate line.

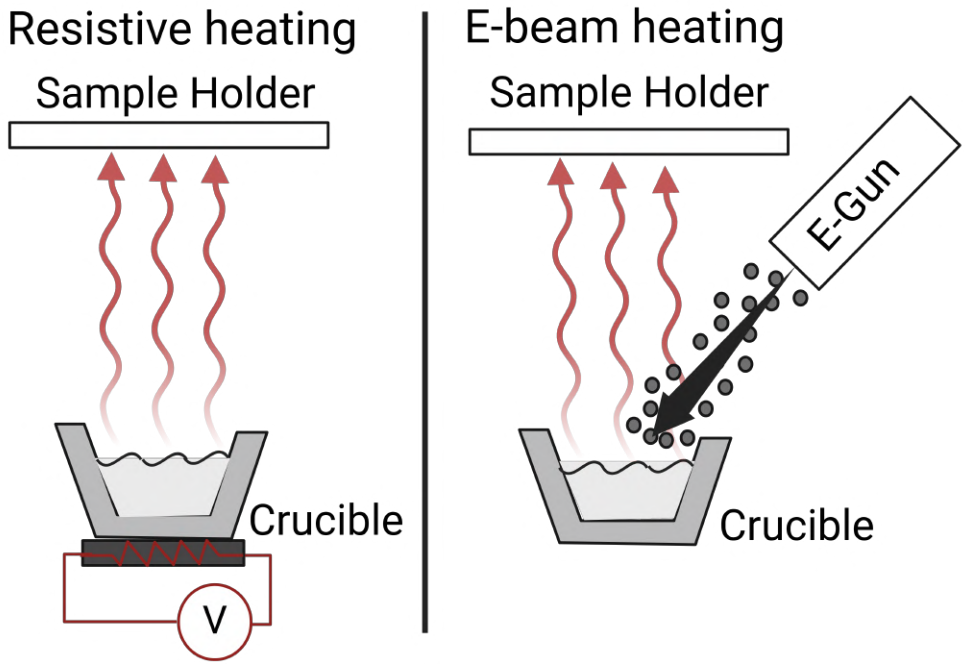

Figure 3.5: Resistive heating PVD, and E-beam PVD.

Materials are usually heated by direct resistive heating, for temperatures below 1500°C, while using other means such as electron beam, for desired temperatures above 1500°C. In resistive heating, high resistive materials such as Tungsten and Molybdenum can be used to achieve high heat energy by currents generated by voltages below 10 V. Resistive materials are usually coiled around a crucible containing the material to be vaporized to preserve the melt(fig.3.5).

High energy e-beam heating is typically used for refractory metals, ceramics, glasses. An e-beam is generated from an electron gun (thermionic emitting filament) operating at about (10–50) kW, the beam is then accelerated by an applied potential of (10–20) kV, and focused by electromagnetic focusing lenses into the target source, some of the transferred energy will be converted into heat that will cause the vaporization of the material. This method can achieve vaporization rates as high as (few Kg/h), thus causing a very high vertical/horizontal deposition rates.

3.2.3 Lithography

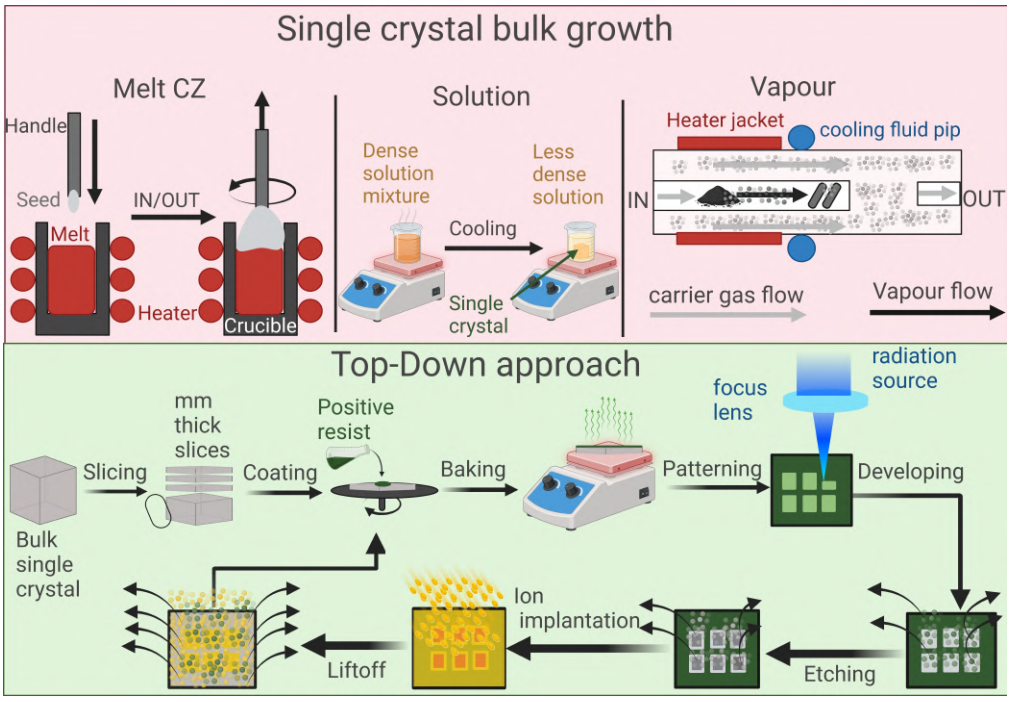

Figure 3.6: Top down approach, starting from a single crystal bulk growth, and different types, followed by a lithographic fabrication process.

Lithography is a patterning technique, performed by a light/particle source to pattern a functional polymer(photo/electro-sensitive) (resist), coated ontop of a sample's surface prior deposition, which allows an easy removal of unwanted (patterned/unpatterned) regions, after deposition, by lift-off processes.
Patterning is characterized by it's resolution, and depth of focus.

$$R = \frac{\lambda \cdot K_1}{NA} \tag{3.3}$$

$$NA = nsin\theta \tag{3.4}$$

λ = the wavelength of the used light.
NA = the numerical aperture of the projection optics.
n = reflective of the output medium.
θ = the maximum half light cone exciting the lens.
K_1 = a factor dependent on the technological process.

$$DoF = k_2 \frac{\lambda}{n(\sin\theta)^2} \tag{3.5}$$

K_2 = a factor dependent on the technological process, takes into account.

3.2.3.1 Types of lithography

Lithography patterning can be performed using:

- EM radiation, such as UV/EUV, with a setup almost identical to an OM. First, a generated light(UV-lamp etc.) is collimated by a collimator, shaped by a mask, then focused by a second lens (used to decrease the dice size), before is subjected to the area to be patterned. This technique can achieve resolutions up to 22 nm (EUV).

- E-beam (Gaussian beam electron lithography), can be used to perform both mask, or maskless patterning, with resolutions up to 45 nm. The setup, and operation mode are very similar to a SEM.(see.4.6).

3.2.3.2 Resists

Prior to patterning, the sample surface have to be coated by a (photo/electro sensitive) resist. During patterning, the resist properties are modified(chain-crosslink or chain-break), then after deposition, unwanted regions can be easily removed.
The energy needed for an efficient patterning, in relation to the thickness of the resist layer, can be estimated using (equ.3.6).

$$\frac{T_E(E)}{T_0} = \gamma ln\left(\frac{E_0}{E}\right) \tag{3.6}$$

T_E= the thickness that can be modified at a given energy E.
T_0= the thickness of the resist.
E_0= the energy needed to modify the resist layer of thickness T_0.
E= the applied energy.
Resists may be grouped into two categories:

- Positive resists are (Photo/electro-sensitive) polymers. Upon exposure, the polymer chains follow a bond-break, affecting the solubility of exposed regions (more soluble compared to the unexposed parts). During the liftoff process, only exposed regions are removed.

- Negative resists are (Photo/electro-sensitive) polymers. Upon exposure, the polymer follow chain bonding or cross-link, which affects the solubility of the exposed regions (less soluble compared to the unexposed parts). During the liftoff process, only unexposed regions are removed.

3.2.3.3 Electron Beam lithography

EBL is widely used in laboratories due to the lower patterning costs, wast production, compared to photolithography, even-if at the cost of a slight decrease in the patterning

resolution.
EBL can be performed in a maskelss manner, using a Gaussian energy distributed electron beam, generated by an electron gun, accelerated by an anode, focused by electromagnetic lenses, and patterned by an XY deflection lens, or by masking, using a wide homogeneous beam, obtained by an electromagnet collimator lens, then shaped by multiple deflection and masking processes, resulting a final shaped electron beam. This method offers higher patterning speed compared to GEBL. Even faster patterning can be achieved, using multiple-electron beam, with production that can reach few wafers per hour, compared to electron shaped lithography that can take about 10 hours to pattern a 300 mm wafer with 65 nm design rules [56].

Incoming electron beam can interact with the sample by following an elastic scattering, where

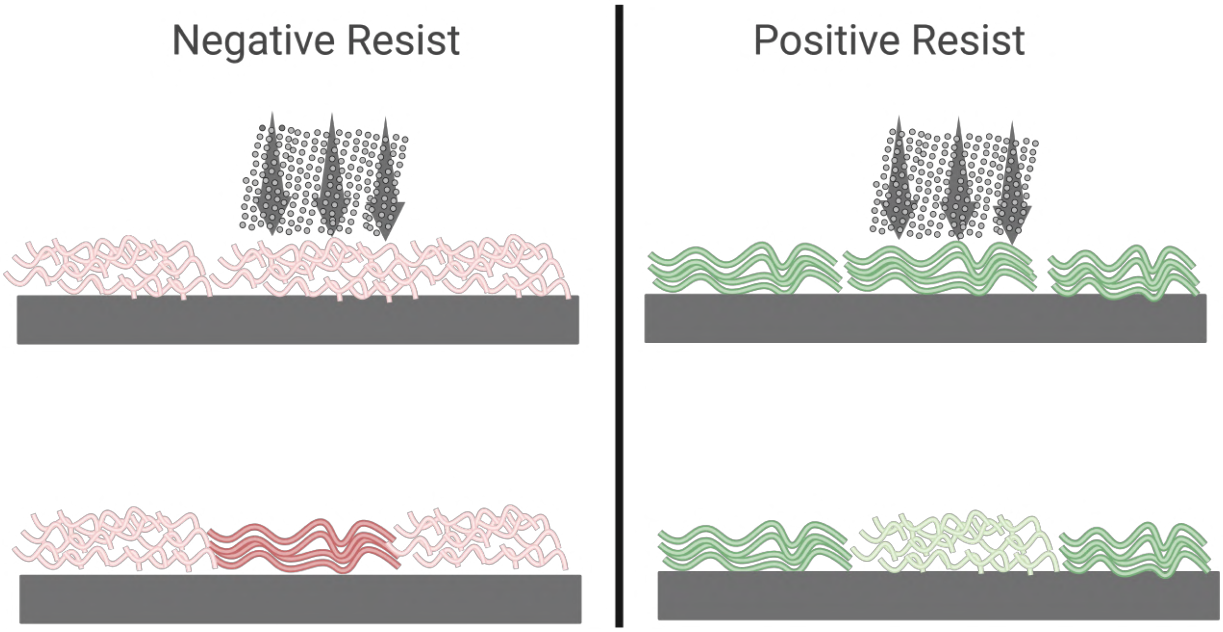

Figure 3.7: Negative resist cross-linking, and positive resists bond breaking of regions exposed by electron beam.

electron beam follow direction change, without any loss in it's initial energy(back-scattered by atomic nuclei), or can follow a direction change accompanied by energy exchange either with atomic nuclei, or electrons of the sample(inelastic scattering), leading to secondary electron emission-xray emission-Auger-phonons(see.4.6).
Many fundamental concepts imposes limitations on the EBL resolution, such as the electron bunching limit(Heisenberg uncertainty principle(equ.3.7).

$$\Delta x \Delta p \geq \hbar \tag{3.7}$$

Resolution is also affected by the resist sensitivity(equ.3.8), that determines the minimum amount of electrons N_{min} for the resist to be modified(equ.3.9)(about 100 e^-), this limits the smallest pixel width l_p(patterning resolution), capable of modifying the exposed resist(for S = $10\mu C/cm^2$,l_p=1.26×10^{-6}cm).

$$S = \frac{e \cdot N_e}{A}(C/cm^2) \tag{3.8}$$

$$N_{min} = \frac{S \cdot l_p^2}{e} \tag{3.9}$$

A third limitation is imposed by charge transport related phenomena: spatial charge,spherical and chromatic aberrations, generated by the electromagnetic lenses, and structures used to shape the beam.

3.3 Vacuum deposition chambers

3.3.1 Introduction

Many widely used device fabrication and characterization techniques such as molecular beam epitaxy(MBE), physical vapor deposition(PVD), and sputtering are carried out in vacuum. One fundamental reason is to minimize scattering probability of the transferred materials by residual gases, thus to achieve a 'line-of-sight' transfer. Equally important is to avoid contamination, and achieve a highly pure deposited layers [12].

Vacuum is evaluated based on particles density in the chamber, compared to the atmospheric density, and is represented in units of pressure (mbar-Torr).

Particles density can be estimated using the ideal gas relation:

$$PV = nRT \tag{3.10}$$

with P = the total pressure.
V = the total volume.
n = the number of moles of gases.
R = the gas constant.
T = the temperature.

Surfaces recontamination period is determined by the sticking coefficient, and the exposure dose. The sticking coefficient can be quantified as the ratio between the fraction of particles that stick on the surface, with respect to the total incoming number of particles. This parameter is totally dependent on both incoming particles and surface potential. In most cases, for most materials, surfaces have high energy, thus they tend to form bonds with contaminants to reduce their energy. The exposure dose is another important parameter, that affects the surface purity. It depends on both exposure period, and density of the exposure gas, this parameter is measured in Langmuir (L), where one Langmuir corresponds to an exposure of 10^{-6} Torr during one second.
Contamination can be controlled by controlling the dose, either by the exposure period or density of the exposure gas(equ.3.11). When an extremely pure fabrication is desired, the dose is lowered by lowering the density of the exposure gas, that can be done by operating under UHV $10^{-10} - 10^{-11}$ mbar.

$$xy[\mathrm{L}] = x \times 10^{-n}[\mathrm{Torr}] \cdot y \times 10^{n-6}[\mathrm{s}] \tag{3.11}$$

Where xy is the desired Langmuir, that can be obtained by varying the pressure term (gas density) and the exposure time term, relatively to each other so the final product will give the desired L.

3.3.2 Gas flows, and vacuum regimes

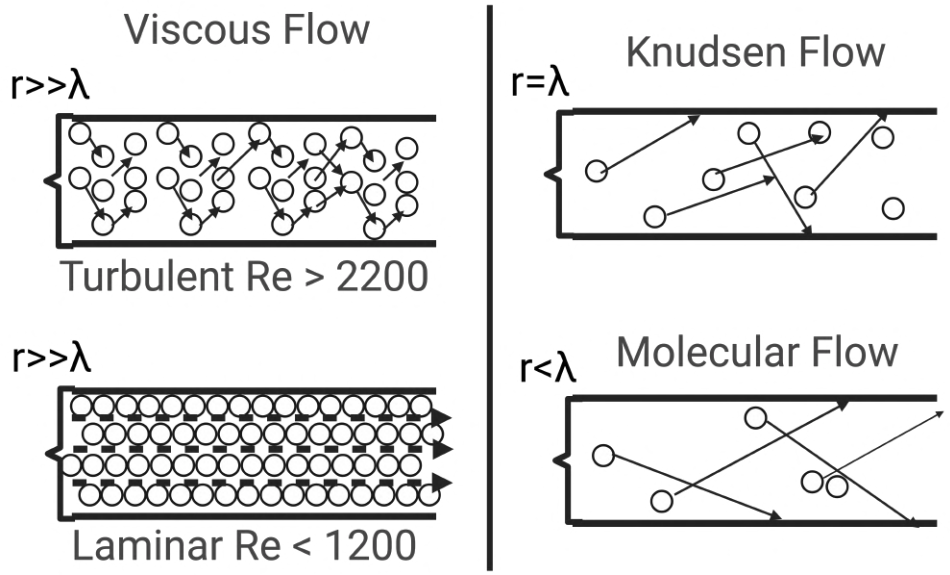

Figure 3.8: Different gas pumping flows: viscous flow when the molecular mean free path (λ) is much lower than the pip radius (r), Turbulent when Reynolds constant > 2200, and Laminar when Re< 1200. Knudsen flow, or transition flow, λ=r, and molecular flow when λ>r.

Vacuum can be low, starting from atmospheric levels, up to 1 mbar, high, reaching pressures up to 10^{-6} mbar, ultra-high, with pressures > 10^{-10} mbar, or extreme up to 10^{-12} mbar.

Chamber gas exhaustion, can follow three types of flows:

1. Viscous or continuum flow: is dominant at rough range(atmospheric pressure-100 mbar), when the molecule's mean free path is considerably shorter than the diameter of the pipe (λ < d), thus when intermolecular collisions are much probable that collision with the chambers walls.
   Viscous flow can be turbulent, if the moving medium follow a vortex motion, or laminar/layer flux, if moving in layers on top of each other. The type of the viscous flow can be determined by the dimensionless Reynolds constant $\mathcal{R}$e, a product of the pipe diameter, flow velocity, density and reciprocal value of the viscosity (internal friction) of the flowing gas. For $\mathcal{R}$e > 2200, the flow is turbulent, while for $\mathcal{R}$e < 2200, laminar flow is dominant.
   The maximum exhaustion intensity is determined by the ΔP_{crit}, any further increase in

the pressure difference $\Delta P > \Delta P_{crit}$, will not result any increase in the flow intensity, and the flow will be choked.

2. Knudsen flow: is a transition flow between viscous, and molecular flow, observed when the mean free path of gas particles $\lambda \approx$ pip diameter.

3. Molecular flow: is observed at high and untra-high vacuum regimes $> 10^{-5}$ mbar, when the gas molecule mean free path $\lambda >> d$, thus particles and molecules collisions with chamber walls becomes more probable, than to follow intermolecular collisions, leading to adsorption of free molecules on the inner walls of the chamber. For HV regimes, the (molecules adsorbed/free molecules) ratio is about 10^3, but can reach up to 10^9 at 10^{-11}mbar(in a sphere of a 1 L volume). The monolayer formation time τ in HV, is only a fraction of a second, while it can reach up to hours in UHV.

$$\Delta P_{crit} = P_1 \left[1\text{-} \left(\frac{P_2}{P_1} \right)_{crit} \right] \tag{3.12}$$

For air, 20°C, the critical value $(\frac{P_1}{P_2})_{crit}$=0.528.

3.3.3 Pumping speed

Pumps are evaluated by their effective pumping speed in direct connection, however, pumps are usually connected to the chamber through connections such as pipes, comprising valves, separators, cold traps, that lower the pumping speed, due to friction of gas molecules during pumping (equ.3.13).

$$\frac{1}{S_{eff}} = \frac{1}{S} + \frac{1}{C} \tag{3.13}$$

S_{eff} = the effective pumping speed.
S = the pumping speed.
C = the total conductance of the connection system.
C can take the form (equ.3.14), in a series connection, and (equ.3.15) for a parallel connection. It should be noted that C depends also on the type of flow, therefore on the operating pressure, and the shape of the pip(radius,length) (equ.3.16).
Total capacitance for multiple connections, attached in series:

$$\frac{1}{C} = \frac{1}{C_1} + \frac{1}{C_2} + ... + \frac{1}{C_n} \tag{3.14}$$

Total capacitance for multiple connections, attached in parallel:

$$C = C_1 + C_2 + ... + C_n \tag{3.15}$$

C_1,C_2,...,C_n = the capacitance of different connection components.
Capacitance dependence on pressure, pip size and cross section radius, in the viscous flow:

$$C_{vis} = 138 \cdot \frac{d^4}{l} \cdot \left(\frac{P1 + P2}{2} \right). \tag{3.16}$$

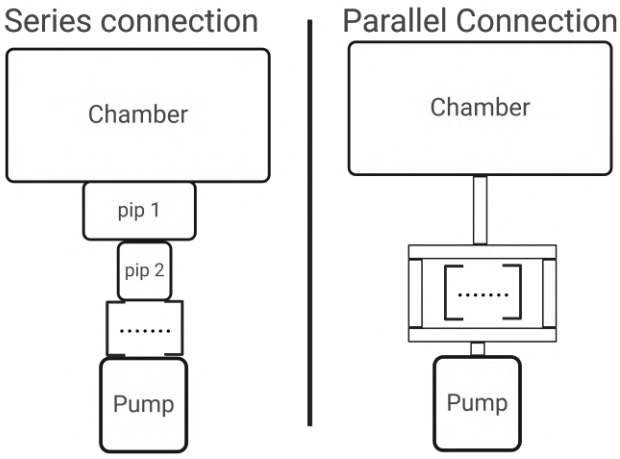

Figure 3.9: Vacuum connections in series, and parallel.

Capacitance dependence on the pressure, pip size, and cross section radius in the viscous flow:

$$C_{mol} = 3.81 \cdot \frac{d^3}{l} \cdot \left(\frac{T}{M}\right)^{\frac{1}{2}}. \tag{3.17}$$

d: pip diameter.
l: pip length.
(P1 + P2)/2: average pressure.
M:molecular mass.
T: temperature.

3.3.4 Pumps

To establish vacuum, pumps are used to exhaust gas molecules/atoms from the chamber to be vacuumed. Pumps are many, but can be grouped into two main categories:

- Compression pumps, in this type, gases are transferred to the atmosphere via multiple compression stages.
- Condensation pumps, in this type, gas molecules to be removed, condense on, or are bonded by other means (chemical bonds), to a surface,medium.

1. **Rotary vane pumps**
   Single stage rotary vane pump are based on an inner cylinder, that houses a rotor equipped with vanes. The rotor rotate as indicated in (fig.3.10), while vanes are sealed against the inner walls by centrifugal forces, but also springs to ensure vanes slide in the housing, oil also used as a lubricator, and as a sealing stage between the vanes and the housing. The gas enters through the intake port, and is pushed by compression through the exhaust valve. Rotary vane pumps are equipped with many other accessories, such as silencer, dirt filter, oil filter, Oil-level sight glass,Anti-suck-back valve...

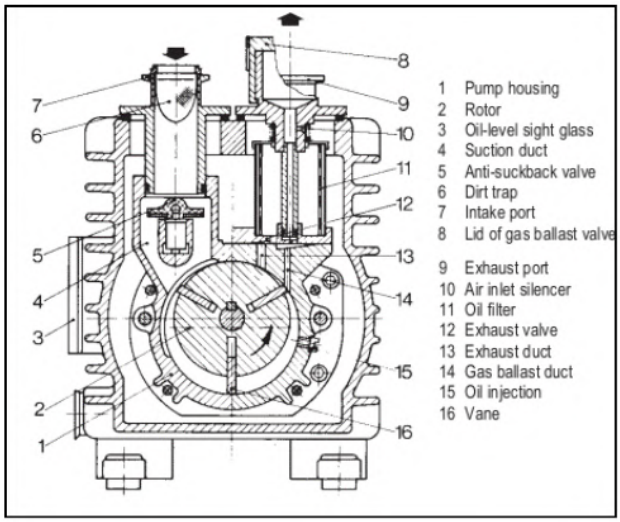

Figure 3.10: single-stage rotary vane pump cross section, with different accessories(taken from [12]).

Typical rotary vane pumps can achieve a pumping speed of 30-60 m^3/h, but can reach up to 585-1200 m^3/h (SOGEVAC model), for pressures $< 2 \times 10^{-2}$ mbar for single stage pumps,and 2.5×10^{-4} mbar for two stage rotary vane pumps.

2. **Sputter-ion pumps**
   Sputter-ion pumps pumping action takes place by sorption processes, initiated by

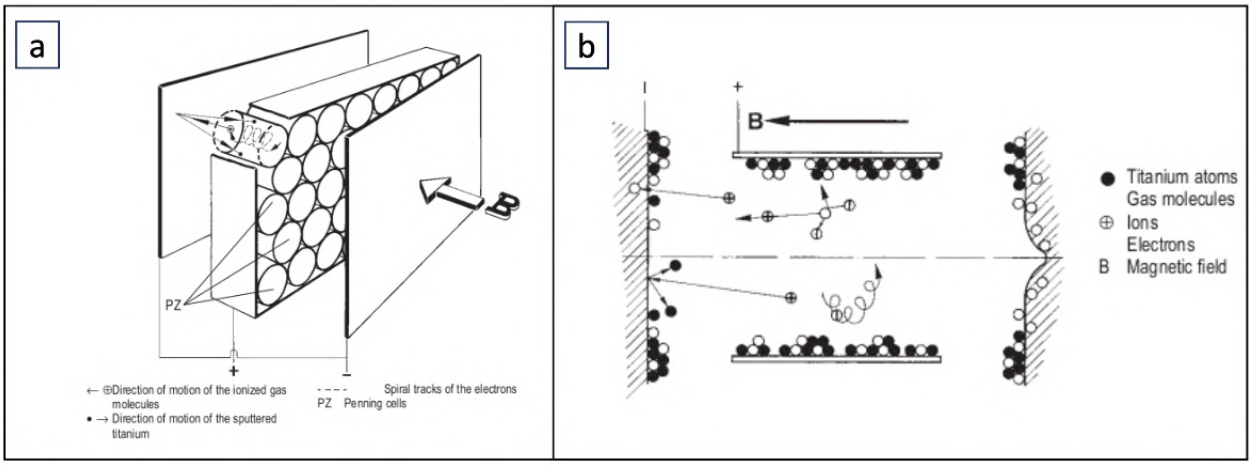

Figure 3.11: a)Sputter-ion pump accessories, and operating mechanism (taken from [12]).

ionized gas particles generated by a Penning discharge (cold cathode discharge). The pump is equipped with two cathodes(Ti), separated by a stack of cylindrical metals, perpendicular to the two plates, while a magnetic field B≈ 10^{-3} mT, generated by permanent magnet parallel to the cylinders(perpendicular to the cathode plates).

The cathode generate free electrons that follows a spiral trajectory as a consequence of the magnetic field B before hitting the anode cell, that causes the release of ions. Unaffected by the magnetic field, generated ions follows the fastest trajectory toward

the other cathode plate, where they collide. As a result, Ti atoms are ejected toward the other plate, while ions chemically bond to the cathode. The newly deposited Ti film act as a getter, and adsorb reactive gas particles(eg. oxygen, hydrogen, nitrogen)(fig.3.11).

The discharge current is dependent on electrons density n^-, ions density n_0, and the length of the total discharge path l:

$$i = n_0.n^-.\sigma.l \tag{3.18}$$

3. **Turbomolecular pump**:

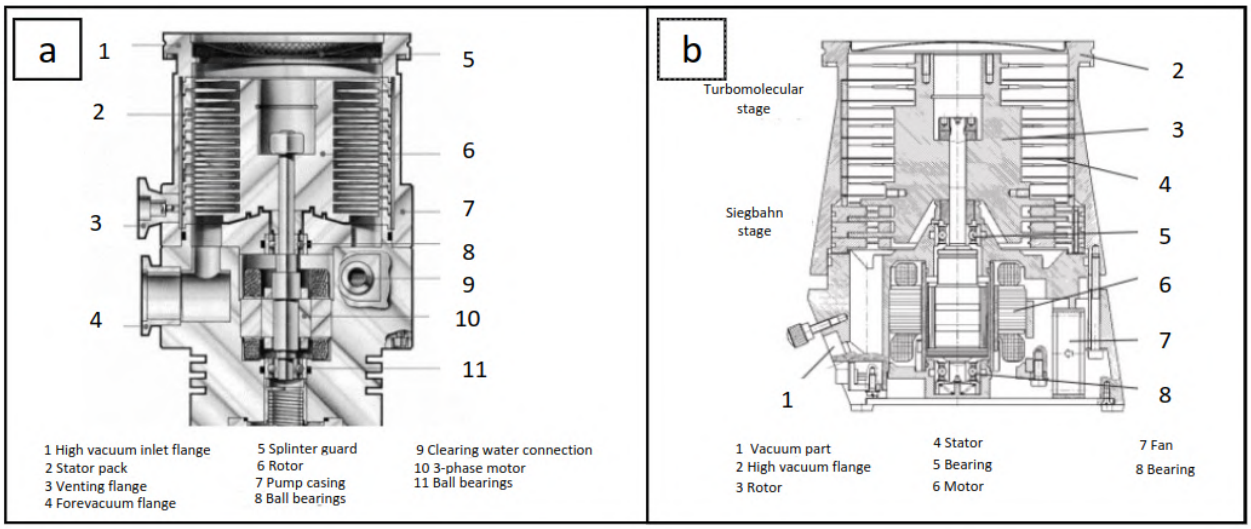

Figure 3.12: a) Turbomolecular pump cross sectional view, showing different components [12].

The pumping action in turbomolecular pumps is performed by impact with a constantly moving surfaces (rotor), leading to a multiple-stage compression, followed by exhaustion. Many parameters affect the pumping performance, such as rotor velocity. An optimal pumping is performed when the rotor speed is in the same order of magnitude of the average thermal velocity of gases in the chamber(equ.3.19).

$$\widetilde{c} = \sqrt{\frac{8.R.T}{\pi.M}} \tag{3.19}$$

The pumping speed is slightly affected by the molecular mass ($S \approx \widetilde{c} \approx \frac{1}{\sqrt{M}}$), however the compression k_0 varies exponentially with M ($k_0 \approx e^{\sqrt{M}} \rightarrow log(K_0) \approx \sqrt{M}$). Turbomolecular rotor speed can reach up to 36000 rpm, for large area pumps,and up to 72000 rpm for small pumps.
The first compression stage usually have a bigger radius that the following stages to ensure large annular inlet area.
The frequency of the rotators is set by a motor, that is monitored by an external frequency converter(solid state).

3.3.5 Sensors

Various methods can be used to estimate the operating pressure, and can be grouped in 2 categories:

- Gauges that measures the pressure by a direct monitoring of forces generated by collision processes, that is directly dependent on the density and temperature of the gas, and independent on the gas type.
- Gauges that estimates pressure, by measuring pressure related properties such as thermal conductivity, electrical conductance etc., these parameters usually depend on the gas type.

Vacuum gauges with gas-dependent pressure reading like thermal conductivity gauge(Pirani gauge), are employed to estimate gas pressure, by measuring thermal conductivity of the gas(fig.3.13). This method consist on measuring heat energy loss of a heated filament, due to energy exchange with gas molecules in the chamber, pressure can then be related to the heat conduction by(equ.3.20), this is only valid in the indicated range, where the thermal conductivity do depend on the pressure (fig.3.13).
Ionization vacuum gauges are the most used instruments to measure gas pressure at HV and UHV, even if at the reading may have low accuracy (up to 50%), especially when there's a sudden increase of pressure, but these devices are the cheapest of all HV-UHV gauges, and are easy to operate. The method of work is similar to the ion pump (IP), a discharge current is generated between an anode and a cathode, that are biased by 2 kV, the free electrons then follow a spiral trajectory due to an external magnetic field generated by a permanent magnet in the direction of the cathode. Electrons then hits gas particles, that gets ionized, that are then collected by (anode/cathode), generating a pressure dependent discharge current, that can be read on the meter(fig.3.13).

$$P_{el} = C_1 \cdot \lambda_{gas}(T(t) - T_a) + C_2 \cdot \lambda_{fil}(T(t)\text{-}T_a) + A_{fil} \cdot \epsilon\sigma(T(t)^4 - T_a^4) + c_{fil} \cdot m_{fil} \left(\frac{\mathrm{d}T}{\mathrm{d}t}\right). \tag{3.20}$$

where c_{fil} and ϵ are specific heat and emissivity of the sensor wire (material properties), A_{fil} and m_{fil} are surface area and mass of the sensor wire, and C_1 and C_2 are constants determined for each sensor in calibration.

3.3.6 Leaks and detection

In a vacuumed chamber, pumping is constantly performed to maintain vacuum. Many leakage sources can affect the vacuum, some which are unavoidable (Permeation), imposing limitations on the highest achievable pressure (equ.3.21).

$$P_u = \frac{Q_G}{S_{eff}} \tag{3.21}$$

These sources can be grouped into:

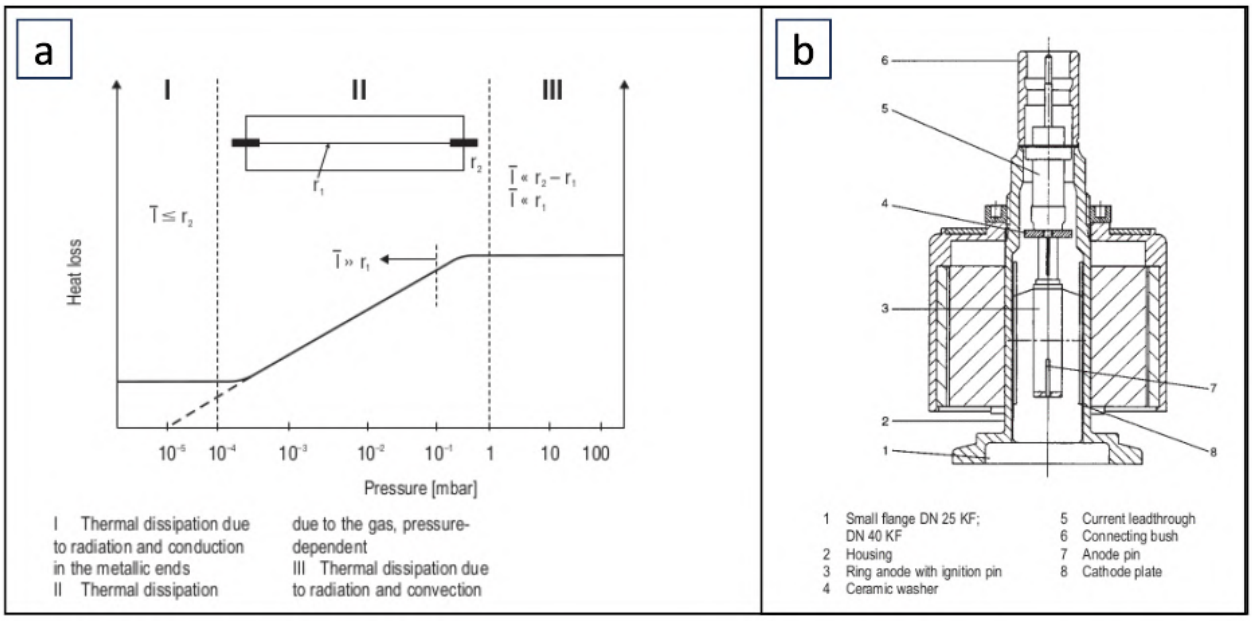

Figure 3.13: a) Thermal conductivity gauge(Pirani) showing the operating pressure range, where thermal conductivity is dependent on the pressure.b) Ionization gauge (taken from [12]).

- Leaks in detachable connections(flanges, connections).
- Leaks in permanent connections(solder, welding, glue).
- Leaks due to porosity(due to mechanical deformation, or thermal processing of some cast components).
- Thermal leaks(appears at a extreme temperature loading(hot/cold)).
- indirect leaks(leakage from vacuum systems, or furnace).
- permeation(rubber hose, and elastometer seals).

Vacuum sealing is assessed by it's leakage rate Q_L(equ.3.22), if $Q_L < 10^{-6}$ mbar ls^{-1}, the equipment is considered very tight, whereas if $> 10^{-4}$ mbar ls^{-1}, the equipment is said to be leaky.

$$Q_L = V \cdot \left(\frac{\Delta P}{\Delta t}\right) = \left(\frac{R.T}{M}\right)\frac{\Delta m}{\Delta t}. \tag{3.22}$$

3.3.7 Deposition system

1) Intro chamber, containing a heater to perform a low pressure PVD, hole connected to oxygen hose, used for oxidation processes.
2) Mask chamber, containing a mask holder (H).
3) PVD chamber, housing 4 crucible (Al-C60-Gaq3-6T).
4) Intermediate chamber, used to separate the EBPVD chamber from the rest of the system.

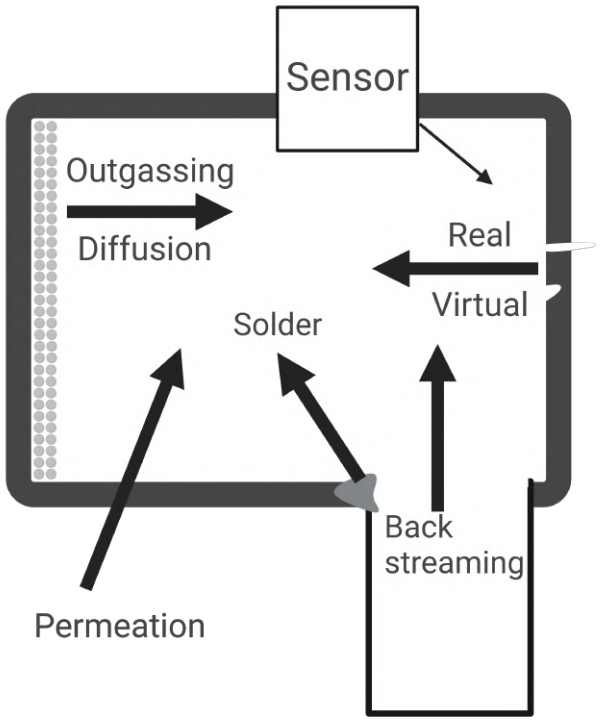

Figure 3.14: Different types of leakages in a vacuumed system.

5) EBVD chamber, housing a Cobalt wire, to be used for EBPVD, and an electron gun.
TB = Turbomolecular pump.
IB = Ion-beam pump.
W = Isolation wall.
H = Mask holder.
C = Crucibles, containing different materials to be used for PVD.

The deposition structure, illustrated in (fig.3.3.7), comprises four separate chambers, each serving a distinct purpose. These chambers are interconnected by a transfer line, accommodated with walls to isolate the chambers from each other, and prevent cross-contamination in case of a leakage.

The intro chamber, designated for sample insertion, and is the only chamber in direct contact with the external atmosphere, this chamber is accommodated with an oxygen source, used in oxidation processes, and a heater for PVD.

The central chamber represent the masking chamber, equipped with a stand that houses masks. This chamber is utilized for placing, changing, or removing masks in case of a shadow masking deposition, also serves as an intermediate chamber, linking other chambers to each other.

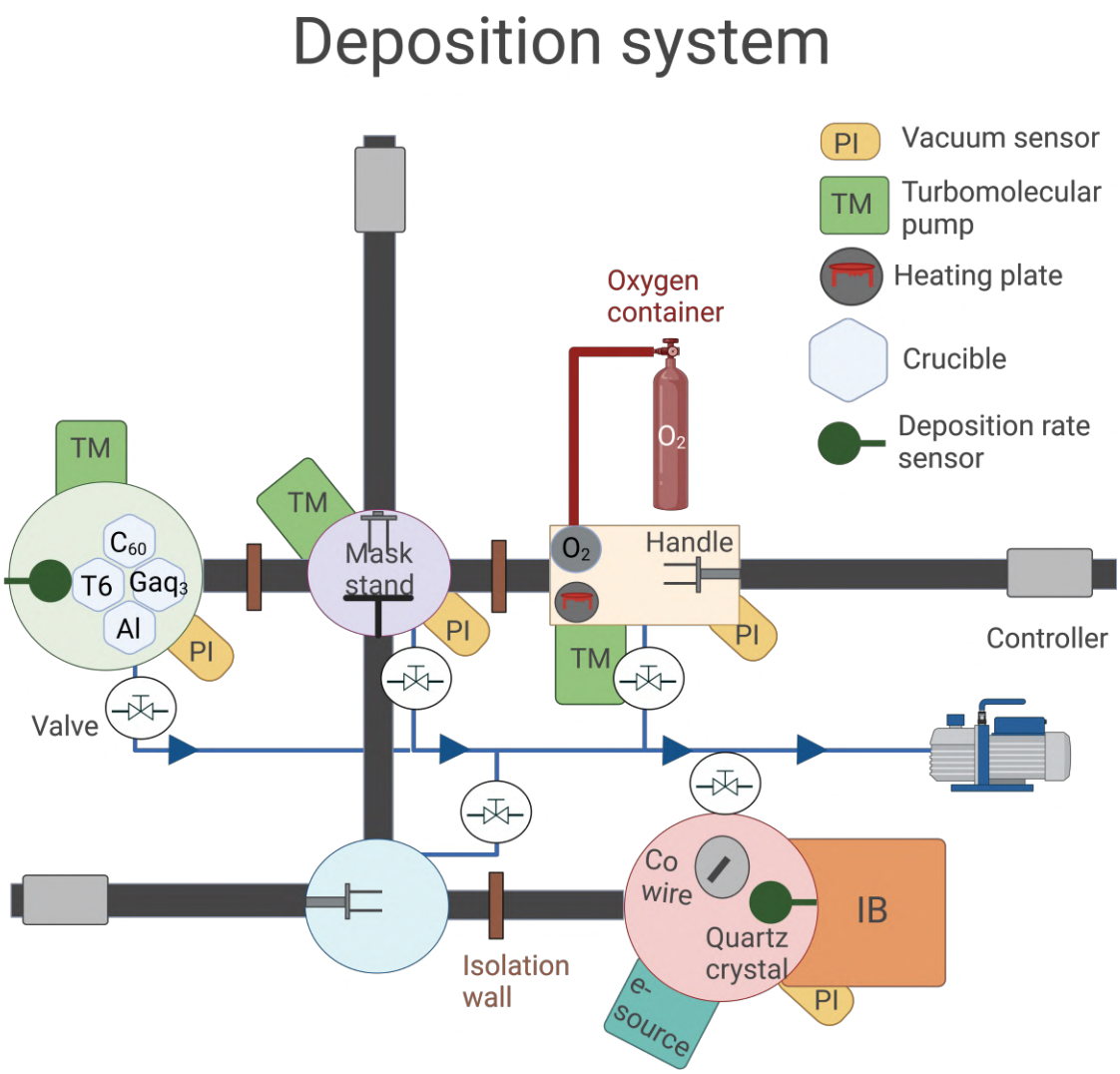

Figure 3.15: Deposition system.

Followed is the PVD chamber, houses four crucibles containing different materials, namely Al, C60, 6T, and Gaq3, and used for PVD, while the fourth chamber is dedicated for Cobalt EBPVD.

For vacuum attainment, each chamber is connected to both a roughing pump and a turbomolecular pump, allowing vacuum levels to reach up to 10^{-9} Torr. Except, the EBPVD chamber, where an ion beam pump (IB) is used to achieve higher vacuum levels, up to 10^{-11} Torr.

The transfer of samples between chambers is facilitated by a magnetic handle, ensuring a controlled and contamination-free transition.

Chapter 4

Characterization techniques

4.1 Electronic instruments

Electronic devices are essential in all laboratories, and used for many purposes such as monitoring, and characterization. Electronic instruments can be evaluated based on many parameters, such as:

- Accuracy: evaluated in terms of the instrument ability to generate an output signal, exactly as the set input parameters. Ideally, the output should match the input precisely, but real instruments typically introduce errors; It can be said that the lower the difference between input and output, the more accurate and reliable the instrument is.
- Stability: described by any short-term or long-term deviation of the source output signal from its set-point over a specified period, and within a defined temperature range.
- Resolution: represents the smallest value an instrument can generate. Highly sophisticated SMU's can reach a resolution down to μV/fA.
- Range: represents the difference between the highest and lowest applicable output by the instrument. Some instruments can cover ranges up to $\pm$30 V/$\pm$200 mA.
- Output resistance: refers to the internal resistance of the source within a given sub-range. In the case of a voltage source, the resistances are connected in series, whereas for current source, they are connected in parallel, the internal resistance is determined by the (series/parallel) configured resistances to achieve a given sub-range.
- Output noise: is generated by the source unit during the production of the output signal. This noise is specific, and vary with the operating sub-range.
- Common mode rejection ratio: represents the ability of the SMU to attenuate any signal generated by the device under test (DUT) within a specified frequency range, typically below 60 Hz. For instance, if a DUT exhibits high signal noise below 50 Hz, this mode can be employed to reduce these unwanted noises.
- Response time: is the duration required for the SMU to regain stability within 0.1% of

the final input after a step change in the input amplitude.

- Source guard: is a shield that surrounds the source circuit and is connected to the Lo lead. This shield plays a crucial role in reducing common-mode noises emanating from the source.

Characterization electronics can be grouped into many categories, such as:

- Source measurement units (SMU) are instruments capable of sourcing and measuring continuous or pulsed, current or voltage simultaneously, these instruments are used for low noise, 2-4 point probe characterizations. These devices offers high resolution(few μV, at $\pm$1.1 V range, for a voltage source/few fA over $\pm$1 nA range), and can operate over a wide range (I-V)(voltage source $\pm$1-110 V/ current source $\pm$ 1 nA-100 mA), and can sense currents/voltages, with accuracy up to ($\pm$ 0.0028 % for voltages, and $\pm$ 0.3 % for current measurement) [57].

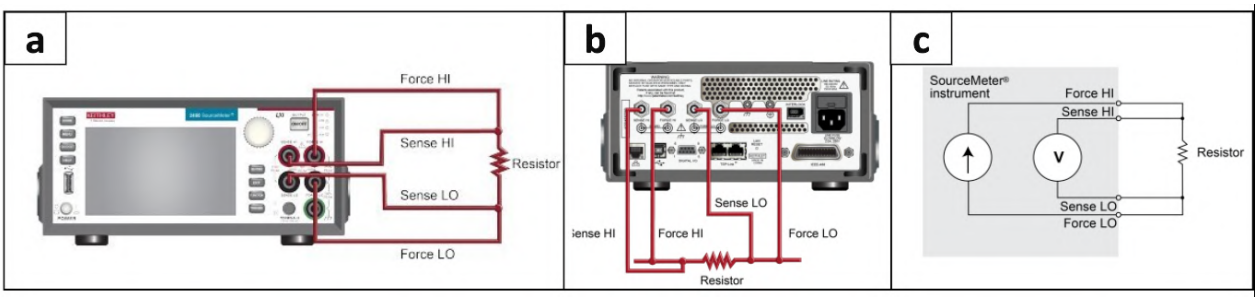

Figure 4.1: Keithley 2450, a) front and b) back connection for a 4 point prob measurement. c) Illustrative scheme(taken from [13]).

Keithley 236 SMU table of specifications [58]:

Source V			Measure V	
Range	step size	accuracy (1 year 18-25°C)	resolution	accuracy(1 year 18-25°C)
$\pm$1.1 V[2]	100 μV	$\pm$(0.033% + 650 μV)	100 μV	$\pm$(0.028% + 300 μV)
$\pm$110 V	10 mV	$\pm$(0.033% + 24 mV)	$\pm$110 V	$\pm$(0.033% + 24 mV)
Source I			Measure I	
$\pm$ 1.0 nA	100 fA	$\pm$(0.3 %+ 450 fA)	100 fA	$\pm$(0.3 % + 100 fA)[2]
$\pm$100 mA	10 μA	$\pm$(0.1 %+ 20 μA)	10 μA	$\pm$(0.1 % + 6 μA)

Table 4.1: Keithley 236 voltage/current, source/measure of the lowest range, and the highest range.

Keithley SMU 2450 table of specifications [59]:

Source V				Measure V		
Range	resolution	accuracy (1 year 18-25°C)	Noise (RMS) < 10Hz	resolution	input resistance	accuracy(1 year 18-25°C)
20 mV	500 nV	0.1%+200μV	1μV	10 nV	>10GΩ	0.1%+150μV
200 V	5 mV	0.15%+24 mV	1 mV	100 μV	>10GΩ	0.15%+ 10mV
Source I				Measure I		
10 nA	500 fA	0.1%+100pA	500fA	10 fA	<100μV	0.1%+50 pA
1 A	50μA	0.067%+900μA	3μA	1μA	<100 μV	0.03%+500μA

Table 4.2: Keithley 2450 voltage/current, source/measure of the lowest range, and the highest range.

Frequency resolution	1 μHz
Amplitude range	10 mV to 10 V 50Ω 20 mV to 20 V in Hi-Z
Amplitude accuracy	$\pm$1% of setting $\pm$1 mV
DC Offset range	$\pm$5 V in 50 Ω $\pm$10 V in Hi-Z
External lock range	10 MHz

Table 4.3: Keithley 3390 table of specifications.

- Function generators are designed to generate a variety of (current/voltage) waveforms in DC and AC mode, over a wide frequency and amplitude ranges, between μHz up to 50 MHz, and 10 mV up to 20 V, with resolution up to 16-bits, and a sampling rate up to 125 MSample/second. In can also be set to perform a linear, or logarithmic frequency sweep. These instruments are used to perform high resolution synchronous AC-IV characterization, used for ToF, impedance analysis...
  Keithley 3390 table of specifications:
- An oscilloscope, is used for capturing and representing analog signals in a digital format, usually during IV characterization, in a synchronized manner, allowing real time analysis of the wave dynamics, that can be stored, and displayed on a digital screen. Various parameters play a crucial role in the performance of an oscilloscope, such as sampling rate, bandwidth, update rate, and memory depth.

  Sampling rate represent number of samples per second, higher sampling rate is always desirable to achieve a more smooth representation of the acquired signal. To avoid crossover(aliasing) between frequencies, sampling rate must always be equal or bigger than the signal bandwidth(Nyquist-Shannon sampling theorem).
  Frequency bandwidth is another important parameter, set by the band-pass filter, used for signal selection. Ideally, the selected window must be a square, however, filters have a response time, and the selected bandwidth will not be a perfect square, the selection is evaluated based on the rise and fall time, observed at the edges of the selected bandwidth. Bandwidth, and rise time determines the highest frequency range,

that is possible to sense. Highly sophisticated instruments can reach up to 100 GHz of bandwidth.

$$F_{BW} = \frac{0.45}{Risetime} \tag{4.1}$$

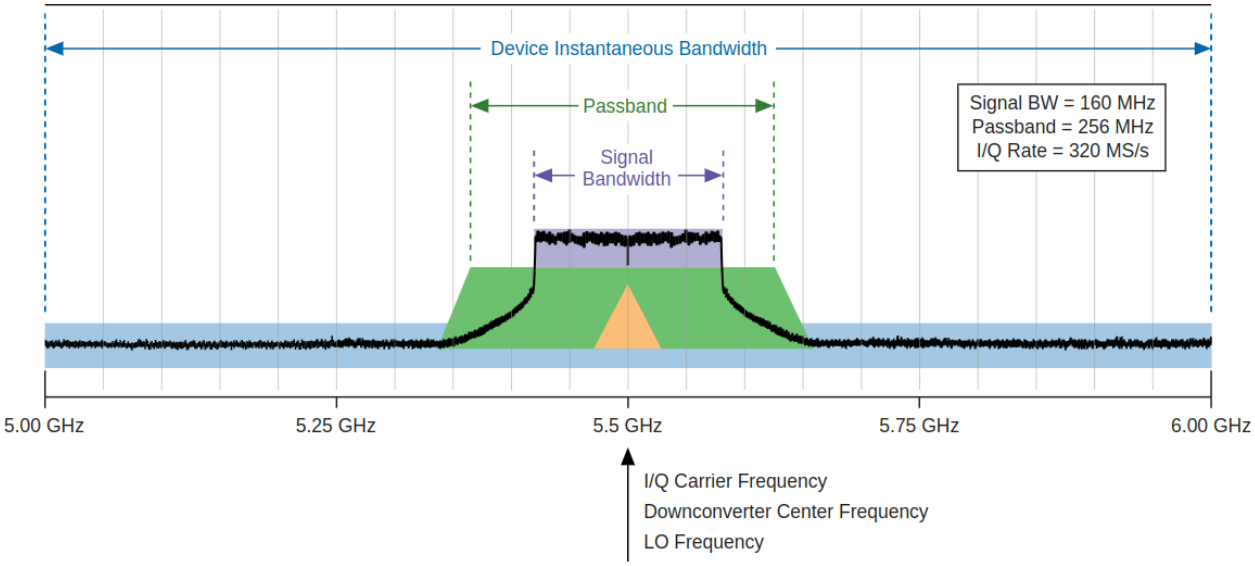

Figure 4.2: Acquisition of a 160 MHz signal bandwidth, at a 320 Msample/sec sampling rate, exactly double the bandwidth(Nyquist-shannon sampling theorem), within a passband of 256 MHz.

The update rate of an oscilloscope is important for displaying waveform changes smoothly, and ensuring real-time representation of signals. A higher update rate enables more accurate visualization of the signal's dynamics.

Memory depth is another significant factor influencing the accuracy of measured signals. It determines the amount of stored signal data in the oscilloscope's built-in memory. A larger memory depth allows more data points to be stored, providing a better representation of the signal; however, it also impacts the sampling rate, as a larger memory depth may result in a slower sampling rate.

4.2 Oxford continuous flow cryostat

Cryostats are structures employed in laboratories to maintain extremely low temperatures for extended periods, facilitating temperature-dependent characterizations of samples under investigation.

Various types of cryostats exist such as closed-cycle, continuous flow, bath, and multistage cryostats. Despite their differences, these instruments shares a common mode of operation, involving heat exchange, by a thermal contact with a cryogenic liquid such as nitrogen or helium.

The continuous flow cryostats structure is comprised of multiple layers. The innermost layer (referred to as sample space) houses the sample. A capillary tube is positioned between the sample space and a radiation shield to transfer the cryogenics and cool the sample space, through a heat exchanger. Then an outer region is kept under HV, to insulate the inner structure from the outer atmosphere, and prevent any heat exchange with the surrounding.
Continuous flow cryostats operate by continuously supplying cryogenics through a bayonet

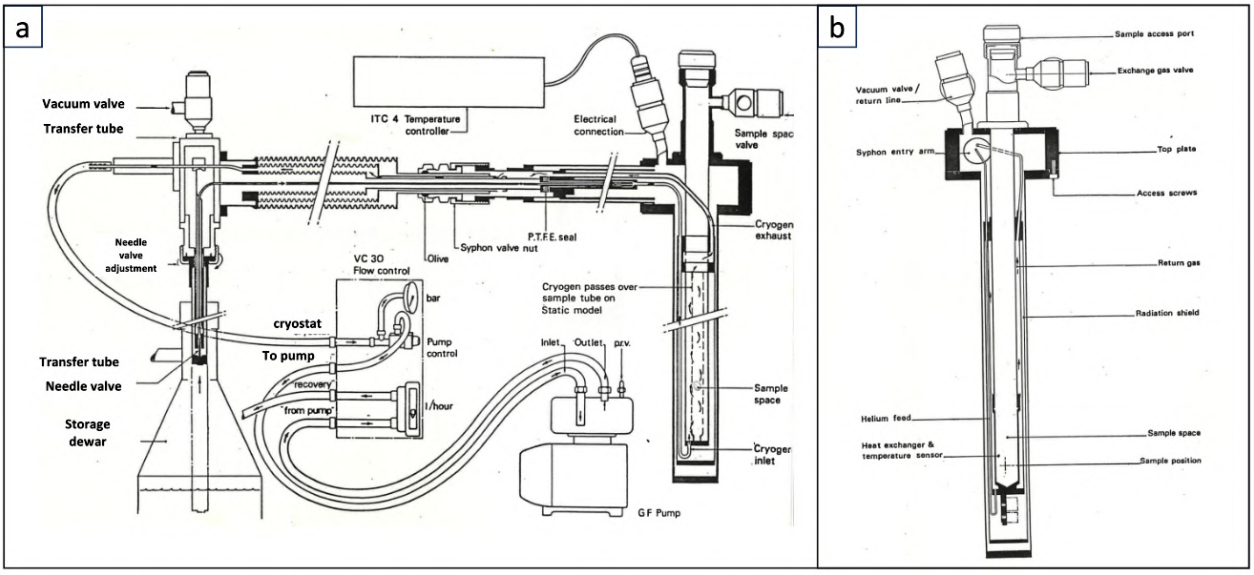

Figure 4.3: a) Continuous flow cryostat connection. b) Cryostat.

connection, linked to the Dewar by a transfer line, allowing the transfer of the cryogenic liquid flow, that is generated and monitored by a roughing pump.

Before operation, the sample space is evacuated and filled with the exchange gas, usually of the same type of the cryogenic liquid, to establish a good thermal contact between the capillary tube, and the sample space environment.

4.3 Probe station

A probe station is a structure that incorporates all essential devices/tools for performing an electrical characterization, for small devices such as microelectronics.

To connect the device under test (DUT), micro-needles made of tungsten or gold are utilized, and can be controlled by piezoelectric micro-manipulators, enabling 4-dimensional movement, through X,Y,Z and inclination q_z, with a range of 20x20 mm^2 in the (X,Y) plane, 40° in the z direction, and ±180° in the q_z. Typically, a microscope and light source are mounted on the bench, and the entire sample space is covered by a Faraday cage to prevent any electromagnetic interactions with the DUT.

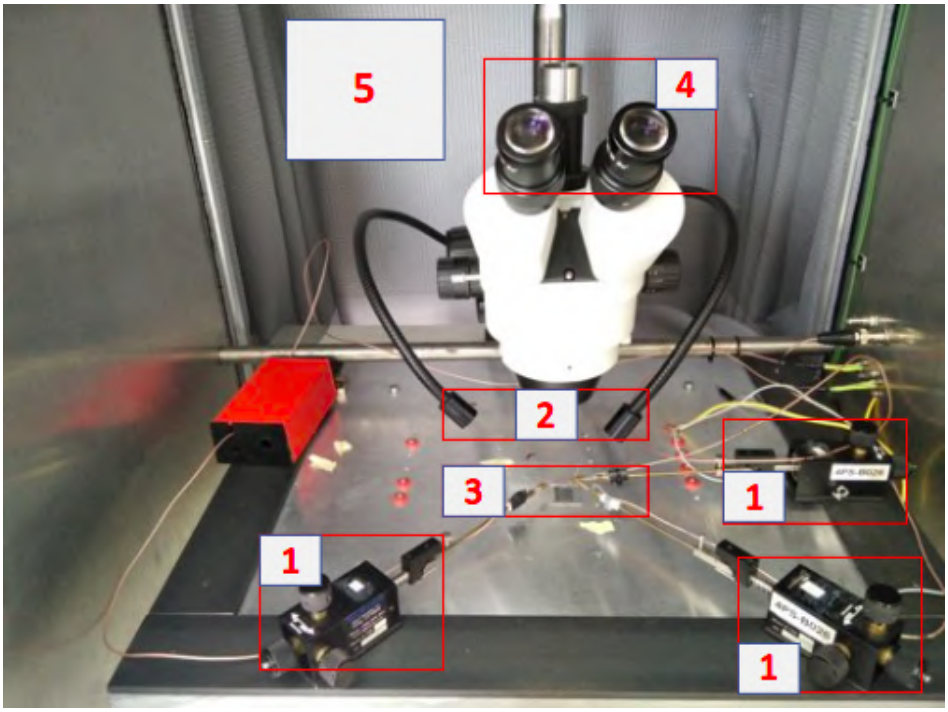

Figure 4.4: Probe-station: 1) Micro-manipulators, 2) Light source, 3) Gold needles attached to the micro-manipulators and connected to the DUT, 4) Microscope, 5) Faraday Cage(taken at UNIBO Lab).

4.4 Electromagnets

Electromagnets are instruments used to generate linear magnetic fields, by an electrical current. A typical electromagnet can be considered as a solenoid, consisting on a metallic wire, uniformly coiled in a cylindrical manner, with radius bigger than length. The circular motion of the electrons inside the coil, generate a linear magnetic field normal to the plane of the electrons motion(equ.2.1). To achieve higher magnetic fields, the metallic wire is coiled

around an FM, resulting an amplification in the induced magnetic field B, due to the intrinsic magnetization of the FM that adds up to the initial generated field H (equ.4.2).

$$B = \mu_0 \mu_r n I = \mu_r B_0 \tag{4.2}$$

Shortening the separating distance between the poles, can increase in the highest achievable field, and result an almost collinear generated flux. Two configurations are possible, either by bending the FM, to have face facing poles(o-ring), or by using two facing solenoids, biased with an opposing electric fields, resulting an opposed poles(fig.4.5).

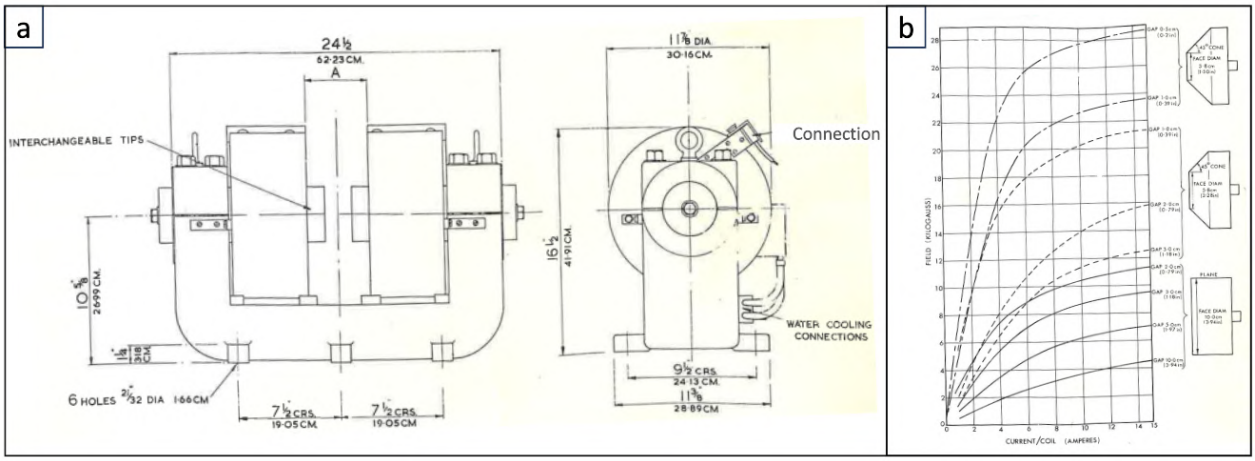

Figure 4.5: a) Electromagnet scheme, and b) saturation magnetic field for different poles shapes.

The generated field, can depend directly on the focus of the generated flux, therefore is directly dependent on the shape of the poles(conic shaped pole, will allow achieving higher fields, compared to a plane shaped pole)(fig.4.5).

Typical electromagnets can produce fields around 2 T, but can reach up to 10 T, albeit at the cost of substantial current, approximately 30 kA, and significant energy dissipation (around 5 MW of heat energy), due to the resistivity of the wire, that impose limit in the highest achievable field. These instrument are constantly cooled down by water or air, to avoid the wire melt down. To treat these limitations, superconductor materials can be used, due to their property of having an almost 0 resistivity below certain temperature and magnetic field, thus enabling the attainment of higher magnetic fields, with a much smaller structure size, and nearly zero energy dissipation.

4.5 Characterization system

The characterization system consists on an Oxford cryostat, attached to a stand, between electromagnet poles. The samples are mounted on the sample holder (fig.4.7), in an horizontal or vertical configuration, leading to in-plane control of the magnetic field direction(between x and y), or in-plane/out of plane control(xy/z).

Once the sample holder is placed in the cryostat, both sample space and the outer space are pumped using a roughing rotary, oil sealed vane pump.
The sample holder top connection, and all the electronic instruments used in the characterizations, are connected to a keithley matrix, that acts as intermediate stage used to control connections between the DUT and the characterization instruments(fig.4.6).
All electronic instruments control and data acquisition are monitored via an interface with labview programs.

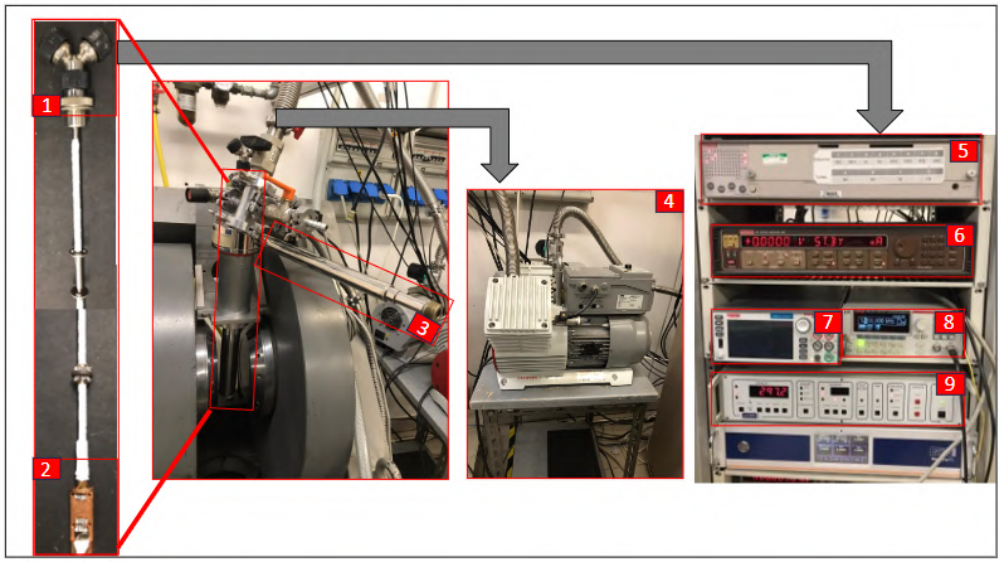

Figure 4.6: 1) sample holder system connection, 2) sample space(vertical/horizontal), 3) cryostat cryogenic connection tube, 4) pump, 5) connection matrix, 6) Keithley 236 SMU, 7) Keithley 2450 SMU, 8) Keithley 3390 wave function generator, 9) Oxford temperature control.

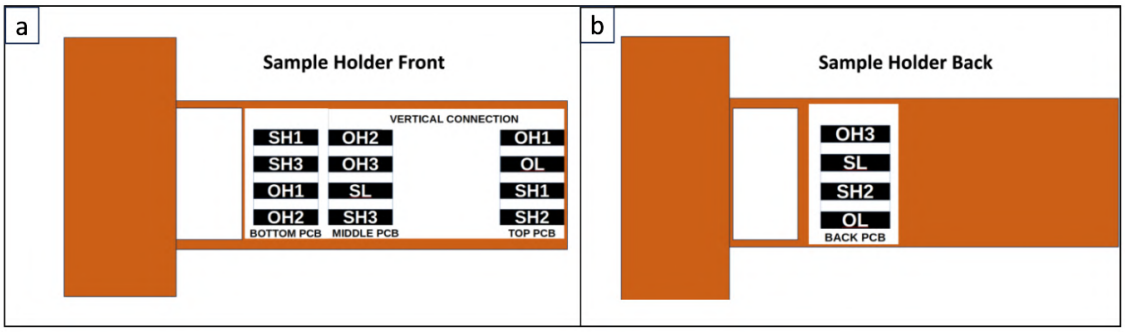

Figure 4.7: Scheme showing the sample holder front and back connection pads, the sample may be mounted vertically, or horizontally, to allow different orientations of the sample with respect to the applied magnetic field.

4.6 Scanning electron microscopy

4.6.1 Fundamentals

Scanning electron microscopy is a widely used technique for surface imaging and chemical analysis [60]. The technique consists on measuring different emissions followed by an e-beam interaction with a sample's surface. An incoming electron beam can either be elastically scattered by the sample surface, (direction change, no energy loss), or inelastically scattered(direction change, accompanied with energy loss), due to energy exchange with the sample's constituents. The exchanged energy is then released in a form of heat, radiation, or matter, that can be sensed/detected, and used for surface analysis. Scanning electron microscopes, offers an e-beam, with a controllable energy/spot size, over a wide range (0.1-30 keV)/(1-100 nm), used to control the e-beam penetration depth, thus, the depth/spatial resolution of the resulting images.

Since electrons can be considered as waves, Abbe's resolution/wavelength equation for OM, can be used also for an e-beam:

$$d = 0.612 \cdot \frac{\lambda}{n \cdot sina} \tag{4.3}$$

Where d= resolution.
λ= the wavelength of the source=$\frac{h}{p}$.
n= index of refraction of medium between point source and lens, relative to free space.

4.6.2 Interactions

The incoming beam penetration and interaction region with the sample's surface depends on both the incoming beam energy, and the sample's chemical composition (fig.4.9).

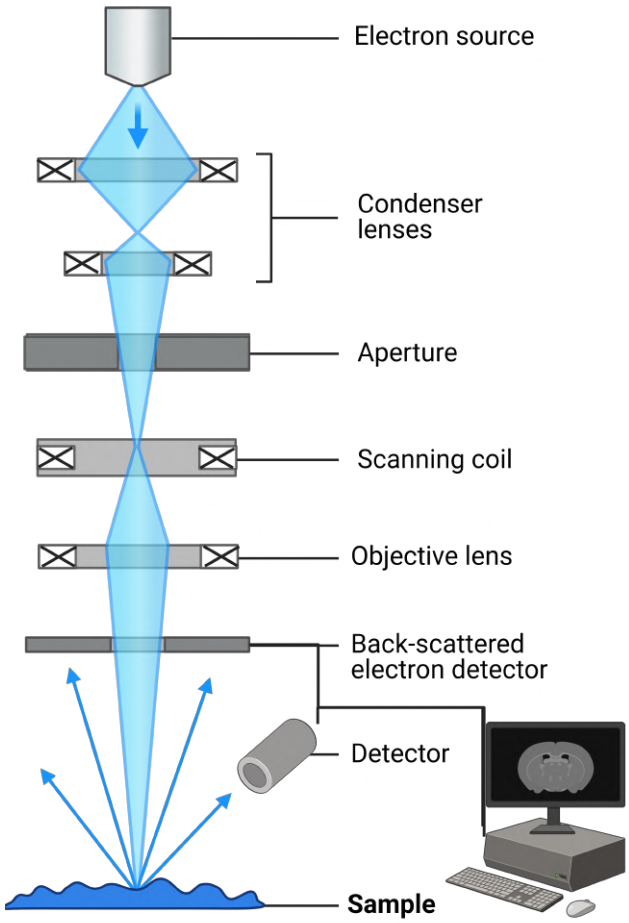

Figure 4.8: Scanning electron microscopy scheme.

In elastic scattering, the beam's electrons are deflected by atoms nuclei(back-scattering mechanism) or electrons with negligible energy loss, while in inelastic interaction, many emissions can follow:

- Secondary electron beam is generated by the sample's free electrons (conduction electrons), upon ionization process, induced by the incoming electron beam. The generated secondary electrons possess very low energy (3-5 eV), thus the collected signal have high spacial, low depth resolution, since secondary electrons can only escape few nanometers of the sample's surface.
  The emitted secondary electrons signal is detected by an Everhart–Thornley (ET) detector, that consists on a scintillator biased by 10 kV, covered by a Faraday cage, used to convert electrons energy into photons. Generated photons are later transported through a quartz pip, and converted into an electrical current signal by a photomultiplier tube (PMT). The generated current depends directly on the intensity of the detected SE signal(fig.4.10).
- Back-scattered electron beam result from an elastic collision between the incoming electron beam and the atomic nuclei of the sample, causing the electrons to be bounced

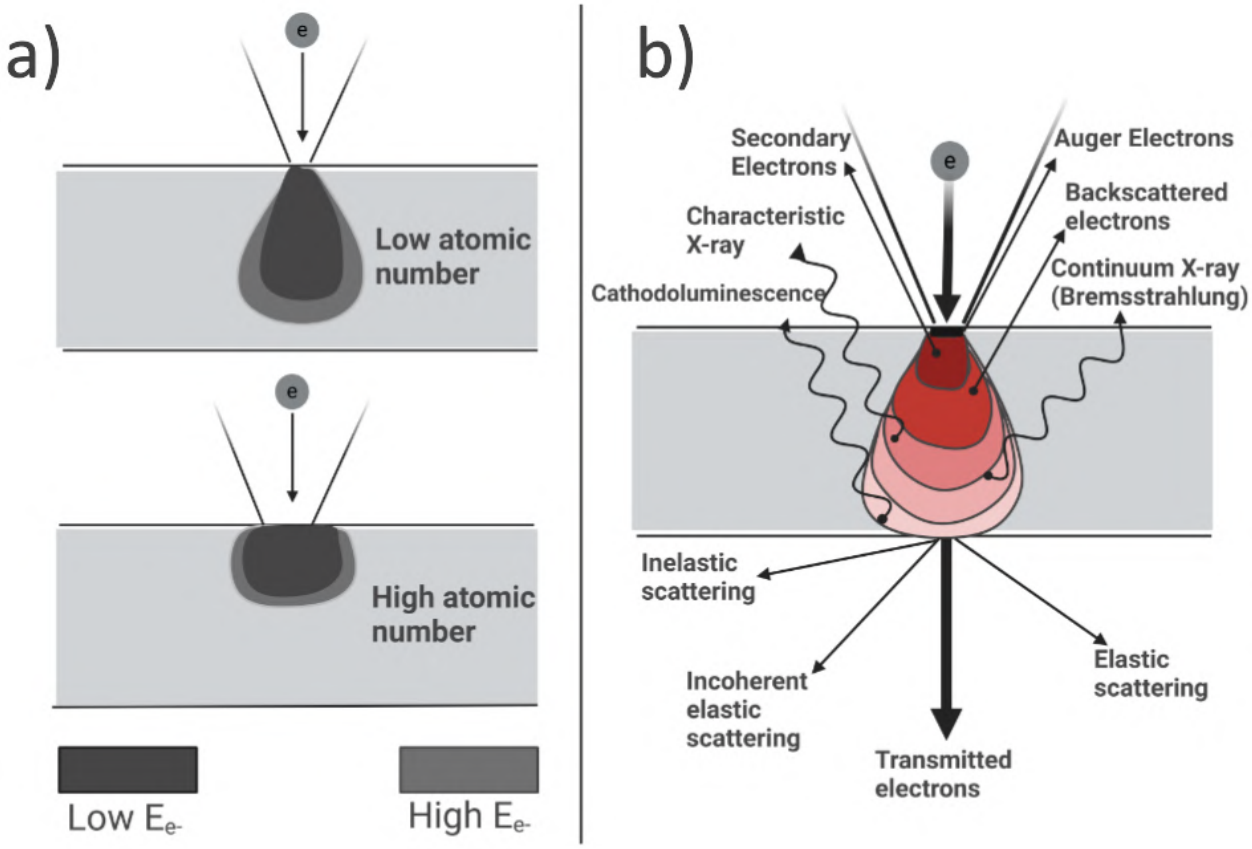

Figure 4.9: a) Interaction region between a low, and high energy e-beam with a low Z, and high atomic number Z . b) Different types of electron-sample emissions

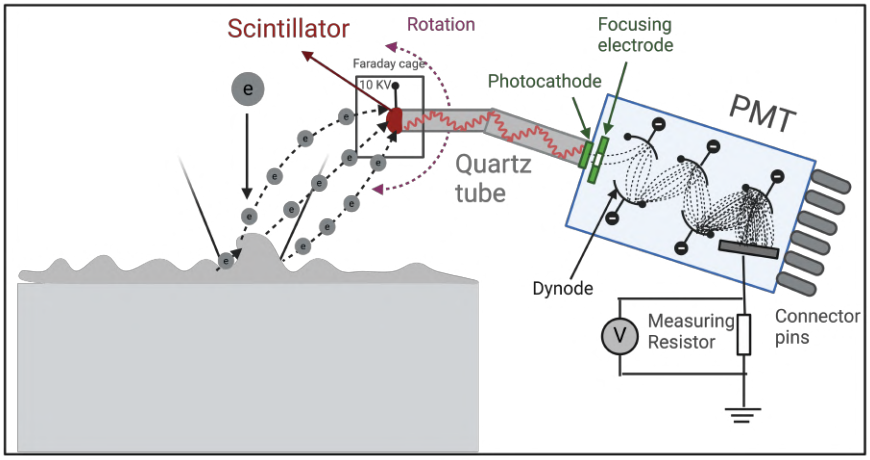

Figure 4.10: Secondary electron detection and signal generation.

back at energies ≈ 50 eV. The density of the back-scattered electrons is contingent upon the atomic number of the sample's nuclei(described by the BSE yield ν=n$_{BS}$/n$_{PB}$), a higher atomic number will result a greater back-scattered portion of the incoming

electron beam.
BSE have higher energy, compared to SE, thus offers stronger signal, with higher depth resolution(up to 1 μm) at the expense of spacial resolution. For BSE detection, ET detector can be used, without biasing the collector(anode), to avoid detecting the secondary electrons signal, however, in most SEMs, a second detector(BSD) is employed(right above the sample space), to detect back moving electrons(upward). The detected signal from back-scattered electrons is particularly useful for subsurface imaging and material elemental composition analysis.

- Characteristic X-ray and Auger emission manifest when the beam interact with core electrons(core electrons ejection), leaving vacancies in the valence band, after a period, an electron at higher energy level follow a transition, and fill the vacancy, emitting energy at the form of a characteristic X-ray, or transferred to a neighboring electron, and cause Auger electron emission (fig.4.11). characteristic X-rays are emitted from a higher depths than SE, BSE, and Auger thus offer higher depth resolution. These emissions are used for quantitative elemental analysis, band structure.

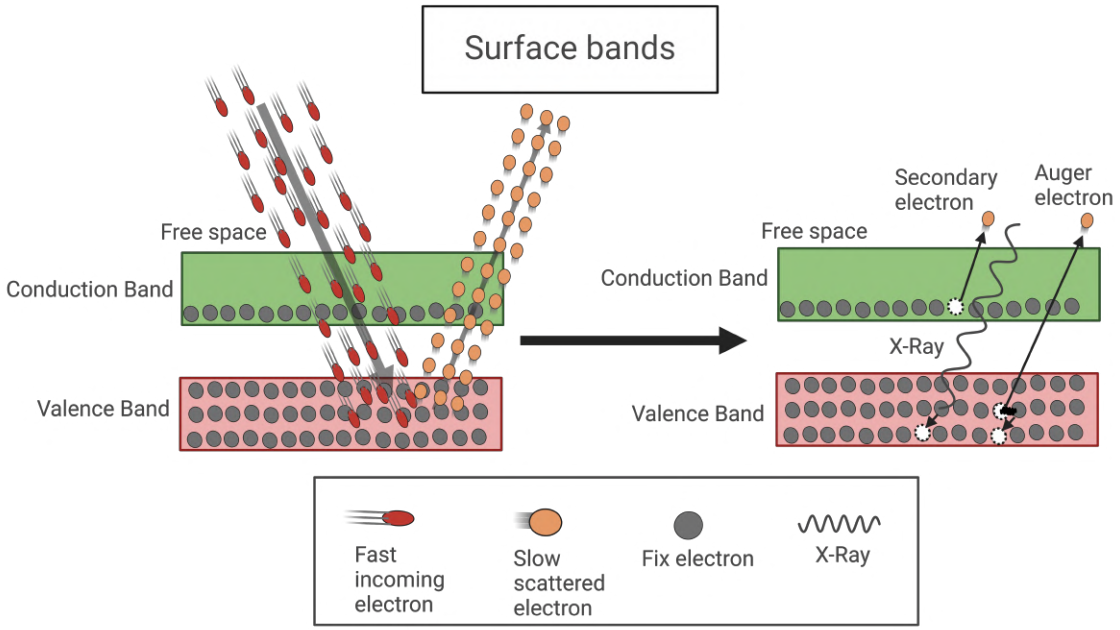

Figure 4.11: Different emissions from interaction between an electron beam with a sample's surface electrons.

- If the sample has an empty conduction band(insulators-semiconductors), the incoming beam can generate electron-hole pair(equ.4.4). Since the e-beam is very narrow, the generated current(Electron beam-induced current (EBIC)) is in the sub-picoamp, that can be measured and used to generate a current dependent image, useful for visualization of depletion region properties in a junction(pn-Schottky), for determining minority carriers properties, and their diffusion length, and mapping electrically active defects(purity

check for semiconductors) within the material.

$$\Delta N = \frac{(1-\nu)I_b E}{qE_{eh}} = \frac{GI_b}{q} \tag{4.4}$$

ΔN = number of generated electron-hole pair.
ν = BSE yield.
I_b = the beam current.
E_{eh} = electron-hole pair generation energy.

4.6.3 Beam generation, collection and image formation

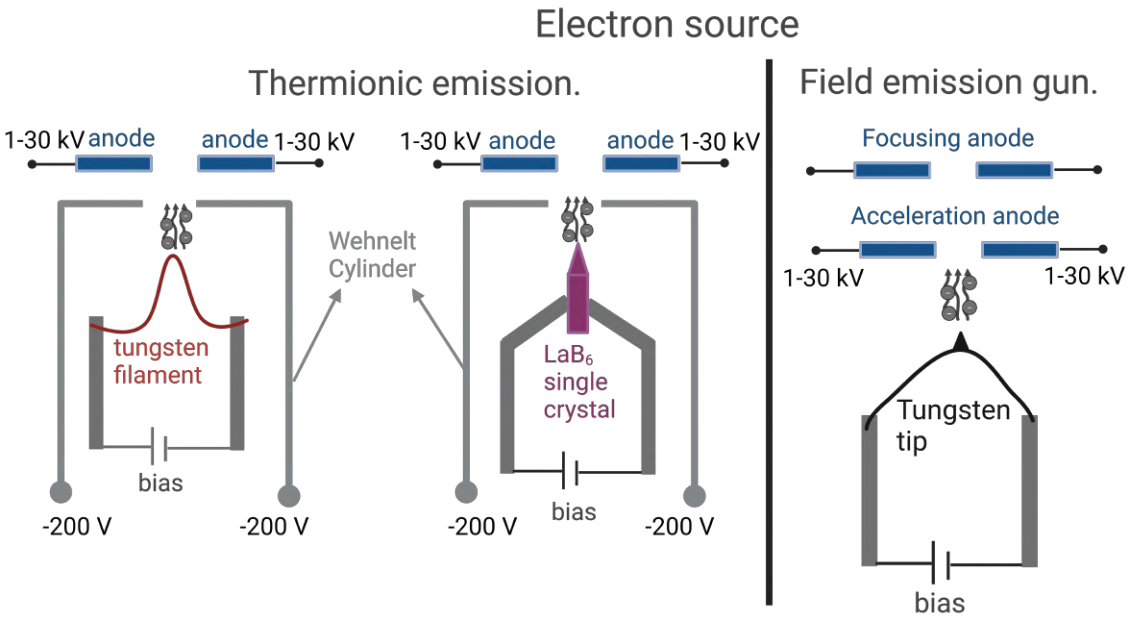

Figure 4.12: Electron source: Thermionic emission where electrons are ejected due to heat energy, and field emission where electrons are extracted by high electric field.

Scanning electron microscopes can be divided into three operational sections:

- Electron beam generation and acceleration is done by an electron gun(fig.4.12), and accelerating anodes.
- Convergence and focusing of the beam is done by a condenser and an objective lens(electromagnet). Adjusting the lenses focus and collimation, can be done by manipulating the magnetic field generated by the lenses.
- Surface scan is done using scanning coils(electromagnets), utilized to deflect the beam along different x-y positions. The measured signals are then used for a digital image construction, of the selected grid over which the scans where performed, each (x,y) position will be represented as a bit in the constructed image.

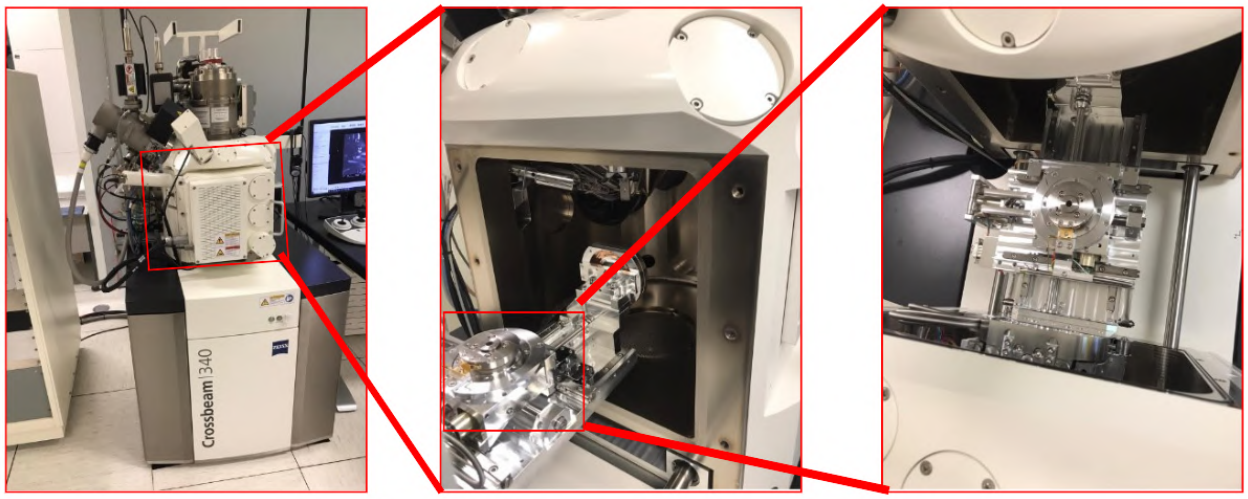

Figure 4.13: Scanning electron microscope.

4.7 Atomic force microscopy

4.7.1 Introduction

Atomic force microscopy is a probing technique, used to analyze surfaces morphology and other properties, at different scales, with a resolution that can reach up to a single molecule [61]. This technique consist on sensing attraction/repulsion forces, exerted by the sample's surface atoms on a sharp tip, when scanning the tip over the surface plane. The total force generated by the atoms at the surface on the tip, is a result of an interplay between attractive Van deer Waals, electrostatic, and repulsive contact forces(fig.4.14).

4.7.2 Forces

- Van der Waals forces are a result of electrons correlation, leading to a dipole formation between the electrons on the surface, and the tip, thus an attractive force $\propto r^{-7}$, will be generated. This force depends on the separating distance between the dipole, as well as the tip radius(equ.4.5).

$$F_{vdW} = \sum_{ij} F_{(vdW,ij)} = -\frac{A_H \cdot R}{\delta^2} \tag{4.5}$$

  A_H = Hamaker constant.
  R = radius of the tip.
  δ = separating distance between the two systems.

- Electrostatic charges can build up at the interfacing edges of the surface and tip, due to a potential difference between the two materials, resulting an attractive force that

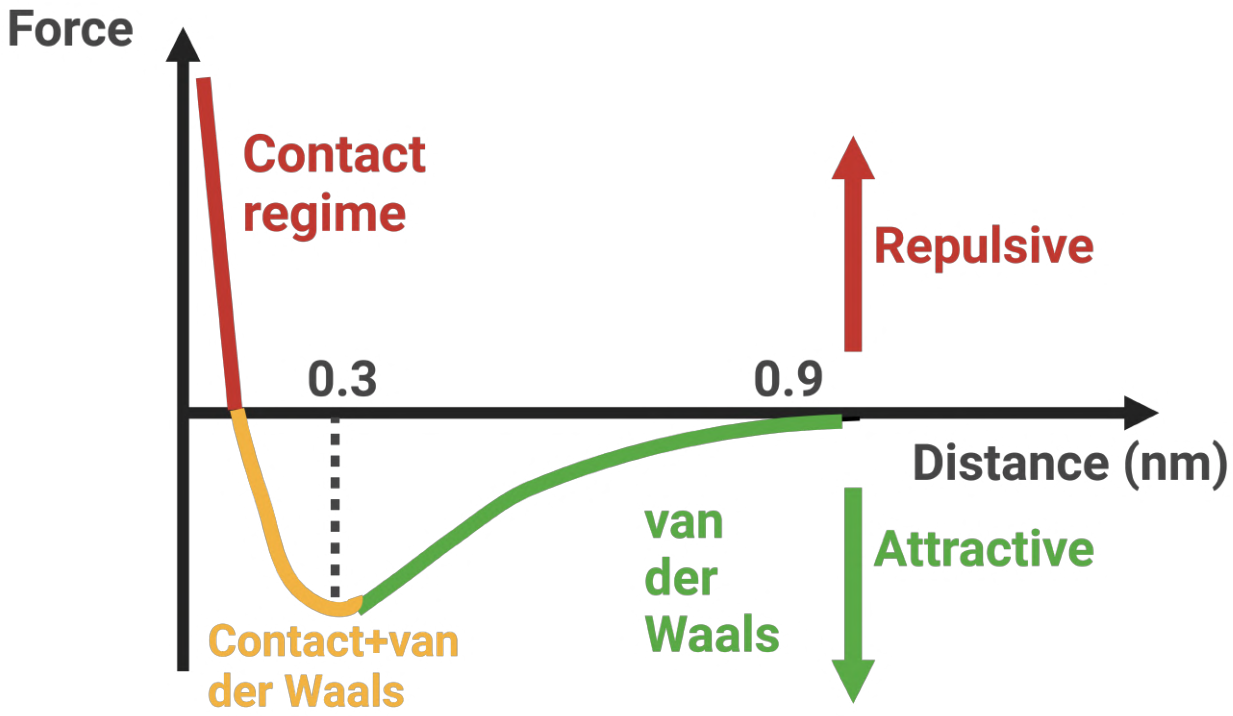

Figure 4.14: Forces between the AFM cantilever's tip, and sample's surface in function of the separating distance.

depends on the radius of the tip, potential, and separating distance(equ.4.6).

$$E = \frac{1}{2}CV^2 \tag{4.6}$$

$$F = \frac{dE}{d\delta} = \frac{1}{2}V^2\frac{dC}{d\delta} \tag{4.7}$$

$$\frac{dC}{d\delta} = \frac{2\pi\epsilon_0 R^2}{\delta(\delta + R)} \approx \frac{1}{\delta^2} \tag{4.8}$$

- Contact forces, arises when electronic filled shells of both tip and surface atoms overlap, resulting a repulsive force(as a consequence of electrons repulsion)($\propto$ r^{-12}), strong enough to deform the atomic elastic bonds. The stress-strain relation can be expressed by Hook's Law(equ.4.9).

$$\sigma_{ij} = E_{ijkl}\epsilon_{kl} \tag{4.9}$$

σ_{ij} = the stress tensor (force/area). E_{ijkl} = Young's elastic modulus tensor.
ϵ_{kl} = the strain tensor ($\Delta l/l_0$).
Many models were constructed to account for the repulsive force, for different tips shapes as a function of distance δ. In it's simplest forms, the tip can be considered to be spherical.

$$F_{rep} = \frac{4}{3}\cdot\frac{E}{1-\nu^2}\cdot\sqrt{R}|\delta^{3/2}| \tag{4.10}$$

ν is Poisson ratio that describes the compressability of the material, and R the spherically shaped tip radius.

4.7.3 AFM operation

For a basic operation, a cantilever equipped with a very sharp tip (50 nm), typically SiO2, is attached to a z scanner at the upper part of the instrument, while the sample is inserted at the bottom of the instrument on a sample holder, connected x and y piezo-scanners, allowing 2-d in-plane movement of the sample. The back of the cantilever is illuminated by a laser, and deflected to a PSPD (the simple case contains 2 PD),generating a voltage difference between the PDs. At first, the laser is calibrated at the center of the two PD, to result a zero voltage difference, once the tip is very close to the sample surface(interacting regime), the tip is attracted/repulsed(based on it's separating distance with the sample's surface (fig.4.14)). An initial set voltage is chosen V_{set}(in the attractive or repulsive regime), then the tip is set to perform x-y scans while measuring the forces generated on the tip at each coordinate. If in the attractive regime, and the tip encounters an increase in the forces applied to the tip, the cantilever will deviate from it's initial set-point, leading to a shift in the deflected laser, which in turn generates a voltage difference at the PSPD. This voltage is then compared to the initial V_{set}(by a differential amplifier), then the voltage difference is sent to a PID that acts to encompass the deviation from the initial V_{set}, by generating a signal to modify the height of the cantilever with respect to the surface.

The z scanner is controlled by two descending stages, an initial coarse motion, with a 30 mm range(0.1 mm resolution, and 30x10^4 DR), followed by a second mode, controlled by a piezoelectric crystal(6 mm range, at a 0.01 nm resolution).

The sensitivity S of the PSPD(the smallest detectable deviation), relates the PSPD output voltage with the cantilever deflection d_c by:

$$d_c = \frac{V_{PSPD}}{S} \tag{4.11}$$

S depends on the dimensions of the optical lever (L_C / L_D) and the PSPD amplification electronics.Typical values are of the order of S=100 V/mm, with a noise < 100 μV, allowing deflection detection up to 1 pm.
These deflections can be estimated by(equ/4.11), and converted into forces by correlating the defection to the elasticity of the cantilever, using Hook's Law:

$$F = k.d_C \tag{4.12}$$

With k being the force constant, that depends on both cantilever geometry, and materials elasticity(equ.4.13).

$$k = \frac{E.W.h^3}{4L^3} \tag{4.13}$$

4.7.4 AFM Modes

1. In contact mode, generated forces are resulted from a direct contact between the sample and the tip. As illustrated above, an approaching process is first performed, once the tip is in the interacting range, a set point is chosen initially V_{set}, then xy scans are performed by xy piezo electric crystals, over a given range. The measured potential at the PSPD is then compared to the V_{set} by differential amplifier connected to a PID-controller(Feedback loop) used to compensate the height difference, by controlling the z piezo, to re-obtain the initial V_{set}. This act is crucial for reducing errors caused by the difference between measured force and set-point force4.14.

$$V_e = V_{PSPD} - V_{set} \tag{4.14}$$

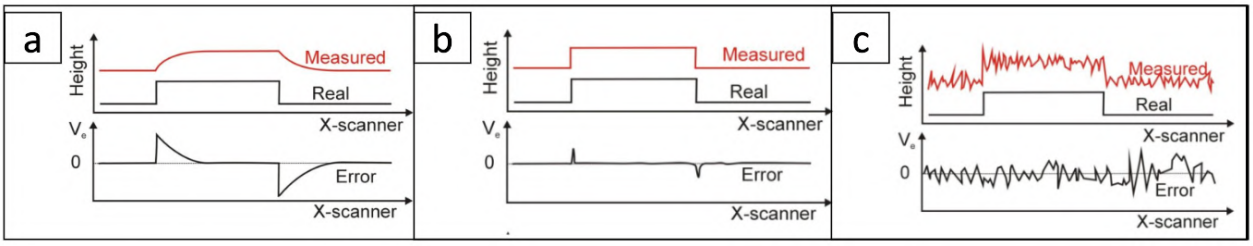

Figure 4.15: Signal comparison using a) low AMP gain,the z-scanner does not follow fast enough the changes in surface height, b) perfect gain, resulting a perfect response, and c) high gain, resulting a feedback too strong, and noises gets amplified.(taken from laboratory of nanoscience and nanotechnology-UNIBO).

Although contact mode AFM have a relatively simple operation,(one control parameter (V_{set}) + one feedback parameter), many disadvantages arises. In the attractive regime, forces are too low and unstable, while in the repulsive regime, the tip is continuously pressed against the sample surface, leading to tip and sample damage, a poor xy-image resolution, due to lateral deflection caused by the shear force, and image artefacts when probing materials with a non constant elastic modulus.

2. In dynamic mode AFM, the cantilever is set to a damping mode, controlled by a piezoelectric crystal, usually at the resonant frequency of the cantilever. At first, a damping frequency and amplitude are set by the user, then the damping cantilever approaches the surface, the V_{set} is chosen (most of the times in the repulsive regime to avoid operating in the instable regime). The setup requires an additional piezoelectric crystal and function generator, to control the damping amplitude and frequency ω_s,and a lock-in amplifier to measure the amplitude and phase of the generated signal, by the PSPD upon the deflected laser oscillation, a DAC is also implemented to acquire the amplitude and phase of the oscillation.

During surface scans, the tip follows a damping frequency shift if experiencing a force change(compared to the V_{set}), due to facing a surface height increase, or decrease, that

will result an amplitude(equ.4.15), and phase shift(equ.4.16), then the PID/controller act to compensate the height change, and to re-obtain the initial height (initial V_{set}).

$$A(\omega) = \frac{u_0 \cdot \omega_0^2}{\sqrt{(\omega_0^2 - \omega^2 - F_z'/m)^2 + \left(\omega^2 \omega_0^2\right)/Q^2}} \tag{4.15}$$

Where $u_0\omega_0$ are the initial amplitude and frequency, ω is the new frequency, F_z' is the force exerted by the surface on the tip, and Q is the quality factor of the tip.

$$\phi(\omega) = arctan\left[\frac{\omega \cdot \omega_0}{\omega_0^2 - \omega^2 - F_z'/m}\right] \tag{4.16}$$

Dynamic AFM offers lots of advantages, compared to contact mode, such as noise

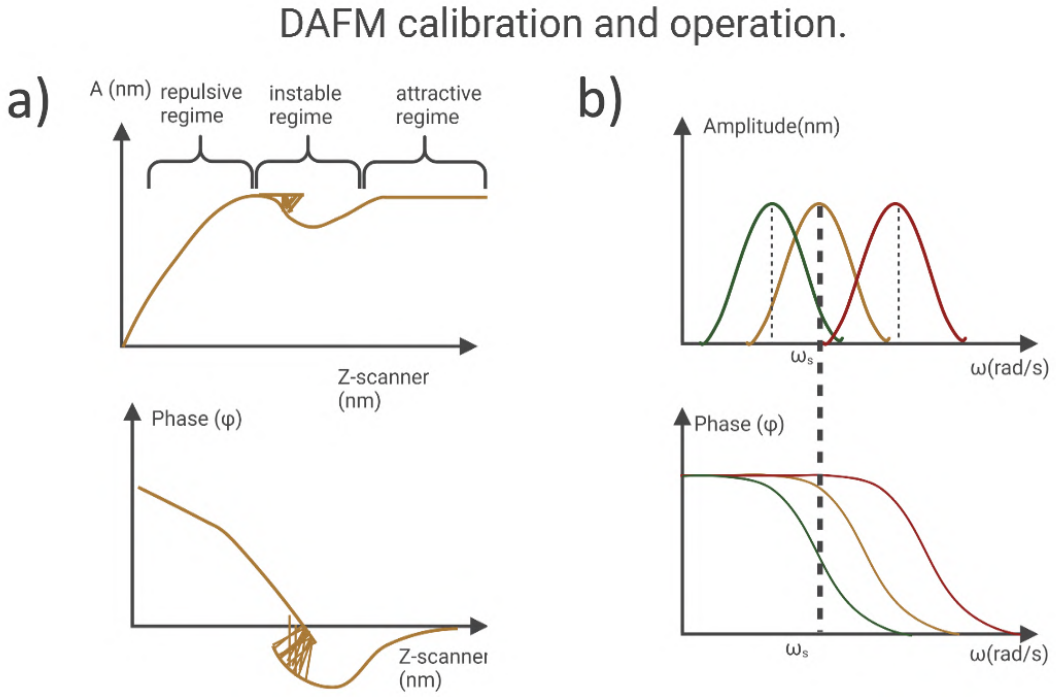

Figure 4.16: a) DAFM amplitude and phase plots, in calibration mode. b) both amplitude and phase of DAFM in operation mode, showing the initial calibrated resonance frequency, and two frequency shifts(taken from Laboratory of nanoscience and nanotechnlogy-UNIBO).

reduction, by the Lockin Amplifier, no snap-in or pull-off instabilities(caused by electrostatic discharges), possible operation in non-contact mode, thus reduced damage of sample and tip, due to absence of shear forces, and phase analysis, that contains information about energy dissipation with the sample.

AFM can be used to measure surface topography, but also other surface characteristics such as electrical properties(Conductive AFM), by performing spacial (x,y), IV measurement, through an applied bias between the surface and the conductive tip, elastic properties, by measuring

pull-off forces, generated upon pressing mechanism, Piezo-response Force Microscopy (PFM). Also, it is possible to probe other forces (electrostatic forces), that can be used to map surface charges at the nano-scale(Kelvin probe force microscopy KPFM). Kelvin probe force microscopy(KPFM), is a contact mode AFM, used to probe electrostatic forces. A frequency modulation is performed(equ.4.17), to decouple the electrostatic signal from other signals(equ.4.18).

$$\Delta V = V_{Sam} - V_{tip} - V_{AC} \cdot sin(\omega_{KP} \cdot t) \tag{4.17}$$

$$F_{el,\omega} = \frac{1}{2}\frac{C}{D^2}(V_{sample} - V_{tip})V_{AC}sin(\omega t) \tag{4.18}$$

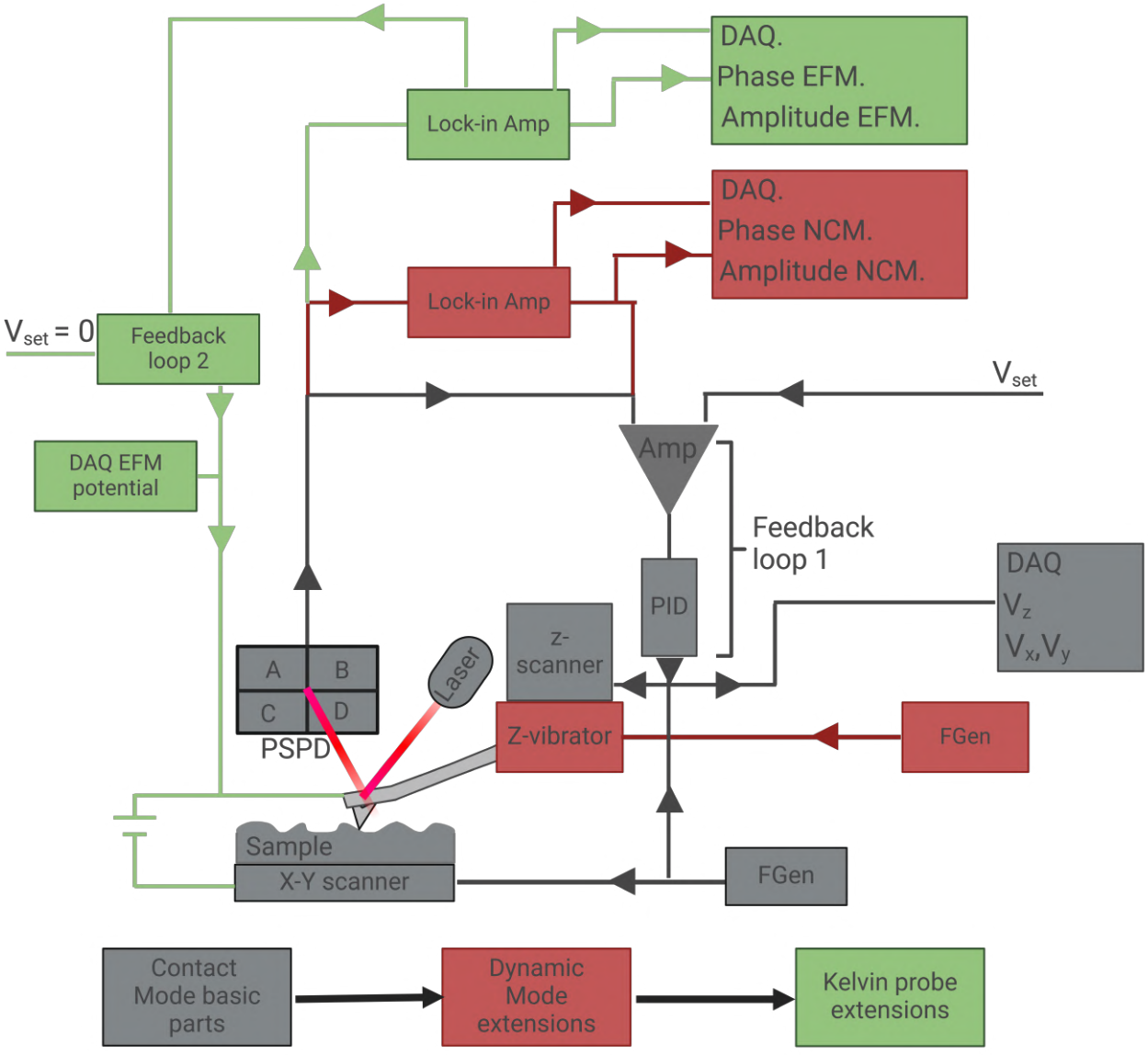

Figure 4.17: AFM experimental setup, for different operation modes.

4.7.5 AFM image visualization, filtering and analysis

An AFM image is obtained as a result of z measurements, performed at a set of (x,y) scans, the slab size is set by the (x,y) range, while the resolution by the spacing between consecutive (x,y) scans. The scan can be performed vertically, by performing an n (forward-backward) x scans, at each y, or horizontally, by preforming an n, y scans, at each x. As a result four files can be generated, containing amplitude and phase of each measurement, in the forward, and backward direction(fig.4.18).

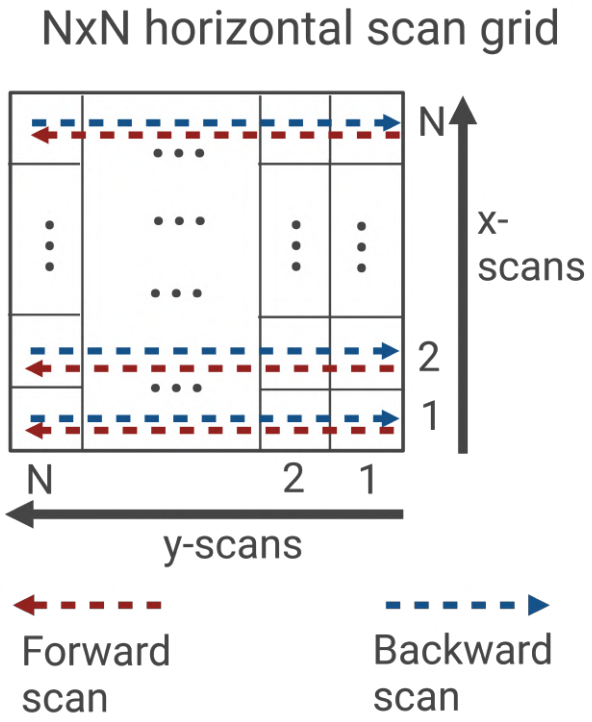

Figure 4.18: Scanning grid in horizontal double acquisition mode, the image size is NxN (x,y) bits.

The obtained image will have many artifacts resultant from constant offset, tilted sample, unstable tip-sample interaction, thermal drift, periodic noise,piezo-scanners etc.

To refine the images as much as possible, many filtering processes can be performed, starting from the removal of tilted plane background, followed by a removal of curved (polynomial background), generated by the piezo-scanner non-ideality. Then removal of thermal drift, is done by line averaging. In general filtering can be very useful to remove predicted artifacts, but too much filtering can lead sometimes to information loss.

Many statistical means can be used to analyze different topographic characteristics such as

roughness(equ.4.19), height pdf, grains number, average grain sizes, 1-D 2-D fft...

$$R_q = \sqrt{\frac{1}{MN}\sum_{m=1}^{M}\sum_{n=1}^{N}(z(x_m, y_n) - < z >)^2} \tag{4.19}$$

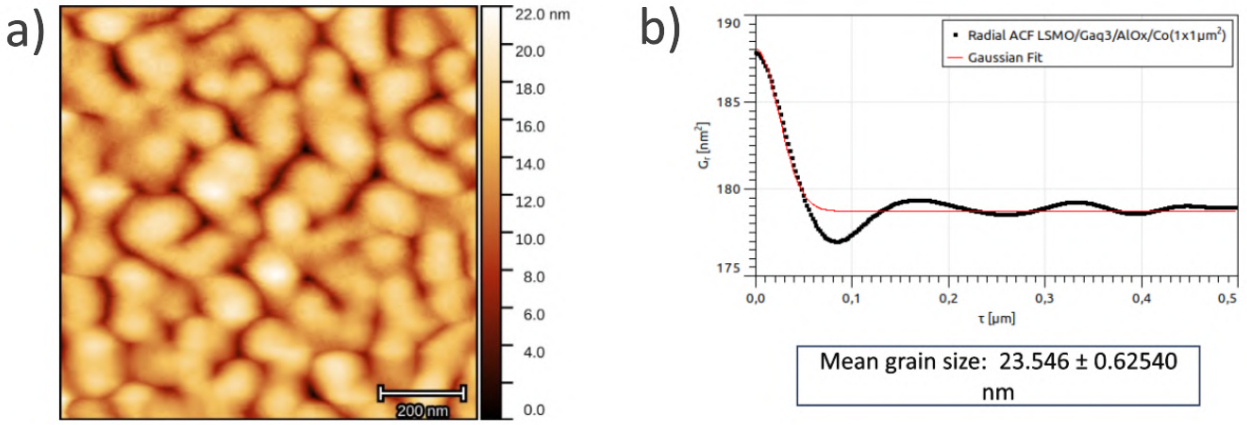

Figure 4.19: a) AFM image of LSMO/Gaq3/AlOx/Co surface. b) Surface grain analysis using the autocorrelation function, estimated grain size is 23.54 ± 0.62 nm.

First order statistical quantities can be very useful for single point analysis, however a complete surface analysis demands second order functions, such as the autocorrelation function. A very powerful tool, used to analyze grain sizes distribution, when grains are randomly distributed on the surface, with a grain size, estimated as the standard deviation of a Gaussian distribution [62].

$$G(\tau_x, \tau_y) = \int\int_{-\infty}^{\infty} z_1\, z_2\, w(z_1, z_2, \tau_1, \tau_2)\, dz_1\, dz_2 \tag{4.20}$$

$$= \lim_{S\to\infty} \frac{1}{S}\int\int_S \xi\,(x_1, y_1)\ \xi\left(x_1 + \tau_x, y_1 + \tau_y\right) dx_1\, dy_1 \tag{4.21}$$

z_1 and z_2 = values of heights at points (x_1, y_1), (x_2, y_2).
τ_x = x_1-x_2.
τ_y = y_1− y_2.
w(z_1, z_2, τ_x, τ_y) = the two-dimensional probability density of the random function $\xi(x, y)$ corresponding to points $(x_1, y_1), (x_2, y_2)$, and the distance between these points τ.

Chapter 5

Magnetic tunnel junction

5.1 Introduction

Resistance switching materials (memristors), are one of the promising NV materials, suggested for new generation RAM, and NC applications [20,63], due to their NV (memristive) nature (see.1).

Valence change materials are memristors that can exhibit resistance change as a result of ionic

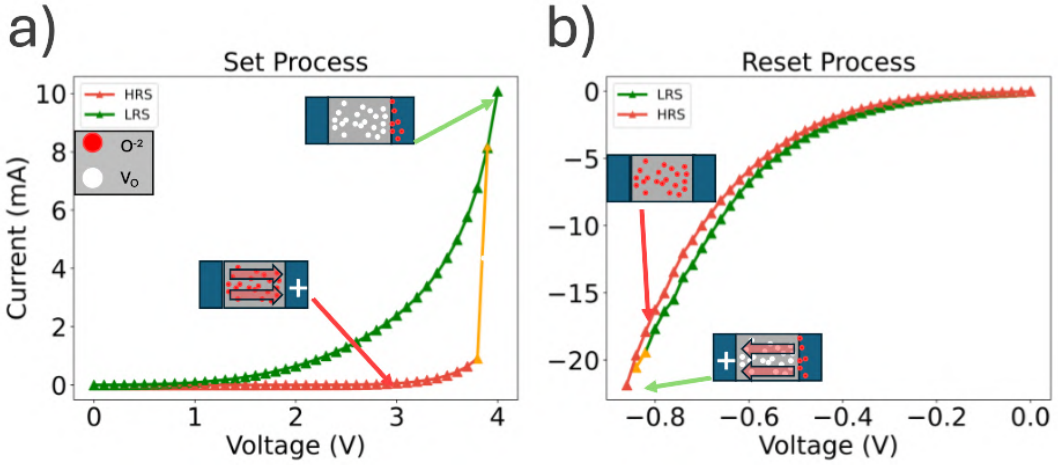

Figure 5.1: a) Set process, the device experience resistance modification as a result of conductive filament formation. b) Reset process, the device re-obtain it's initial resistance, due to the destruction of the conductive filaments.

diffusion. Many binary transition metal oxides such as TiO2 [64,65],TaO2 [66,67],Al2O3 [68,69] etc. belong to this type of materials, and already show this effect, which consist on formation or destruction of conductive filaments inside the metal oxide layer, due to oxygen ions migration back and forth from the metal-oxide layer toward one of the electrodes, as a result of high applied voltage. These materials are characterized by having a non linear IV characteristics (fig.5.1) [20,70].

Other technology suggested for memory and computing applications are spintronics, these magnetic multistructures may exhibit magneto-resistance effect (see.2.4.3). Similarly, these materials attracted huge interests for many application such as sensing(linear magnetic transducers), due to their high sensitivity to magnetic fields(up to 1 nT at room temperature), data storage(read heads,hard disks), and other automotive, recording, biological related applications [71].

The mix between these two types of resistance switches was reported by [72], where they were able to show two different resistance switches, caused by both TMR and ionic diffusion [72,73].

In this chapter we will focus on the exploitation of both resistance and magnetoresistance effects in a Co/AlOx/Co magnetic tunnel junction (MTJ), as well as the size effect on the devices operation. The analysis will involve a full description of all operating parts in the device such as top/bottom electrodes, and the device itself by means of IV and MR measurements, at room, as well as low temperatures (100 K).

5.2 Experimental details

A cleaning process of a sapphire single crystal substrate was performed by ultrasonic treatment, while immersed in acetone solution, for two cycles, 15 min each, then in isopropanol for the same amount of time, followed by annealing at 255°C, for 30 min to dry the sample, then rested for 2 hours to slowly cool down to about 40°C. The deposition consisted on 3 EBL patterning of PMMA to allow the deposition of 9 bottom electrodes, AlOx on top of the bottom electrodes, and then 9 top electrodes respectively. The first deposition consisted on a 10 nm Co using EBPVD, the second consisted on 3 consecutive, 2 nm Al layer using PVD, each followed by oxidation process (O_2 exposure), to increase the oxygen concentration in the insulating layer, resulting a 6 nm AlOx layer, while the third consisted on a 10 nm Co EBPVD. Lift-off using acetone was performed after each deposited layer, all used deposition characteristics are presented in (tab.5.1). To avoid shorts between the two electrodes, cross-linking of PMMA using high dose EBL was performed after the first deposition to create an insulating window on top of the bottom electrode, that was then filled by the AlOx layer.
To clarify, the fabrication was performed in collaboration between two institutes, and I was not involved in it.
The final substrate hosted 9 devices, with the same cross sectional thicknesses, comprised of two 10 nm Co electrodes separated by a 6 nm of AlOx. Each row contained identical devices, the first row had 50x50 μm^2 sized devices, the second 10x10 μm^2, while the third 5x5 μm^2 (fig.5.2). Devices were first SEM imaged, then devices and devices electrodes were IV probed at a probe station, with low reading voltages (-100 mV), using 4-point, 2-point probe respectively, then the substrate was placed on a chip carrier, devices electrodes were connected to the electrode pads using a wire bonder, then the chip was mounted on top of the sample holder (fig.4.7), and placed in a cryostat, where IV, and MR measurements were performed at room and low temperature (100 K).

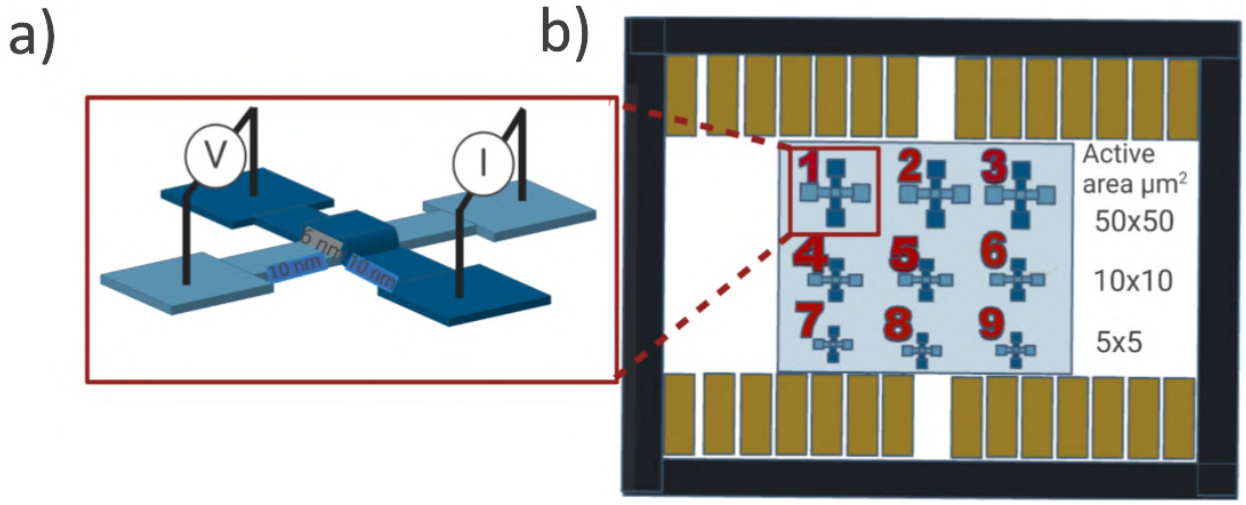

Figure 5.2: a) Devices cross section. b) Substrate housing 9 devices, placed on a chip carrier, connected to electrode pads. All devices shares the same cross sectional thicknesses(10 nm/6 nm/10 nm), but each row have different device size(50x50/10x10/5x5) μm^2.

Layers	Pressure (mbar)	deposition rate (nm/min)	exposure time (min)
Co (EBPVD)	1.8×10^{-10}	0.2	50
3x Al(PVD)	10^{-8}	0.6	3.5
3x Oxidation	5×10^{-8}		30
Co (EBPVD)	1.8×10^{-10}	0.2	50

Table 5.1: Deposition characteristics.

For the resistance estimation, IV were performed using low reading voltages(100 mV), applied to bottom electrodes, while current was measured at top electrodes. For the MR measurements, all devices were characterized in a similar fashion, resistance estimation was done by low reading voltages (-100 mV), while subjecting the substrate to a cyclic magnetic induction sweep between [300;-300] mT, and for the resistance temperature measurements, resistance estimation was performed similarly to the MR, estimated after each 5 K decrease in the temperature.

5.3 Results and discussion

1. **Electrical characterization**

   At room temperature, all electrodes showed an increase in their resistance when scaling down the electrodes size (tab.5.2), however a resistance difference was observed between top and bottom electrodes, observed at all the devices, indicating a possible size difference. While devices showed a big variance in their resistance, and resistivity, but with a clear resistance increase when scaling down the active areas, resulting an

Devices	Top electrode Average Resistance(Ω)	Bottom electrode Average Resistance(Ω)
50x50 μm^2	500 ± 55	280 ± 70
10x10 μm^2	600 ± 100	390 ± 110
5x5 μm^2	820 ± 70	600 ± 40

Table 5.2: Devices top and bottom electrodes average resistances, for each row.

average resistance of 65 MΩ, 2 GΩ, and 13 GΩ, for 50x50 μm^2, 10x10 μm^2, and 5x5 μm^2 respectively. The resistivity change was attributed to the unpredictable initial resistance state typical in this type of materials.

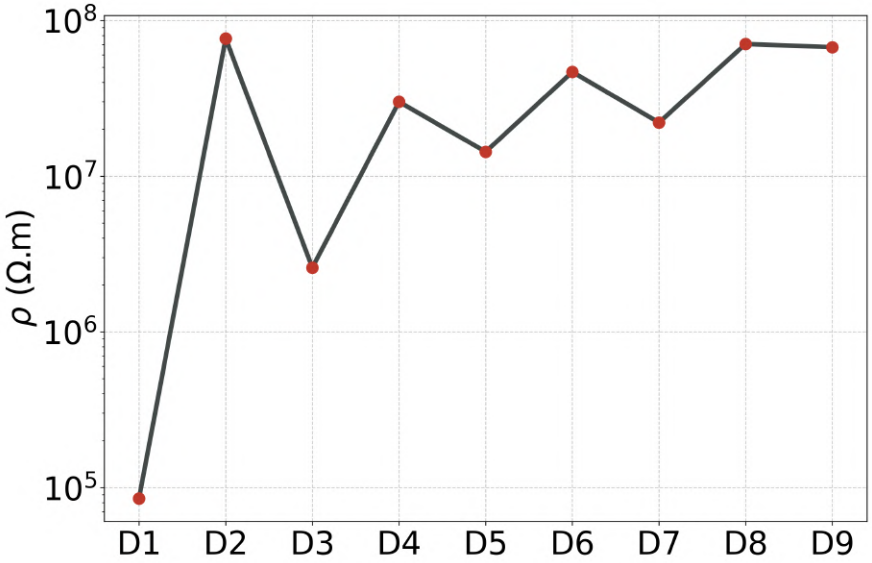

Figure 5.3: Devices resistivity, obtained by a 4-point probe. Devices shows orders of magnitude variation in their resistivity.

Device	Resistance (Ω)	Resistivity($\Omega \cdot m$)
D_1 (50×50 μm^2)	$200 \times 10^3 \pm 750$	83×10^3
D_2 (50×50 μm^2)	$190 \times 10^6 \pm 2.5 \times 10^6$	79×10^6
D_3 (50×50 μm^2)	$6 \times 10^6 \pm 1 \times 10^6$	2.5×10^6
D_4 (10×10 μm^2)	$2 \times 10^9 \pm 0.2 \times 10^9$	33×10^6
D_5 (10×10 μm^2)	$1 \times 10^9 \pm 1 \times 10^7$	16×10^6
D_6 (10×10 μm^2)	$3 \times 10^9 \pm 4 \times 10^7$	50×10^6
D_7 (5×5 μm^2)	$5 \times 10^9 \pm 5 \times 10^7$	21×10^6
D_8 (5×5 μm^2)	$17 \times 10^9 \pm 1 \times 10^8$	70×10^6
D_9 (5×5 μm^2)	$16 \times 10^9 \pm 1 \times 10^8$	65×10^6

Table 5.3: Devices resistance and resistivity.

Based on the SEM images, all devices showed similar deformation at the top region

of devices active areas (fig.5.4), that did not scale when scaling down the device, thus becoming significant for small devices.

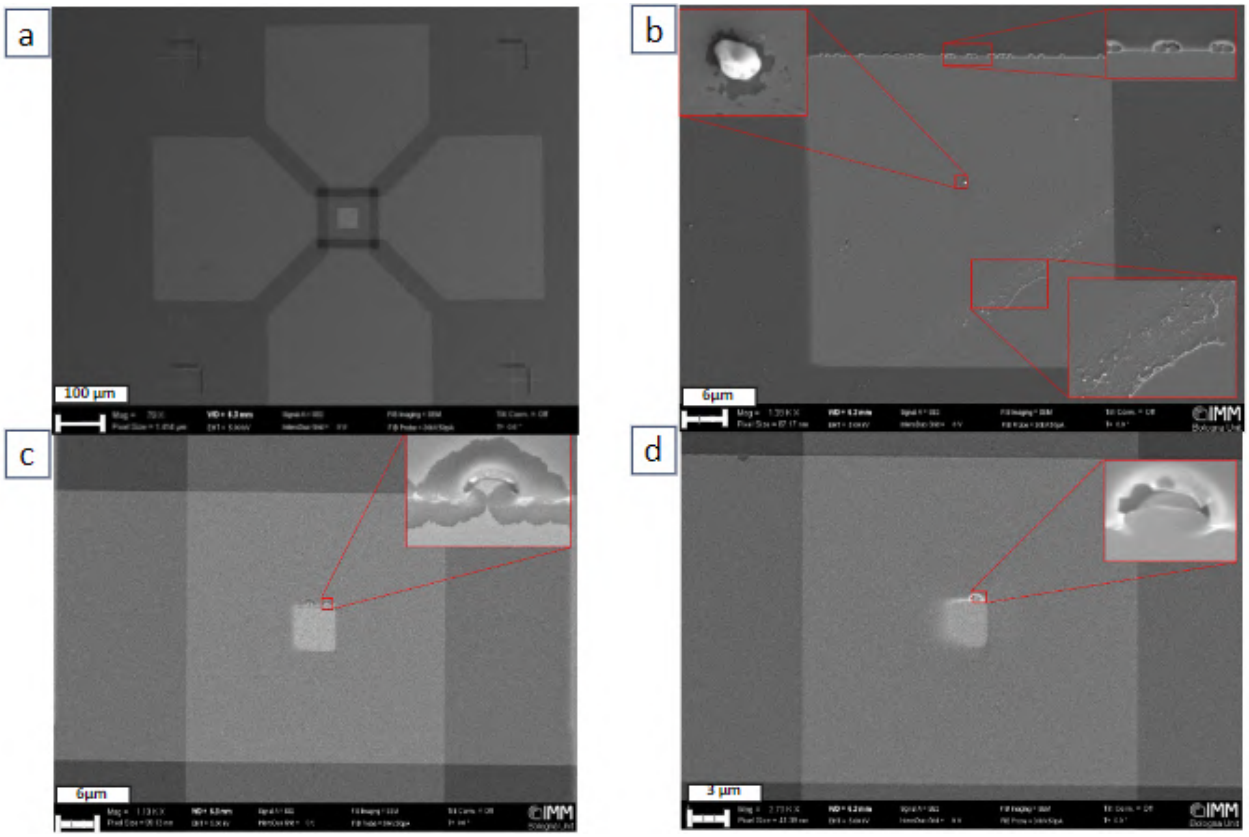

Figure 5.4: SEM images of a) 50x50 μm^2 while device. b) 50x50 μm^2 device's active area. c) 10x10 μm^2 device's active area. d) 5x5 μm^2 device's active area.

At room temperature, resistances collected at the cryostat were similar to that of the probe station. When cooling the substrate, resistance change was measured for two 50x50μm^2 devices, then fitted using inelastic hopping via chains of multiple localized states [14], 4 channels hopping was in accordance with the collected data (fig.5.5).

At low temperatures, small devices showed resistance in the TΩ range, therefore we focused our attention on bigger devices (50x50 μm^2).
At 100 K, devices were subjected to high applied voltages in attempt to modify there conductance. Indeed, a reversible conductance change was reported (fig.5.7). To make connection with the adopted electrical transport mechanism(amorphous tunneling), conductance/voltage of both before and after conductance modification were plotted and fitted using (equ.2.19). Devices initial conductance were in good agreement with 4 channels model, thus validating the transport mechanism suggested previously (fig.5.5).

Device	G_0	$G_{4/3}$	$G_{8/3}$
1 (50x50 μm^2)	$2.35x10^{-05}$	$4.79x10^{-09}$	$2x10^{-12}$
3 (50x50 μm^2)	$9.95x10^{-09}$	$1.05x10^{-11}$	$3.79x10^{-15}$

Table 5.4: 3 channel GT amorphous tunneling model,table of estimated parameters(equ.2.19).

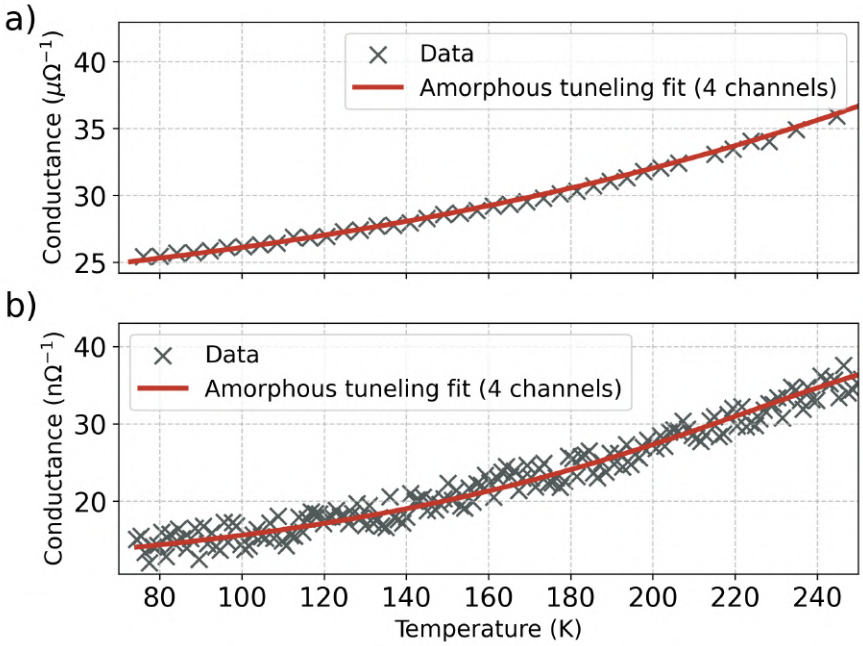

Figure 5.5: Conductance-temperature characteristics of two 50x50 μm^2 Co/AlOx/Co MTJ, between 270 K and 74 K, fitted using 4 channels amorphous tunneling [14], parameters estimation are summarized in (tab:5.4).

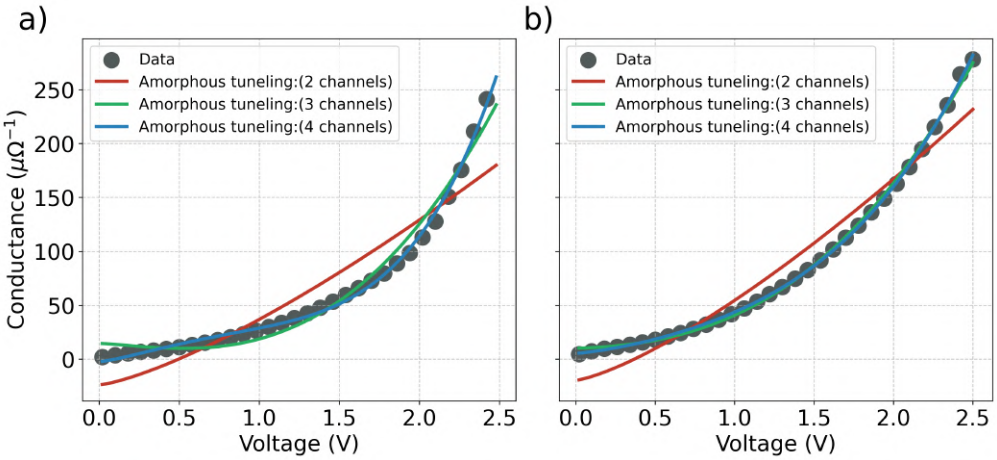

Figure 5.6: Conductance voltage characteristics a) before conductance modification, and b) after conductance modification. Results are fitted using Amorphous tunneling model [14], considering 2, 3 and 4 channels hopping, estimated parameters are represented in (tab.5.5).

State	G_0	$G_{4/3}$	$G_{8/3}$	$G_{12/3}$
HRS 4 channels	$1.47x10^{-6}$	$1.63x10^{-5}$	$1.2x10^{-6}$	$1.35x10^{-6}$
LRS 4 channels	$3.19x10^{-6}$	$1.81x10^{-5}$	$5.88x10^{-6}$	$4.97x10^{-7}$
HRS 3 channels	$4.85x10^{-6}$	negative	$1.57x10^{-5}$	
LRS 3 channels	$4.68x10^{-6}$	$1.03x10^{-5}$	$1.2x10^{-5}$	

Table 5.5: Estimated parameters, from the conductance voltage fit, using the amorphous tunneling model (equ.2.19).

2. **Electrical bistability**

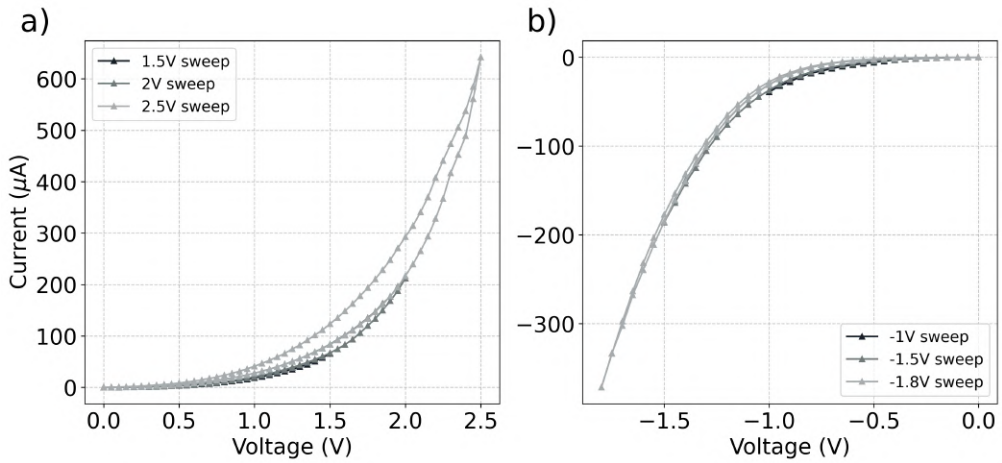

Figure 5.7: Device IV characteristics, at different consecutive a) positive voltage, and b) negative voltage sweeps. Hysteresis was observed in both, indicating the modification of the device resistance (decrease after positive sweeps, and increase after negative sweeps).

Devices were subjected to low to intermediate positive sweeps (fig.5.7.a)), in search for any modification in the devices conductance, a conductance increase was first reported after [0;2]V, viewed by a hysteresis in the IV, then at [0;2.5] V (our considered 'LRS'). Then consecutive negative sweeps were performed (fig.5.7.b)), a partial reset was first observed after -600 mV, followed by consecutive resets at different increasing voltages amplitudes, up to -1.8 V (our considered 'HRS'), after which a new 'HRS' different from the 'IRS' was reported, indicating an initial (intermediate) resistive state. The same set-reset was performed for a second time, using sweeps identical to the ones used before, and it was possible to re-achieve almost the same intermediate states, with small deviation.

To view the endurance of the 'HRS'/'LRS' switch, a set of 10000 cycles was performed, each composed of a +2.5 V set pulse, followed by a -1.8 V reset pulse, after each pulse reading process was carried out using small applied voltages (-100 mV) (fig.5.8), after 1600 cycles, the switch was destroyed.

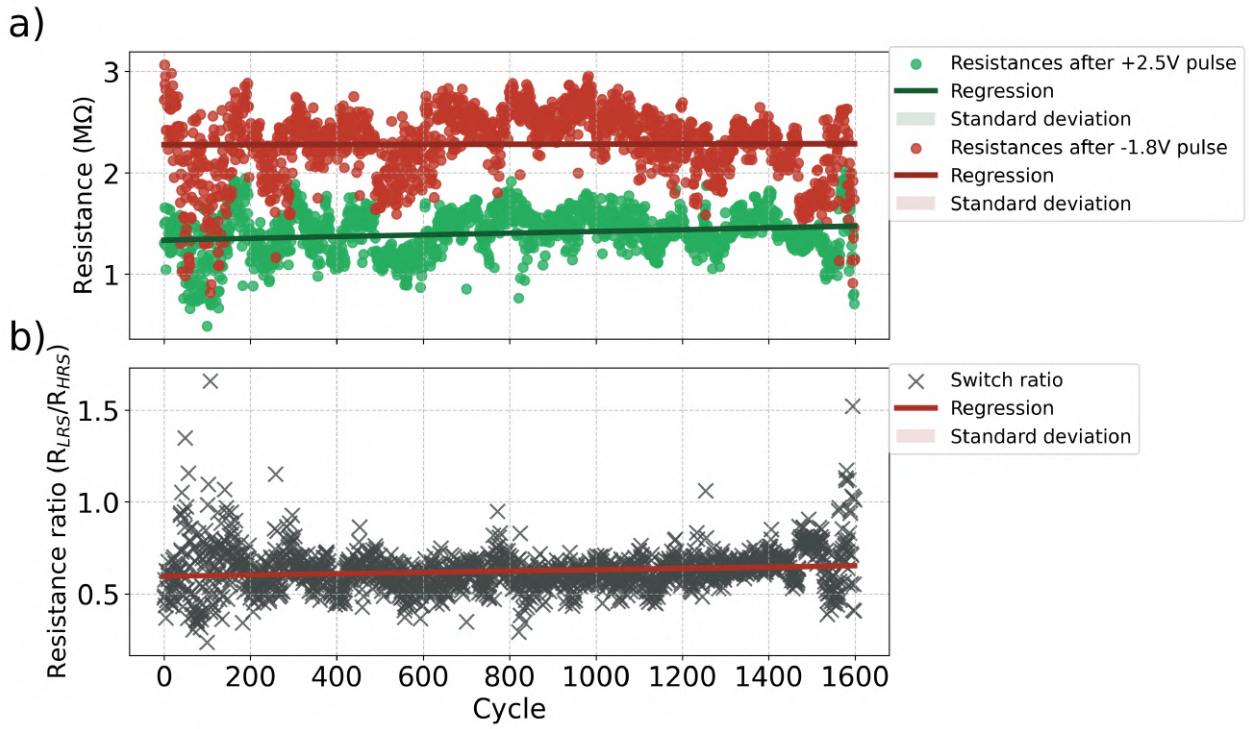

Figure 5.8: Endurance check of a 50x50 μm^2, at 100 K, the device showed an endurance up to 1600 cycles of 2.5/-1.8 V pulses, and a ratio up to 0.6, resistance measurement was done after each pulse using low reading voltage (-100 mV). b) ratio between 2.5 V and -1.8 V resistances.

3. **Magnetoresistance characterization**

For the magneto-resistance measurements,and given the cross geometry of the electrodes,

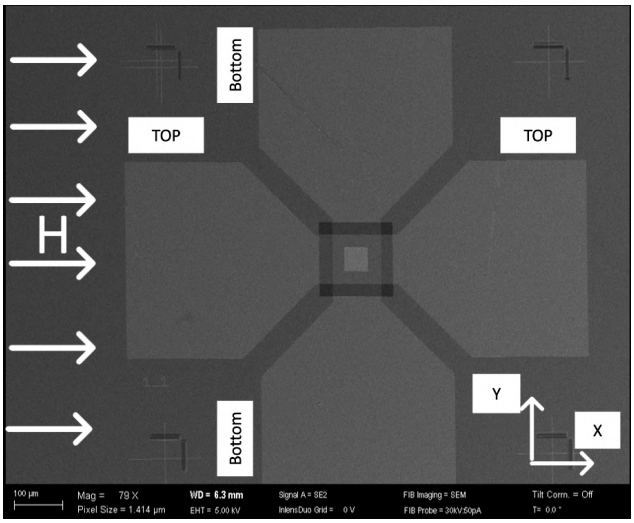

Figure 5.9: Magnetic field direction, with respect to top and bottom electrodes.

the magnetic induction was applied in the longitudinal direction of top electrodes, while

in the traverse direction for bottom electrodes (fig.5.9).

At room temperature, devices didn't show any MR effects (fig.5.12.a)), while all electrodes showed AMR with about -0.4% (fig.5.10). A coercivity mismatch was reported between the two electrodes, indicating the presence of an in-plane anisotropic distribution of the demagnetization field, and in correlation with the resistance difference between the two electrodes represented earlier, shape related anisotropy was suggested.

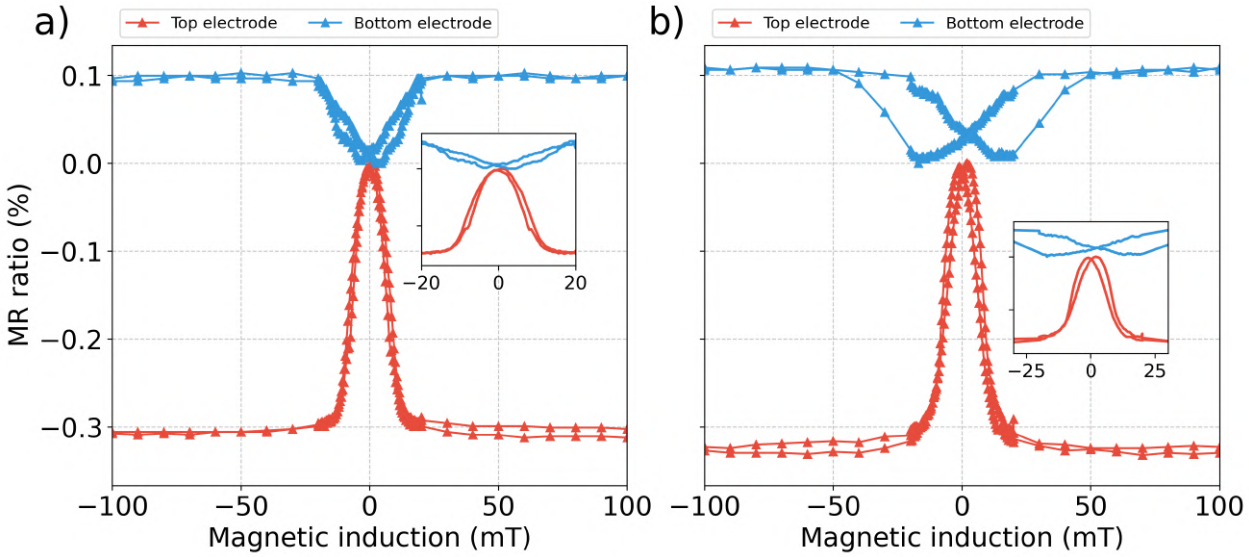

Figure 5.10: MR ratios for bottom and top electrodes at a) room temperature, and b) Low temperature (100 K).

To check this hypothesis, micromagnetic simulations(using mumax), were performed to study the in-plane coercivity angle dependence for different slabs dimensions (x,y), always satisfying y=2x, and fixing z at 10 nm, in accordance with the electrodes geometries, used parameters are represented in (tab.5.6). Small slabs showed an in-plane anisotropic H_C (fig.5.11), but as scaling up the slab size, both coercivity's magnitude, and angle dependence decreased, up to becoming negligible for slabs 1 order of magnitude smaller than the actual electrodes. We were not able to increase the slab size anymore, due to computing limitations, however the trend is in accordance that a shape anisotropy is absent.

Saturation magnetization (A/m)	1400×10^3
Magnetic induction (mT)	250×10^3
step (mT)	1×10^3
Landau-Lifshitz damping constant	0.02
Exchange stiffness (J/m)	13×10^{-12}

Table 5.6: Micromagnetic simulation parameters.

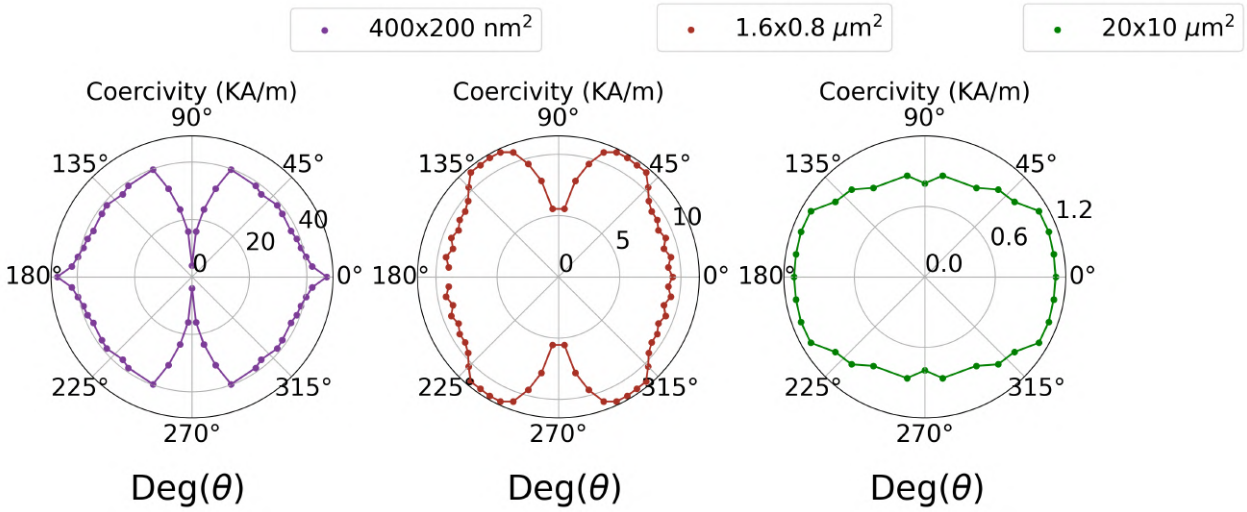

Figure 5.11: Coercivity, in-plane polar plot for different slabs dimensions, extracted from micromagnetic simulations.

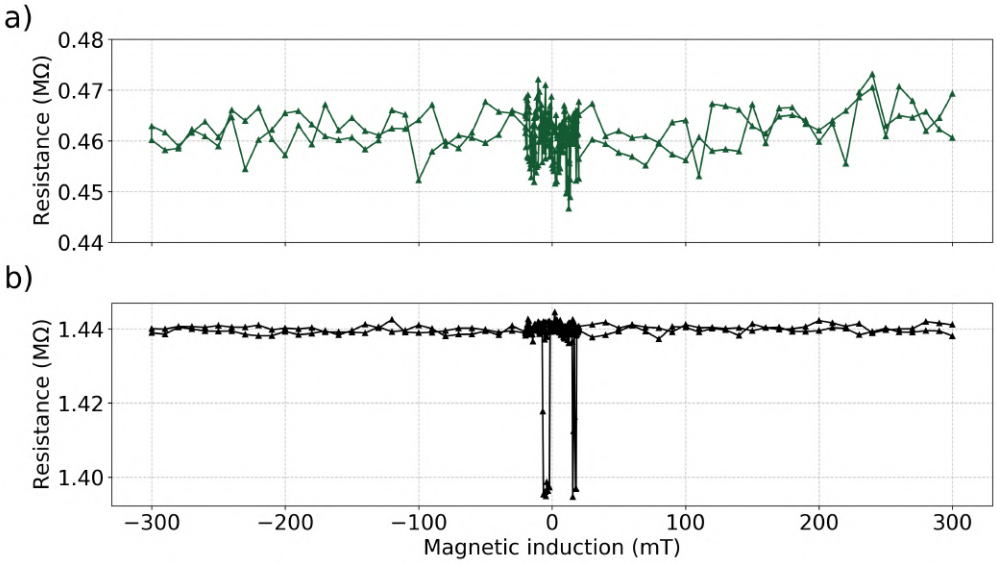

Figure 5.12: $50{\times}50\mu m^2$ MTJ MR at a) room temperature, and b) 100 K at the initial resistance state. No TMR was observed at room, nor at low temperature, only random telegraphic noises.

At 100 K, no change in the AMR ratio was observed, however top electrodes coercivity increased drastically compared to bottom electrodes. As for the devices, no TMR was observed at the initial resistance state, except some random telegraphic noises [74] reported at low applied voltages, and were attributed to trapped charges in some already present conductive filaments (fig.5.12), these discharges were more frequent at intermediate and 'LRS'.

5.4 Conclusions

A reversible resistance switch was reported after +2.5V/-1.8V set/reset pulses, with an endurance up to 1600 on/off cycles, and an on/off ratio of 0.6.

Charge transport in these devices was in accordance with inelastic hopping via chains of multiple localized states [14], that was consistent with both GT and GV acquired data.

Bigger devices (50x50μm^2) were the most promising, as a huge increase in the resistance of smaller devices was reported.

The mismatch reported in the electrodes H_C was not totally understood, the presence of a shape related anisotropy was excluded by simulation, a possible reason may be the oxidation of the cobalt layer, that affects it's magnetic properties, [75], while no TMR was reported except some telegraphic noises [74].

Chapter 6

Molecular spin Valve

6.1 Introduction

The race toward finding alternatives to traditional Von-Neumann computing due to the bottleneck problem, many new computing techniques emerged, among these is NC, a technique that emulates brain performance, thus allow in-memory computing. For that, many materials were suggested that have the ability to store information, and compute at the same time in a NV manner, one of the most promising are resistive switching materials.
These materials follow a NV modification of their resistance, as a consequence of the bi-multi stable states that can be controlled by external stimuli.
Molecular spin valves (MSV) are spintronics that may experience a resistance change in response to external magnetic fields (GMR effect), in addition, NV, reversible modification in these devices resistance was also reported [15], when elaborating a thin post transition oxide layer in the device, following the formation/rupture of CF in the MS layer. These two switches can be harnessed to achieve higher storage/computing densities [76, 77].
LSMO/Gaq3/AlOx/Co is an MSV composed of a Tris(8-hydroxyquinoline)-Gallium(III)(Gaq3) and a thin oxide layer(AlO_x), sandwiched between two FM electrodes (LSMO/Co). The LSMO half-metal is used as spin injector, due to it's remarkable electrical and magnetic properties of generating a fully spin-polarized currents (up to 100% theoretically), thus resulting a totally polarized spin injection [78].
The Gaq3 MS usage as a spin transport medium, is due to the considerably large spin mean free path, as a result of the small spin-orbit, reduced hyperfine interactions, and absence of Hanle effect [79], while the metal-oxide layer serves two purposes, to protect the 'soft' MS from an ill-defined layer, that can be caused by top electrode atoms (Co) inter-diffusion upon deposition, and as an oxygen source [15].

The resistance modification in these devices is caused by conductive filament formation inside the MS, controlled by an applied external electric field (positive/negative) applied to the bottom electrode that activate oxygen ions migration forth and back from the oxide layer toward the MS, resulting the formation/rupture of complexes(Gaq3-O_2), thereby affecting the

materials electric, and spin transport properties6.1, which reflects on both devices resistance, and GMR ratio [15,80].

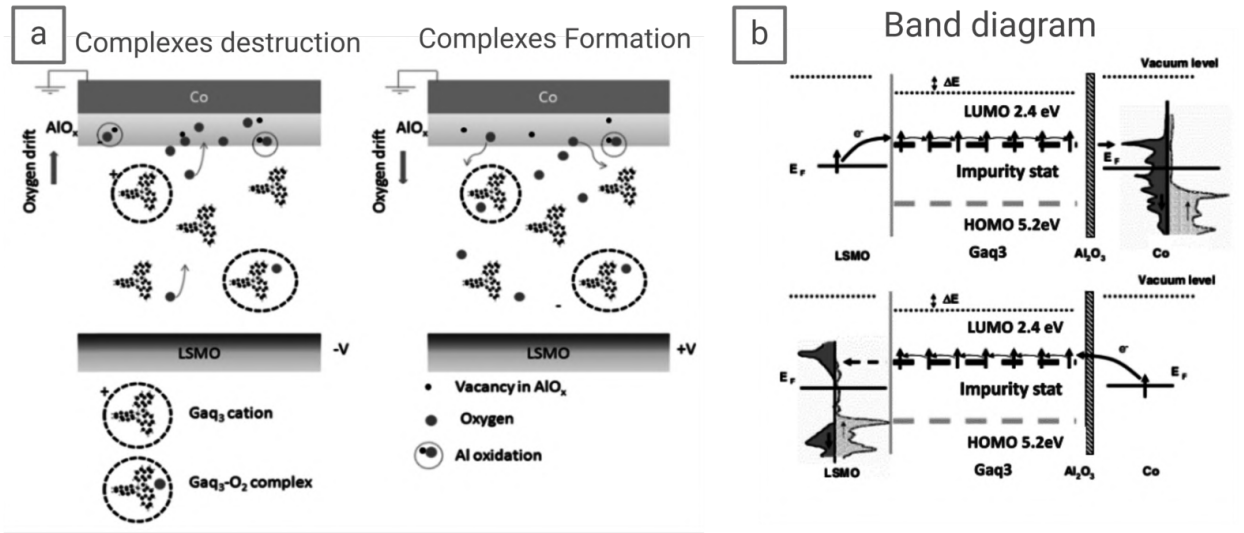

Figure 6.1: Spin transport in an LSMO/Gaq3/AlOx/Co MSV a) illustrative scheme. b) Energy diagram (taken from [15]).

In the following work we investigate electrical, and magneto-electrical properties of 16 LSMO(20 nm)/Gaq3(15 nm)/AlOx(2 nm)/Co(10 nm) MSV, hosted in a 4x4 crossbar circuit.The analysis involves characterization of all devices, by means of IV and MR measurements, at room temperature, and cryogenic temperatures (100 K).

6.2 Experimental details

For the fabrication, an STO substrate containing 4 LSMO 20 nm thick strips, previously deposited by channel spark ablation (CSA) was used [81]. A first, in-situ annealing of the sample was performed under UHV(9×10^{-9} mbar), at 250°C, for 30 minutes, then left to cool down to room temperature (2h) prior deposition. Once the sample's temperature reached about 40 °C, 2 consecutive shadow PVD were performed to deposit 15 nm Gaq3, and 2 nm Al, respectively, then oxidized by exposure to partial pressure of O_2. Finally, a shadow EBPVD was performed to deposit 4, 10 nm thick Co strips, all deposition parameters used are summarized in (tab.6.1). The final substrate hosted 16 devices, assembled in a crossbar geometry (fig.6.2). After fabrication, the substrate was placed in a glass container, and stored in an active storage environment to slow aging.

The substrate surface was imaged using AFM, then horizontally mounted on the sample holder (fig.4.7), and placed in a cryostat(fig.4.6), devices were then connected to the SMUs for characterization through a matrix used to control the connections (fig.6.2). For the resistance estimation, IVs were performed using low reading voltages (-100 mV), applied to bottom

electrodes, while current measuring at top electrodes. For the MR measurements, all devices were characterized in a similar fashion, resistance estimation was done by low reading voltages (-100 mV), while subjecting the substrate to a cyclic magnetic induction sweep between [300;-300] mT, and for the resistance temperature measurements, resistance estimation was performed similarly to the MR, after each 5 K decrease in the temperature.

Deposited layers	vacuum (mbar)	deposition rate (nm/min)	time (min)
Gaq3(PVD)	9×10^{-9}	1	15'
Al(PVD)	10^{-8}	0.6	3'5"
Co(EBPVD)	1.8×10^{-10}	0.2	50'

Table 6.1: Deposition parameters.

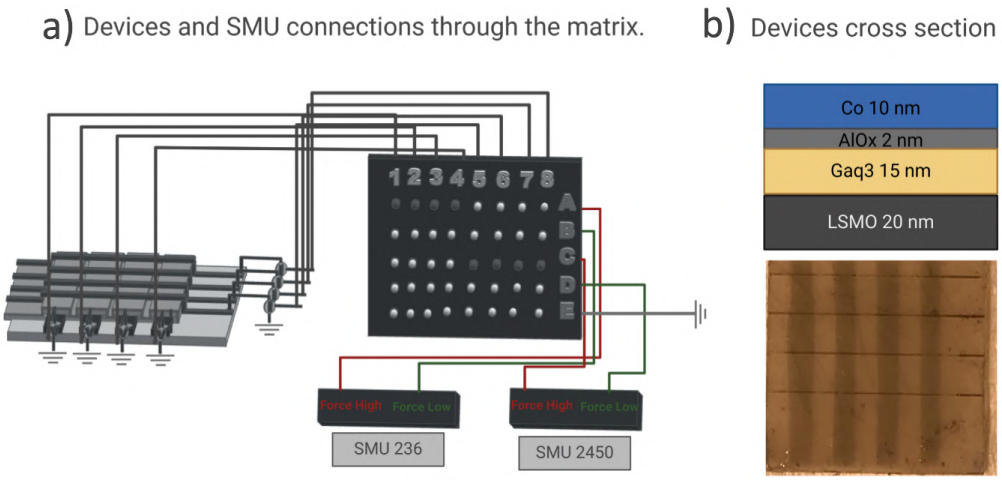

Figure 6.2: a) experimental setup used for the electrical characterization. b) Devices cross section, and real image.

6.3 Results and discussion

1. **Surface analysis**

First, surface morphology was probed by AFM for different deposited layers (fig.6.3). STO layer showed an extremely fine surface, after the deposition of LSMO, small islands were observed (fig.6.4), however, after the MS and oxide layer deposition, the surface roughness increased by few nm (fig.6.7), and after the cobalt deposition, a decrease in peak to trough was observed (fig.6.3) [82].

Grains mean size was estimated by a Gaussian fit of the radial ACF(equ.4.20) for each deposited layer, while RMS roughness was estimated using statistical methods, results are represented in the (tab.6.2).

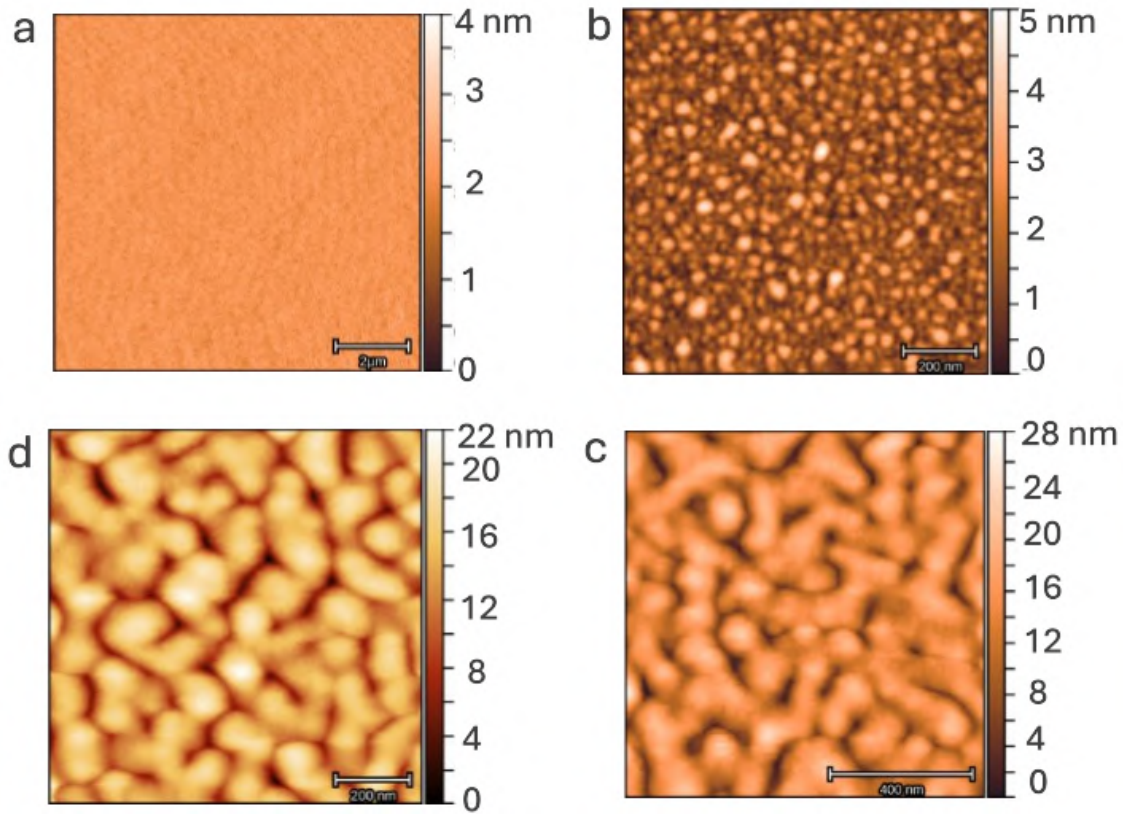

Figure 6.3: AFM image of a) STO, b) STO/LSMO, c) STO/LSMO/GaQ3/AlOx, and d) STO/LSMO/GaQ3/AlOx/Co surfaces.

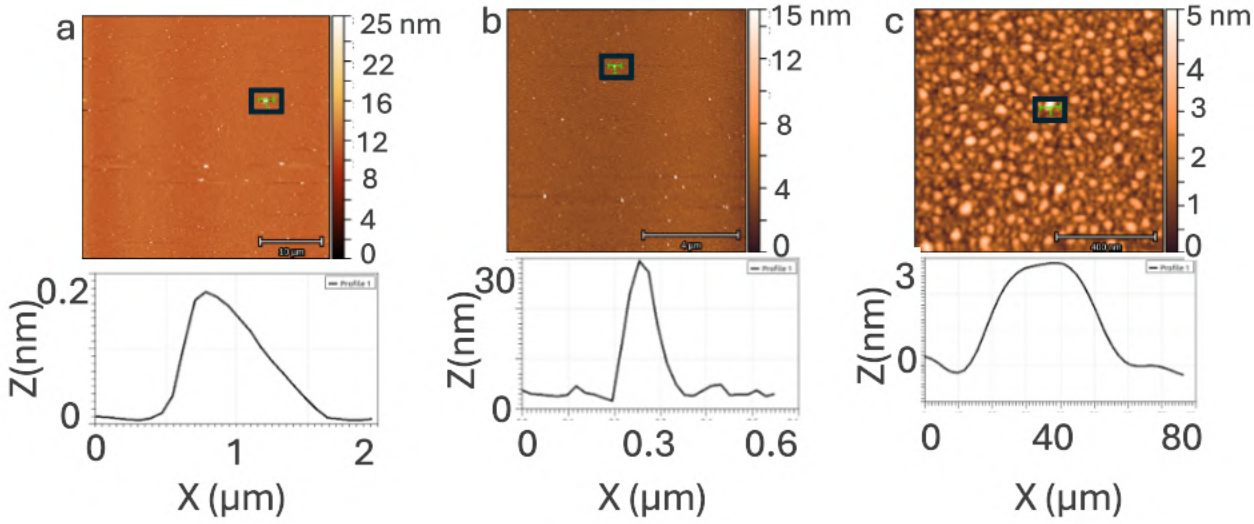

Figure 6.4: AFM images of LSMO deposited on top of STO at different scales.

In analogy with (tab.6.2), and (fig.6.4), LSMO layer contained two types of grains, around a micron rounded grains attributed to the non-uniform generated vapor, and can be caused by micro-cracks, pits or weakly attached molecules present on the target source

surface, and other sub-micron rounded or faceted features [81], that were attributed to the subsurface superheating during deposition [78,83].
After the Gaq3/AlOx deposition, a few nm increase in the surface roughness was observed. Viewed surface features can be grouped into miron sized, round shaped observed at big scales(fig.6.6), and other sub-micron, with rounded, and elongated shapes(fig.6.7). In comparison with the STO/Gaq3/AlOx morphology(fig.6.5), a first remark was the disappearance of the rounded features viewed at the sub-micon range, while elongated features persisted.

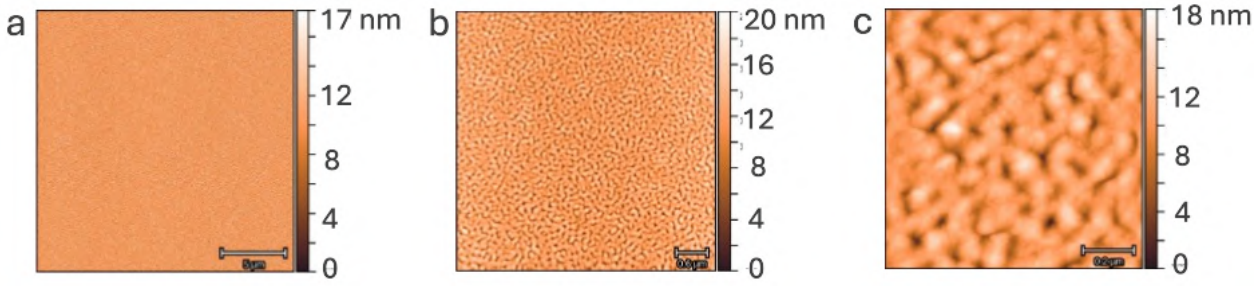

Figure 6.5: AFM image of Gaq3/AlOx deposition on top of STO, at different scales.

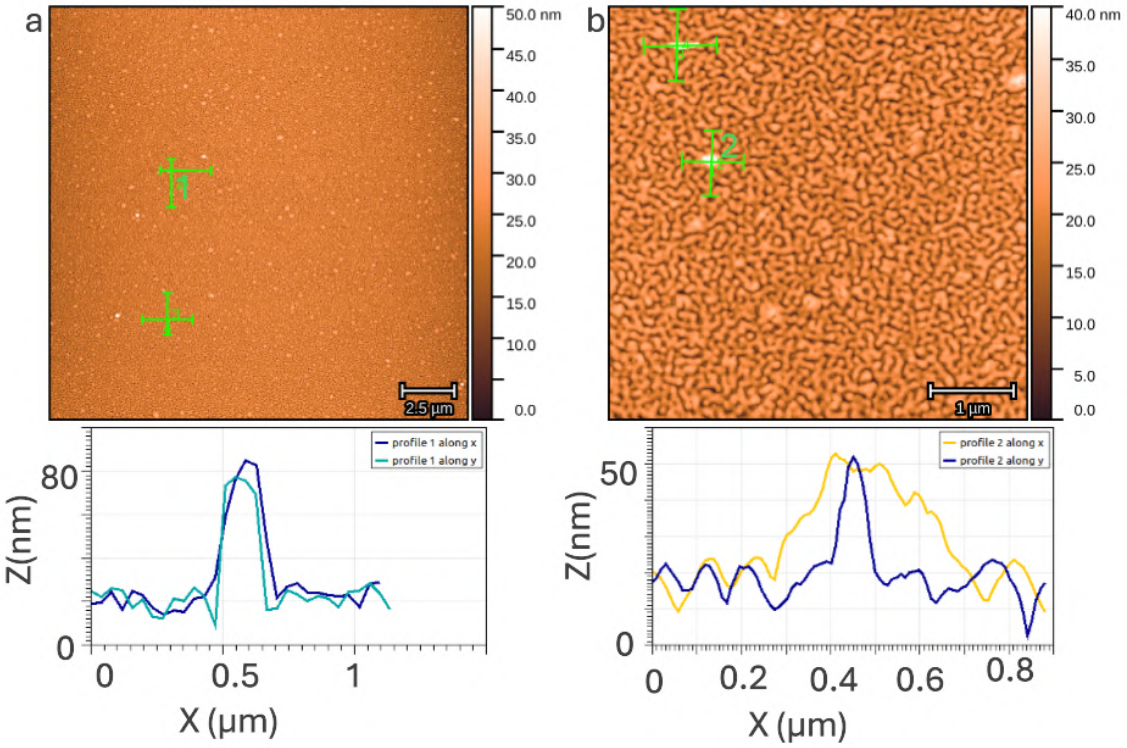

Figure 6.6: Deposition of Gaq3/AlO$_x$, on top of LSMO, and profile of different grains viewed at different scales.

After the Co deposition on top of STO/LSMO/Gaq3/AlO$_x$, the same features were also reported, with a decrease in the surface RMS roughness. A slight increase in the

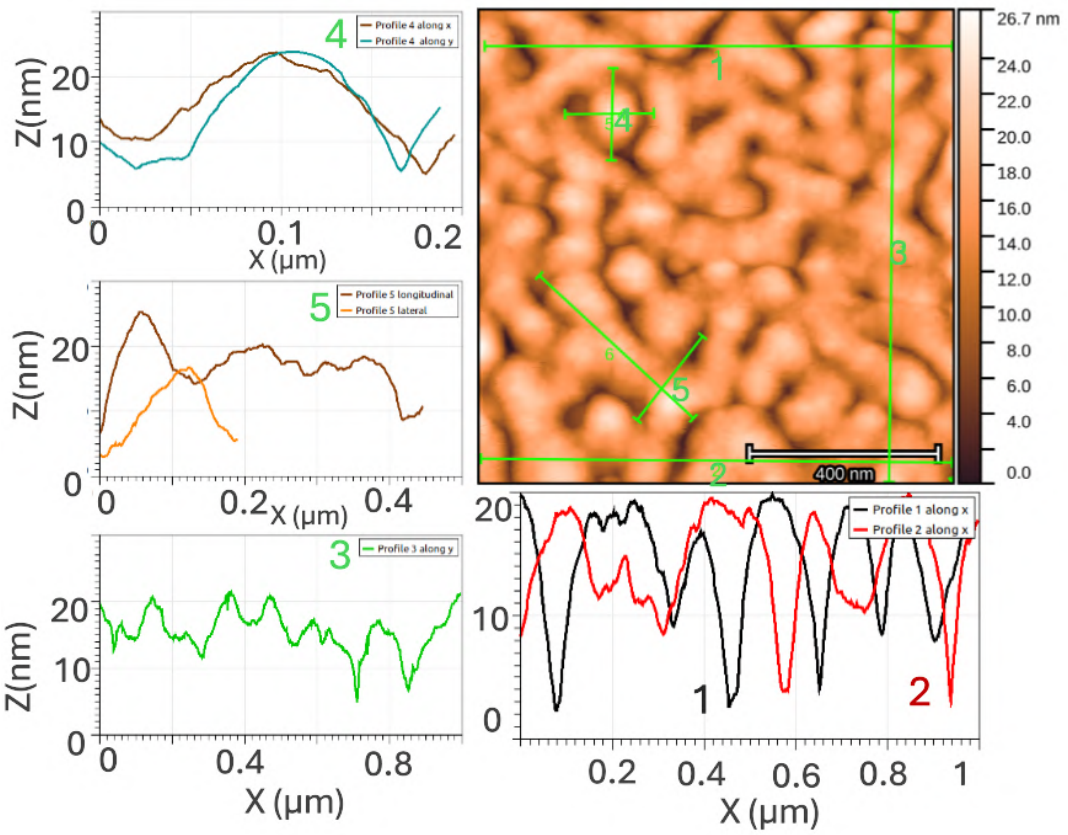

Figure 6.7: LSMO/Gaq3/AlOx 1x1 μm^2 AFM image, profile of surface morphology and different observed grains.

mean grains size, and slight decrease in the mean grains height was reported, indicating a slight increase in the deposition efficiency on features edges and in pits, than on peaks [82]. However, for Co deposition on top of the STO, a very fine surface was reported, reflecting a smooth, uniform deposition(RMS=2.5 Å), and was attributed to the fine substrate surface, deposition conditions(UHV at 10^{-10} mbar), and the used deposition technique(EBPVD).

Deposited layers, on top of STO consecutively all numbers are in (nm)	mean size (nm)	RMS size (nm)	RMS roughness (nm)
LSMO(20)	7.43	0.714	0.71
LSMO(20)/Gaq3(15)/AlOx(2)	16.04	3.96	3.84
LSMO(20)/Gaq3(15)/AlOx(2)/Co(10)	16.20	3.05	2.99
STO/Gaq3(15)/AlOx(2)	13.98	2.01	3.85
STO/Co(10)	7.19	0.23	0.25

Table 6.2: Table summarizing surface characteristics after each deposited layer, extracted from one (1x1 μm^2) image.

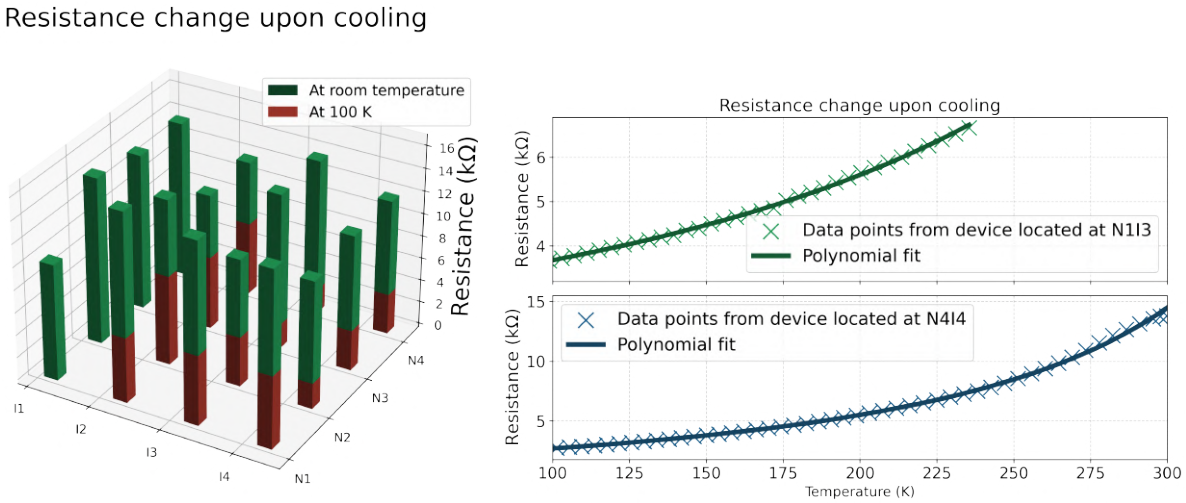

(a) (b)

Figure 6.8: a)Resistance at room temperature and at 100 K, b) resistance-temperature characteristics fitted by a polynomial function.

2. **Electrical characterization**

   At room temperature, all devices showed similar resistances(13 kΩ ± 1.8 kΩ)(fig.6.8.a)). When cooling the substrate, devices showed a sharp resistance drop, due to the dominance of the LSMO on the devices overall resistances (fig.6.8.b)). At 74 K, as the LSMO resistance became negligible, a big variance in the devices resistances was reported (5±1.9 kΩ)(fig.6.8.a)), indicating, similarly to the MTJ, an initial unpredictable intermediate resistance state in these type of materials.

3. **Magnetoresistance characterization**

   At Room temperature, a huge CMR was reported, typical for LSMO half-metal below T_C [81], again, reflecting the dominance of the LSMO to the overall resistance at high temperatures (fig.6.9).
   At 100 K, positive MR effect was reported in all devices, that was later confirmed to be GMR, by comparing MR measurements, while applying the magnetic induction in the devices in-plane longitudinal, and transverse directions, the effect was shown to be independent on the angle, thus ruling out AMR effect, this result confirmed an active spacer between the two electrodes, and in accordance with the random IRS and the correlation between the resistance and magneto-resistance states, the initial GMR ratios were different from D2D (fig.6.9).

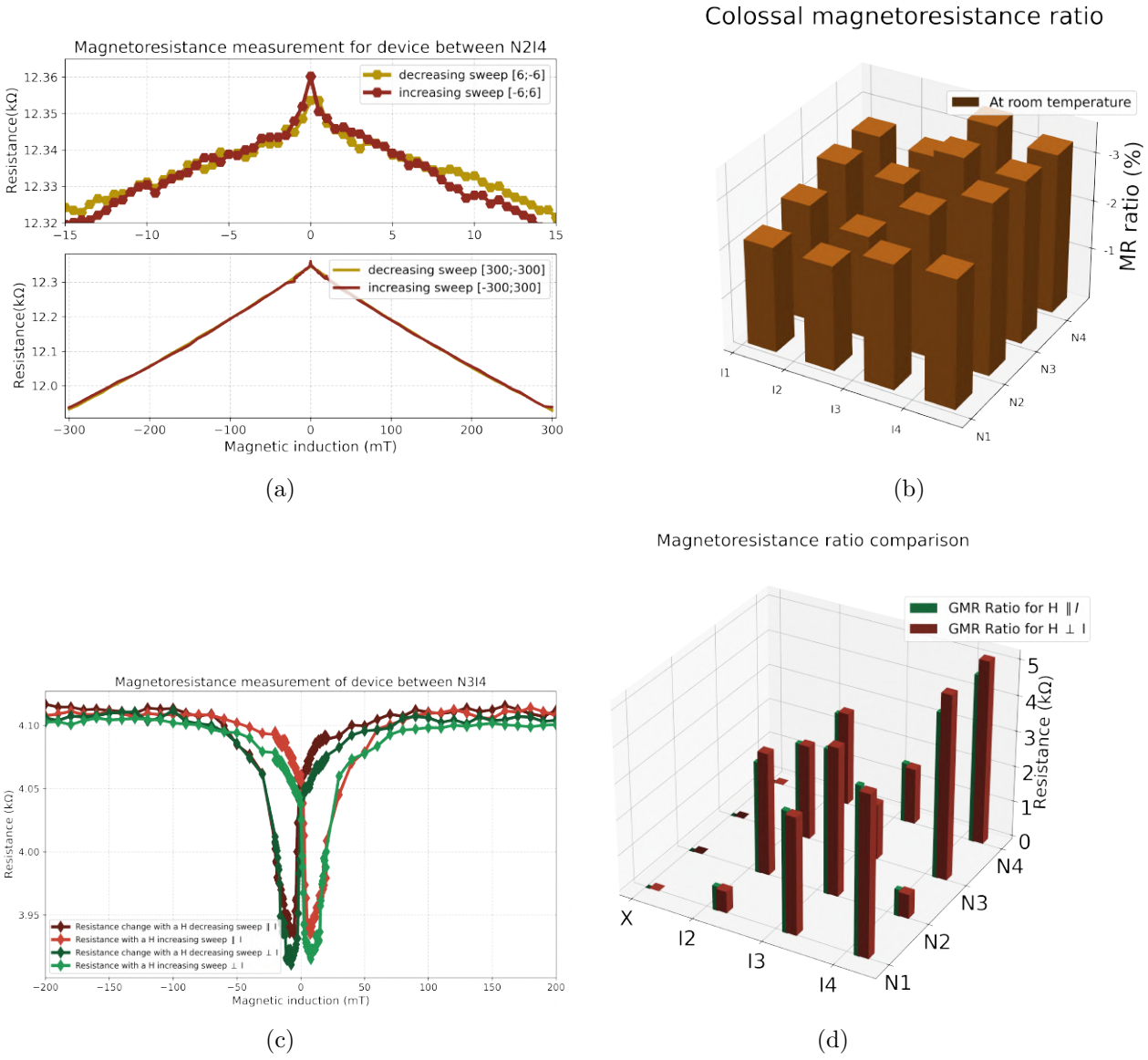

Figure 6.9: a) MR measurement of one of the devices at RT, showing a CMR effect. b) CMR % of all 16 devices. c) MR measurement of one device at 100 K, showing a GMR effect. d) GMR % of 12 devices (equ.2.21).

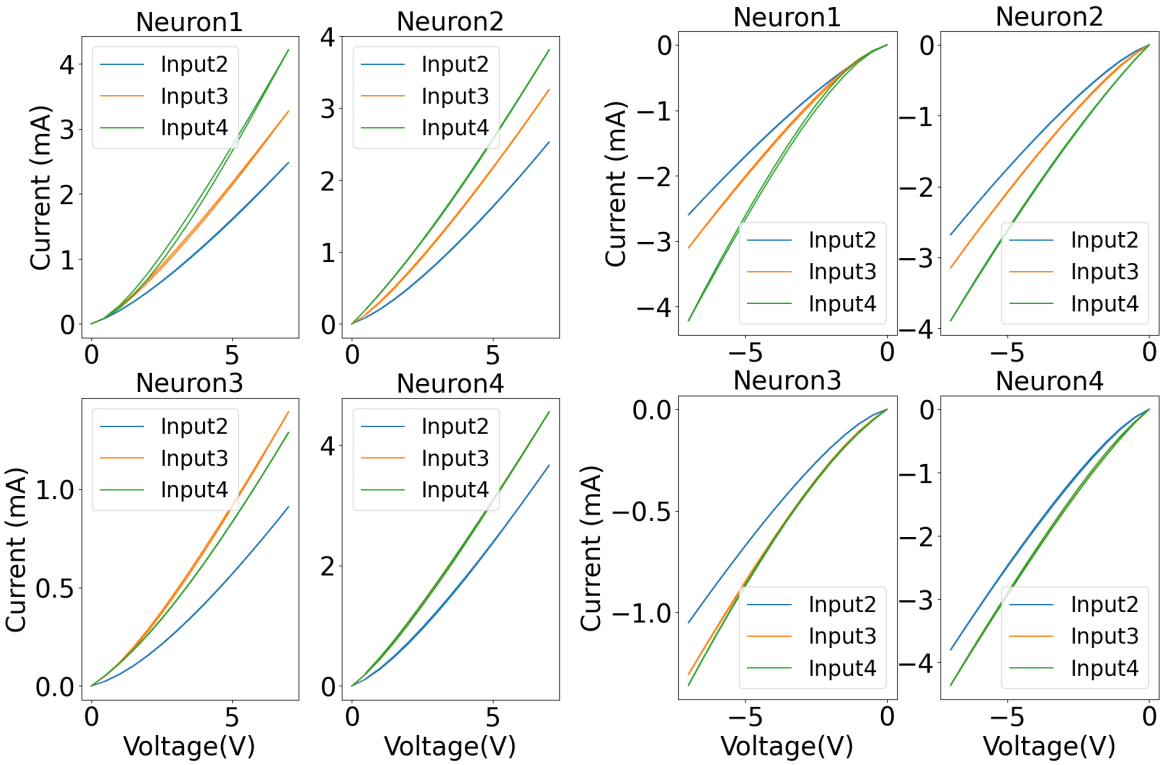

Figure 6.10: 12 devices IV after a) +8 V, and b) -8 V applied sweeps, small hysteresis was reported at N1I4.

4. **Electrical bistability**

At 100 K, devices were subjected to a set of increasing positive voltage sweeps (fig.6.10), in search for any resistance modification. At high applied voltages, devices experienced orders of magnitude increase in their resistance (fig.6.12), then at + 12 V a resistance drop was observed, and was switched back using -12 V. The switch showed a ratio up to 0.6 and was checked for 14 cycles of ± 12 V set-reset pulses(fig.6.11).

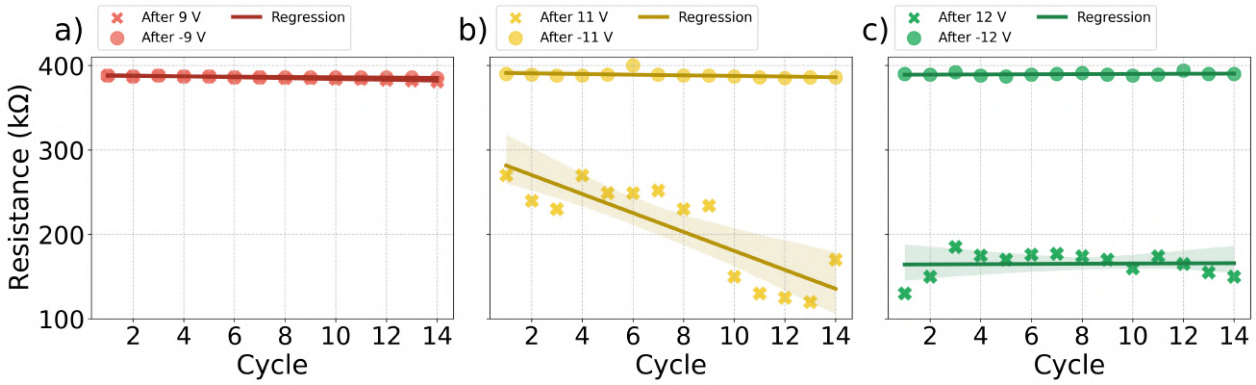

Figure 6.11: Set of (positive-negative) pulses cycles, using a) ± 9 V, b) ±11 V, c) ±12 V. A switch was reported at ±11 V, and was stable at ±12 V.

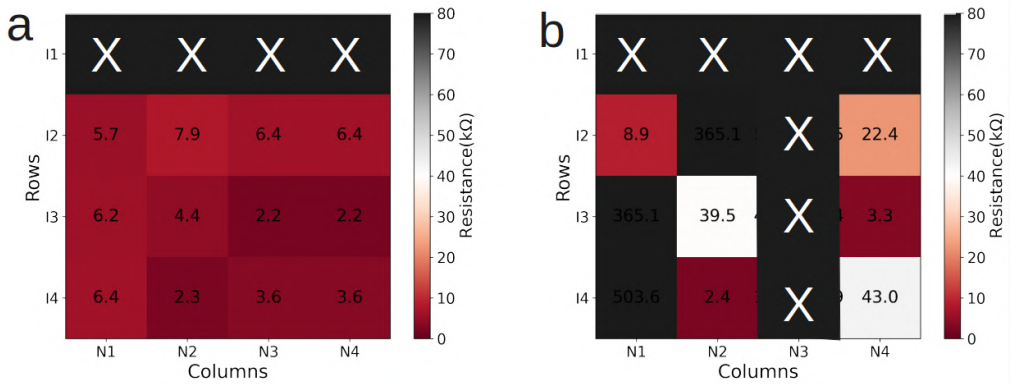

Figure 6.12: a) Devices initial resistances at 100 K. b) Devices resistances after subjection to high applied voltages up to ± 12 V, for 14 cycles. Marked devices are disconnected.

6.4 Conclusions

To conclude, all devices showed magneto resistance switches (GMR effect) at 100 K. The absence of AMR effect indicates an active spacer between the two electrodes, therefore rule out the possibility of having shorts between the electrodes.

Resistive switches were observed in devices at high applied voltages(above 11 V), with an on/off ratio up to 0.6, similar to other spintronics switching devices (SOT-MRAM,STT-MRAM etc.) [84,85].

In addition, both Resistance and magneto-resistance switches were shown to be correlated.

Bibliography

[1] Catherine D Schuman, Shruti R Kulkarni, Maryam Parsa, J Parker Mitchell, Bill Kay, et al. Opportunities for neuromorphic computing algorithms and applications. *Nature Computational Science*, 2(1):10–19, 2022.

[2] Dennis V Christensen, Regina Dittmann, Bernabe Linares-Barranco, Abu Sebastian, Manuel Le Gallo, Andrea Redaelli, Stefan Slesazeck, Thomas Mikolajick, Sabina Spiga, Stephan Menzel, et al. 2022 roadmap on neuromorphic computing and engineering. *Neuromorphic Computing and Engineering*, 2(2):022501, 2022.

[3] John A Hertz. *Introduction to the theory of neural computation*. Crc Press, 2018.

[4] Gianluca Milano, Giacomo Pedretti, Kevin Montano, Saverio Ricci, Shahin Hashemkhani, Luca Boarino, Daniele Ielmini, and Carlo Ricciardi. In materia reservoir computing with a fully memristive architecture based on self-organizing nanowire networks. *Nature materials*, 21(2):195–202, 2022.

[5] Mahyar Shahsavari, Philippe Devienne, and Pierre Boulet. Spiking neural computing in memristive neuromorphic platforms. *Handbook of Memristor Networks*, pages 691–728, 2019.

[6] John MD Coey. *Magnetism and magnetic materials*. Cambridge university press, 2010.

[7] J-H Park, E Vescovo, H-J Kim, C Kwon, R Ramesh, and T Venkatesan. Direct evidence for a half-metallic ferromagnet. *Nature*, 392(6678):794–796, 1998.

[8] Wolfgang Brütting. Physics of organic semiconductors. 2005.

[9] Sergei Baranovski. *Charge transport in disordered solids with applications in electronics*. John Wiley & Sons, 2006.

[10] Nir Tessler, Yevgeni Preezant, Noam Rappaport, and Yohai Roichman. Charge transport in disordered organic materials and its relevance to thin-film devices: a tutorial review. *Advanced Materials*, 21(27):2741–2761, 2009.

[11] Mario Norberto Baibich, Jean Marc Broto, Albert Fert, F Nguyen Van Dau, Frédéric Petroff, P Etienne, G Creuzet, A Friederich, and J Chazelas. Giant magnetoresistance of (001) fe/(001) cr magnetic superlattices. *Physical review letters*, 61(21):2472, 1988.

[12] *https:FVT Fundamentals of Vacuum Technology leybold*.

[13] *https://download.tek.com/manual/2450-900-01E Aug 2019 User.pdf*.

[14] Yizi Xu, D Ephron, and MR Beasley. Directed inelastic hopping of electrons through metal-insulator-metal tunnel junctions. *Physical Review B*, 52(4):2843, 1995.

[15] Ilaria Bergenti, Francesco Borgatti, Marco Calbucci, Alberto Riminucci, Raimondo Cecchini, Patrizio Graziosi, Donald A MacLaren, Angelo Giglia, Jean Pascal Rueff, Denis Céolin, et al. Oxygen impurities link bistability and magnetoresistance in organic spin valves. *ACS applied materials & interfaces*, 10(9):8132–8140, 2018.

[16] Manuel Le Gallo and Abu Sebastian. An overview of phase-change memory device physics. *Journal of Physics D: Applied Physics*, 53(21):213002, 2020.

[17] Dudley Allen Buck et al. Ferroelectrics for digital information storage and switching. Master's thesis, Massachusetts Institute of Technology, Dept. of Electrical Engineering, 1952.

[18] Andrei Shumilin, Prakriti Neha, Mattia Benini, Rajib Rakshit, Manju Singh, Patrizio Graziosi, Raimondo Cecchini, Luca Gnoli, Mirko Prezioso, Ilaria Bergenti, et al. Glassy synaptic time dynamics in molecular la0. 7sr0. 3mno3/gaq3/alox/co spintronic crossbar devices. *Advanced Electronic Materials*, page 2300887, 2024.

[19] Alberto Riminucci and Robert Legenstein. Fast learning synapses with molecular spin valves via selective magnetic potentiation. *arXiv preprint arXiv:1903.08624*, 2019.

[20] Kyun-Ho Jung, Seung-Gon Song, Kyoung-Wan Park, Jung-Hyun Sok, Kyong-Min Kim, and Yun-Sun Park. Observation of alo x material in electrical resistive switching for nonvolatile random access memory application. *Journal of the Korean Physical Society*, 70:489–493, 2017.

[21] Bhagwat Swaroop, WC West, Gregory Martinez, MN Kozicki, and LA Akers. Programmable current mode hebbian learning neural network using programmable metallization cell. In *1998 IEEE International Symposium on Circuits and Systems (ISCAS)*, volume 3, pages 33–36. IEEE, 1998.

[22] Gianluca Milano, Samuele Porro, Ilia Valov, and Carlo Ricciardi. Recent developments and perspectives for memristive devices based on metal oxide nanowires. *Advanced Electronic Materials*, 5(9):1800909, 2019.

[23] Shuang Pi, Can Li, Hao Jiang, Weiwei Xia, Huolin Xin, J Joshua Yang, and Qiangfei Xia. Memristor crossbar arrays with 6-nm half-pitch and 2-nm critical dimension. *Nature nanotechnology*, 14(1):35–39, 2019.

[24] Qi Liu, Bin Gao, Peng Yao, Dong Wu, Junren Chen, Yachuan Pang, Wenqiang Zhang, Yan Liao, Cheng-Xin Xue, Wei-Hao Chen, et al. 33.2 a fully integrated analog reram based 78.4 tops/w compute-in-memory chip with fully parallel mac computing. In *2020 IEEE International Solid-State Circuits Conference-(ISSCC)*, pages 500–502. IEEE, 2020.

[25] Mirko Prezioso, Farnood Merrikh-Bayat, Brian D Hoskins, Gina C Adam, Konstantin K Likharev, and Dmitri B Strukov. Training and operation of an integrated neuromorphic network based on metal-oxide memristors. *Nature*, 521(7550):61–64, 2015.

[26] Can Li, Daniel Belkin, Yunning Li, Peng Yan, Miao Hu, Ning Ge, Hao Jiang, Eric

Montgomery, Peng Lin, Zhongrui Wang, et al. Efficient and self-adaptive in-situ learning in multilayer memristor neural networks. *Nature communications*, 9(1):2385, 2018.

[27] Peng Yao, Huaqiang Wu, Bin Gao, Jianshi Tang, Qingtian Zhang, Wenqiang Zhang, J Joshua Yang, and He Qian. Fully hardware-implemented memristor convolutional neural network. *Nature*, 577(7792):641–646, 2020.

[28] Giacomo Pedretti and Daniele Ielmini. In-memory computing with resistive memory circuits: Status and outlook. *Electronics*, 10(9):1063, 2021.

[29] Nitin Rathi, Indranil Chakraborty, Adarsh Kosta, Abhronil Sengupta, Aayush Ankit, Priyadarshini Panda, and Kaushik Roy. Exploring neuromorphic computing based on spiking neural networks: Algorithms to hardware. *ACM Computing Surveys*, 55(12):1–49, 2023.

[30] Tadashi Kadowaki and Hidetoshi Nishimori. Quantum annealing in the transverse ising model. *Physical Review E*, 58(5):5355, 1998.

[31] Mark W Johnson, Mohammad HS Amin, Suzanne Gildert, Trevor Lanting, Firas Hamze, Neil Dickson, Richard Harris, Andrew J Berkley, Jan Johansson, Paul Bunyk, et al. Quantum annealing with manufactured spins. *Nature*, 473(7346):194–198, 2011.

[32] Maliheh Aramon, Gili Rosenberg, Elisabetta Valiante, Toshiyuki Miyazawa, Hirotaka Tamura, and Helmut G Katzgraber. Physics-inspired optimization for quadratic unconstrained problems using a digital annealer. *Frontiers in Physics*, 7:48, 2019.

[33] Dagur I Albertsson and Ana Rusu. Highly reconfigurable oscillator-based ising machine through quasiperiodic modulation of coupling strength. *Scientific Reports*, 13(1):4005, 2023.

[34] David B Fogel. *Evolutionary computation: toward a new philosophy of machine intelligence*. John Wiley & Sons, 2006.

[35] William A Borders, Ahmed Z Pervaiz, Shunsuke Fukami, Kerem Y Camsari, Hideo Ohno, and Supriyo Datta. Integer factorization using stochastic magnetic tunnel junctions. *Nature*, 573(7774):390–393, 2019.

[36] Kerem Y Camsari, Brian M Sutton, and Supriyo Datta. P-bits for probabilistic spin logic. *Applied Physics Reviews*, 6(1), 2019.

[37] David H Ackley, Geoffrey E Hinton, and Terrence J Sejnowski. A learning algorithm for boltzmann machines. *Cognitive science*, 9(1):147–169, 1985.

[38] Andrew Lucas. Ising formulations of many np problems. *Frontiers in physics*, 2:5, 2014.

[39] F Barahona. On the computational complexity of ising spin glass models. *Journal of Physics A: Mathematical and General*, 15(10):3241, oct 1982.

[40] Takahiro Inagaki, Yoshitaka Haribara, Koji Igarashi, Tomohiro Sonobe, Shuhei Tamate, Toshimori Honjo, Alireza Marandi, Peter L McMahon, Takeshi Umeki, Koji Enbutsu, et al. A coherent ising machine for 2000-node optimization problems. *Science*, 354(6312):603–606, 2016.

[41] Peter L McMahon, Alireza Marandi, Yoshitaka Haribara, Ryan Hamerly, Carsten Langrock, Shuhei Tamate, Takahiro Inagaki, Hiroki Takesue, Shoko Utsunomiya, Kazuyuki Aihara, et al. A fully programmable 100-spin coherent ising machine with all-to-all connections. *Science*, 354(6312):614–617, 2016.

[42] Guillermo Gallego, Tobi Delbrück, Garrick Orchard, Chiara Bartolozzi, Brian Taba, Andrea Censi, Stefan Leutenegger, Andrew J. Davison, Jörg Conradt, Kostas Daniilidis, and Davide Scaramuzza. Event-based vision: A survey. *IEEE Transactions on Pattern Analysis and Machine Intelligence*, 44(1):154–180, 2022.

[43] Marco Monforte, Ander Arriandiaga, Arren Glover, and Chiara Bartolozzi. Where and when: event-based spatiotemporal trajectory prediction from the icub's point-of-view. In *2020 IEEE International Conference on Robotics and Automation (ICRA)*, pages 9521–9527. IEEE, 2020.

[44] Sung Woon Cho, Chanho Jo, Yong-Hoon Kim, and Sung Kyu Park. Progress of materials and devices for neuromorphic vision sensors. *Nano-Micro Letters*, 14(1):203, 2022.

[45] Daniel Gutierrez-Galan, Juan P. Dominguez-Morales, Fernando Perez-Peña, Angel Jimenez-Fernandez, and Alejandro Linares-Barranco. Neuropod: A real-time neuromorphic spiking cpg applied to robotics. *Neurocomputing*, 381:10–19, 2020.

[46] JW Gardner, EL Hines, and M Wilkinson. Application of artificial neural networks to an electronic olfactory system. *Measurement Science and Technology*, 1(5):446, 1990.

[47] Evor L. Hines and Julian W. Gardner. An artificial neural emulator for an odour sensor array. *Sensors and Actuators B: Chemical*, 19(1):661–664, 1994.

[48] Minhao Yang, Chen-Han Chien, Tobi Delbruck, and Shih-Chii Liu. A 0.5 v 55 μW 64 $\times$ 2 channel binaural silicon cochlea for event-driven stereo-audio sensing. *IEEE Journal of Solid-State Circuits*, 51(11):2554–2569, 2016.

[49] Ismail Uysal, Harsha Sathyendra, and John Harris. Towards spike-based speech processing: a biologically plausible approach to simple acoustic classification. *International Journal of Applied Mathematics and Computer Science*, 18(2):129–137, 2008.

[50] Stefano Buccelli, Yannick Bornat, Ilaria Colombi, Matthieu Ambroise, Laura Martines, Valentina Pasquale, Marta Bisio, Jacopo Tessadori, Przemysław Nowak, Filippo Grassia, et al. A neuromorphic prosthesis to restore communication in neuronal networks. *IScience*, 19:402–414, 2019.

[51] Gabriella Panuccio, Marianna Semprini, and Michela Chiappalone. Intelligent biohybrid systems for functional brain repair. *New Horizons in Translational Medicine*, 3(3):162–174, 2016.

[52] David J Guggenmos, Meysam Azin, Scott Barbay, Jonathan D Mahnken, Caleb Dunham, Pedram Mohseni, and Randolph J Nudo. Restoration of function after brain damage using a neural prosthesis. *Proceedings of the National Academy of Sciences*, 110(52):21177–21182, 2013.

[53] V Dediu, LE Hueso, I Bergenti, A Riminucci, F Borgatti, P Graziosi, C Newby, F Casoli,

Machiel Pieter De Jong, C Taliani, et al. effects in alq 3-based hybrid devices. *Physical Review B*, 78(11):115203, 2008.

[54] Radek Pohl, Victor A Montes, Joseph Shinar, and Pavel Anzenbacher. Red- green- blue emission from tris (5-aryl-8-quinolinolate) al (iii) complexes. *The Journal of organic chemistry*, 69(5):1723–1725, 2004.

[55] John G Simmons. Electric tunnel effect between dissimilar electrodes separated by a thin insulating film. *Journal of applied physics*, 34(9):2581–2590, 1963.

[56] Stefan Landis. *Lithography*. John Wiley & Sons, 2013.

[57] Yokogawa Corporation of America Barry Bolling, Senior Application Engineer. *Understanding Source Measure Unit Specifications*.

[58] *https://www.testequipmenthq.com/datasheets/KEITHLEY-236-Datasheet.pdf*.

[59] *https://download.tek.com/manual/SPEC-2450B November 2017.pdf*.

[60] Weilie Zhou, Robert Apkarian, Zhong Lin Wang, and David Joy. Fundamentals of scanning electron microscopy (sem). *Scanning Microscopy for Nanotechnology: Techniques and Applications*, pages 1–40, 2007.

[61] Jun Zhang, Pengcheng Chen, Bingkai Yuan, Wei Ji, Zhihai Cheng, and Xiaohui Qiu. Real-space identification of intermolecular bonding with atomic force microscopy. *Science*, 342(6158):611–614, 2013.

[62] G Rasigni, M Rasigni, J Palmari, C Dussert, F Varnier, and A Llebaria. Statistical parameters for random and pseudorandom rough surfaces. *JOSA A*, 5(1):99–103, 1988.

[63] Larry Senesac and Thomas G Thundat. Nanosensors for trace explosive detection. *Materials today*, 11(3):28–36, 2008.

[64] Lilan Zou, Wei Hu, Wei Xie, Ruqi Chen, Ni Qin, Baojun Li, and Dinghua Bao. Excellent resistive switching property and physical mechanism of amorphous tio2 thin films fabricated by a low-temperature photochemical solution deposition method. *Applied surface science*, 311:697–702, 2014.

[65] Hasan Efeoglu, Süheyla Güllülü, and Tevhit Karacali. Resistive switching of reactive sputtered tio2 based memristor in crossbar geometry. *Applied Surface Science*, 350:10–13, 2015.

[66] Zongwei Wang, Jian Kang, Zhizhen Yu, Yichen Fang, Yaotian Ling, Yimao Cai, Ru Huang, and Yangyuan Wang. Modulation of nonlinear resistive switching behavior of a taox-based resistive device through interface engineering. *Nanotechnology*, 28(5):055204, 2016.

[67] Giin-Shan Chen, An-Chi Cho, and Sung-Te Chen. Anodization of tantalum films for the enhancement of monolayer seeding and electroless copper plating. *Journal of The Electrochemical Society*, 167(8):082506, 2020.

[68] Yanfei Qi, Ce Zhou Zhao, Chenguang Liu, Yuxiao Fang, Jiahuan He, Tian Luo, Li Yang, and Chun Zhao. Comparisons of switching characteristics between ti/al2o3/pt and

tin/al2o3/pt rram devices with various compliance currents. *Semiconductor Science and Technology*, 33(4):045003, 2018.

[69] Cheng-Lin Tsai, Feng Xiong, Eric Pop, and Moonsub Shim. Resistive random access memory enabled by carbon nanotube crossbar electrodes. *Acs Nano*, 7(6):5360–5366, 2013.

[70] Ziyi Wang, Bo Sun, Haibo Ye, Zhiyong Liu, Guanglan Liao, and Tielin Shi. Annealed alox film with enhanced performance for bipolar resistive switching memory. *Applied Surface Science*, 546:149094, 2021.

[71] PP Freitas, R Ferreira, S Cardoso, and F Cardoso. Magnetoresistive sensors. *Journal of Physics: condensed matter*, 19(16):165221, 2007.

[72] Jhen-Yong Hong, Chen-Feng Hung, Kui-Hon Ou Yang, Kuan-Chia Chiu, Dah-Chin Ling, Wen-Chung Chiang, and Minn-Tsong Lin. Electrically programmable magnetoresistance in alo x-based magnetic tunnel junctions. *hong*, 11(1):6027, 2021.

[73] JM Teixeira, J Ventura, R Fermento, JP Araujo, JB Sousa, P Wisniowski, and PP Freitas. Electroforming, magnetic and resistive switching in mgo-based tunnel junctions. *Journal of Physics D: Applied Physics*, 42(10):105407, 2009.

[74] Stefano Brivio, Jacopo Frascaroli, Erika Covi, and Sabina Spiga. Stimulated ionic telegraph noise in filamentary memristive devices. *Scientific reports*, 9(1):6310, 2019.

[75] M El-Tahawy, L Péter, LF Kiss, J Gubicza, Zs Czigány, Gy Molnár, and I Bakonyi. Anisotropic magnetoresistance (amr) of cobalt: hcp-co vs. fcc-co. *Journal of Magnetism and Magnetic Materials*, 560:169660, 2022.

[76] Mirko Prezioso, Alberto Riminucci, Patrizio Graziosi, Ilaria Bergenti, Rajib Rakshit, Raimondo Cecchini, Anna Vianelli, Francesco Borgatti, Norman Haag, M Willis, et al. A single-device universal logic gate based on a magnetically enhanced memristor. *Advanced Materials*, 25(4):534–538, 2013.

[77] Vinod K Sangwan, Deep Jariwala, In Soo Kim, Kan-Sheng Chen, Tobin J Marks, Lincoln J Lauhon, and Mark C Hersam. Gate-tunable memristive phenomena mediated by grain boundaries in single-layer mos2. *Nature nanotechnology*, 10(5):403–406, 2015.

[78] Fenghong Li, Yiqiang Zhan, Tsung-Hsun Lee, Xianjie Liu, Akira Chikamatsu, Tzung-Fang Guo, Hong-Ji Lin, JCA Huang, and Mats Fahlman. Modified surface electronic and magnetic properties of la0. 6sr0. 4mno3 thin films for spintronics applications. *The Journal of Physical Chemistry C*, 115(34):16947–16953, 2011.

[79] Alberto Riminucci, Mirko Prezioso, Chiara Pernechele, Patrizio Graziosi, Ilaria Bergenti, Raimondo Cecchini, Marco Calbucci, Massimo Solzi, and V Alek Dediu. Hanle effect missing in a prototypical organic spintronic device. *Applied Physics Letters*, 102(9), 2013.

[80] Alberto Riminucci, Zhi-Gang Yu, Mirko Prezioso, Raimondo Cecchini, Ilaria Bergenti, Patrizio Graziosi, and Valentin Alek Dediu. Controlling magnetoresistance by oxygen impurities in mq3-based molecular spin valves. *ACS applied materials & interfaces*, 11(8):8319–8326, 2019.

[81] Patrizio Graziosi, Mirko Prezioso, Alessandro Gambardella, Catherine Kitts, Rajib Kumar Rakshit, Alberto Riminucci, Ilaria Bergenti, Francesco Borgatti, Chiara Pernechele, Massimo Solzi, et al. Conditions for the growth of smooth la0. 7sr0. 3mno3 thin films by pulsed electron ablation. *Thin Solid Films*, 534:83–89, 2013.

[82] Ilaria Bergenti, Alberto Riminucci, E Arisi, Mauro Murgia, Massimiliano Cavallini, Massimo Solzi, Francesca Casoli, and V Dediu. Magnetic properties of cobalt thin films deposited on soft organic layers. *Journal of Magnetism and Magnetic Materials*, 316(2):e987–e989, 2007.

[83] Rajiv K Singh, D Bhattacharya, and Jl Narayan. Subsurface heating effects during pulsed laser evaporation of materials. *Applied physics letters*, 57(19):2022–2024, 1990.

[84] Yitao Ma, Sadahiko Miura, Hiroaki Honjo, Shoji Ikeda, Takahiro Hanyu, Hideo Ohno, and Tetsuo Endoh. A 600-µw ultra-low-power associative processor for image pattern recognition employing magnetic tunnel junction-based nonvolatile memories with autonomic intelligent power-gating scheme. *Japanese Journal of Applied Physics*, 55(4S):04EF15, mar 2016.

[85] Valerio Milo, Gerardo Malavena, Christian Monzio Compagnoni, and Daniele Ielmini. Memristive and cmos devices for neuromorphic computing. *Materials*, 13(1):166, 2020.